

Electronic Thesis and Dissertation Repository

---

8-3-2017 10:30 AM

# The Design, Fabrication, and Characterization of Nanoparticle-Protein Interactions for Theranostic Applications

Wai Hei Tse  
*The University of Western Ontario*

Supervisor  
Dr. Jin Zhang  
*The University of Western Ontario*

Graduate Program in Medical Biophysics  
A thesis submitted in partial fulfillment of the requirements for the degree in Doctor of  
Philosophy  
© Wai Hei Tse 2017

Follow this and additional works at: <https://ir.lib.uwo.ca/etd>



Part of the [Biomedical Engineering and Bioengineering Commons](#), [Medical Biophysics Commons](#), and  
the [Nanotechnology Commons](#)

---

## Recommended Citation

Tse, Wai Hei, "The Design, Fabrication, and Characterization of Nanoparticle-Protein Interactions for Theranostic Applications" (2017). *Electronic Thesis and Dissertation Repository*. 4781.  
<https://ir.lib.uwo.ca/etd/4781>

This Dissertation/Thesis is brought to you for free and open access by Scholarship@Western. It has been accepted for inclusion in Electronic Thesis and Dissertation Repository by an authorized administrator of Scholarship@Western. For more information, please contact [wlsadmin@uwo.ca](mailto:wlsadmin@uwo.ca).

## **Abstract**

Theranostics, a combination of therapeutics and diagnostics, spans a spectrum of research areas to provide new opportunities in developing new healthcare technologies and medicine at affordable prices. Through employing a personalized medicine approach, biotechnology can be tailored to the needs of an individual. Applications of theranostics include drug delivery carriers capable of sustained drug release and targeted delivery, biosensors with high sensitivity and selectivity, and diagnostic relevant entities that can be incorporated into the former technologies. Nanotechnology provides a suitable foundation for theranostics to build upon due to material-based properties; magnetism, biocompatibility, and quantum effects to name a few. Purpose can be incorporated and personalized by choosing the correct targeting ligands such as proteins and antibodies which provide both selectivity and specific function. An understanding of the interaction at the atomic level between nanoparticles and proteins can provide insight into ideal modification strategies to maximize the potential of both nanoparticles and the antibody of choice for biomedical applications. Analysis of the cellular protein interaction with theranostic nanotechnology provides a deeper understanding of the parameters and modification strategies to ensure the correct function is achieved. In the area of drug delivery, we investigated the functionalization strategies for the hybridization of organic nanoparticle drug carriers with inorganic imaging compatible nanoparticles, effect of size, and antibody bioconjugation on cell viability. The goal was to ensure the nanoparticle model minimized disruptions to the cellular structures while exacting its purpose for targeted localization or inducing a pharmacological effect. For biosensor applications, we demonstrated a non-invasive alternative to glucose measurement via tear glucose with high selectivity and sensitivity through the conjugation of the lectin concanavalin A (Con A) with fluorescent nanoparticles. Through the Forster Resonance Energy Transfer mechanism, we were able to measure glucose levels as low as 0.03 mM with high selectivity and sensitivity to minute changes in glucose concentration. These findings provide a better understanding of merging antibodies/proteins with nanotechnology and their effect in a biomedical setting. Effective management of

nanotechnology can potentiate a stronger physiological reaction, provide biomedical imaging relevance, and enhance biosensor development.

## **Keywords**

Theranostics, nanoparticles, drug delivery, biosensor, upconversion fluorescence

## Co-Authorship Statement

The following thesis contains four manuscripts: three have been published in peer-reviewed journals and one manuscript has been prepared for submission. As the first author of these peer-reviewed publications, Wai Hei Tse was a significant contributor to all facets of the studies, manuscript preparation, and submission. Wai Hei has contributed to all study designs and was responsible for the design and synthesis of the theranostic models. Specific tasks include optimization of the theranostic model and design of the cellular model to study the interaction between nanoparticles and various cell lines. Following data acquisition, Wai Hei performed data analysis, biomedical interpretation of the data, drafting and final approval of manuscripts. As the Principle Investigator and Supervisor, Dr. Jin Zhang provided continuous guidance and aided in the study conception and nanoparticle design, data acquisition, study planning, and interpretation of data. In addition, Dr. Zhang was responsible and for drafting, performing final revisions, and approval of manuscripts as well as guarantor of data integrity. For each manuscript in this thesis, all other co-authors approved the final draft of the manuscript and their specific contributions are listed below.

Chapter 2 is an original research article entitled "Engineering large gelatin nanospheres coated with quantum dots for targeted delivery to human osteosarcoma cells with enhanced cellular internalization." This manuscript was published in the *Proceedings of the 14th IEEE International Conference on Nanotechnology* in August 2014. This manuscript was co-authored by Wai Hei Tse, Laszlo Gyenis, David W. Litchfield, and Jin Zhang. Laszlo Gyenis assisted with data acquisition of data. David W. Litchfield provided the cells and facilities for live cell imaging.

Chapter 3 is an original research article entitled "Cellular interaction influenced by surface modification strategies of gelatin-based nanoparticles," was published in the *Journal of Biomaterials Applications* in 2017. This manuscript was co-authored by Wai Hei Tse, Laszlo Gyenis, David W. Litchfield, and Jin Zhang. Laszlo Gyenis assisted with data acquisition of data. David W. Litchfield provided the cells and facilities for live cell imaging.

Chapter 4 is a compilation of two original research articles entitled "Bimodal imaging compatible theranostic nanoparticle for anti-angiogenic treatment," and "Biocompatible imaging with NaGdF<sub>4</sub>: Er<sup>3+</sup>, Yb<sup>3+</sup> Upconversion Nanoparticles on HUVEC Cells" are in preparation to be submitted in Sept. 2017. These manuscripts are co-authored by Wai Hei Tse, Songlin Yang, Longyi Chen, Colin M. McCurdy, Christine Tarapacki, Blaine Chronik, and Jin Zhang. Songlin Yang aided in the data acquisition and analysis of pertinent cellular data. Longyi Chen lent his expertise in the physical characterization of the upconversion nanoparticles. Colin M. McCurdy and Christine Tarapacki provided the MRI assessment of the upconversion nanoparticles and its interpretation.

Chapter 5 is an original research article entitled "Nanostructured biosensor for detecting glucose in tear by applying fluorescence resonance energy transfer quenching mechanism," was published in *Biosensors and Bioelectronics* in 2017. This manuscript was co-first authored by Longyi Chen and Wai Hei Tse, Yi Chen, Matthew W. McDonald, James Melling, and Jin Zhang. Yi Chen provided assistance in the substrate synthesis for the nanosized biosensor. Matthew W. McDonald and James Melling provided rat tear samples for our analysis.

## **Acknowledgments**

I would like to thank my supervisor, Dr. Jin Zhang for providing me with the many opportunities within our research group and abroad. Your continuous guidance and support throughout my endeavors have shaped me into the scientist I am today. Again and again, you have provided ample chances to push me beyond my boundaries, resulting in countless opportunities and accomplishments that I was hesitant to reach for. Your wholehearted dedication to your research, students, and vision for discovery will forever encourage me to be engaged in work I love; for this I am grateful. Furthermore, I am thankful for your professional mentorship and faith in my ability.

I am thankful to have Drs. James Lacefield, Shuo Li, and David Litchfield as members of my advisory committee. Thank you for being engaged in my research and pointing me in the right directions. Your guidance, criticism, and words of encouragement have been essential to my development as a researcher and to keep me grounded in my enterprises to reach this point.

The past and present trainees of the Zhang research group have been an invaluable platform to build friendships, foster professional relationships, source of knowledge, and develop research excellence. To Longyan Chen, Yi Chen, and Robert Bi: Thank you for imparting your knowledge to me. The skillset and foundation you provided me will be invaluable moving forward. To Longyi Chen: Thank you for being both a great friend and colleague. Your expertise in materials characterization and nanoparticles has been invaluable in my research and in our collaborations. Your dedication to research excellence has encouraged me to strive for the same. You were always there for me through the good and the bad times, helping me make sense of my data and lending an ear to vent my frustrations. To Songlin Yang: I cannot thank you enough for staying late helping me with data collection. Your perseverance and support during the last stretches of our project was vital to its completion.

To my kendo family and mentors who I have had the pleasure to teach and learn from, you have provided me many opportunities to hone my character, work ethics, and

effective communication skills. Without your patience, understanding, and constant support, I would not be able to achieve a work-life balance and attain the academic and extracurricular achievements I have today.

Most importantly, I would like to thank Clara, my family, and my friends. Your patience, support, and encouragement have contributed significantly to my success. Clara: Thank you for contributing to my success. You have been a critical part of my journey providing both mental and physical support, creative design of media, and never-ending encouragement to seize every opportunity that comes my way. To my parents Bell and Jude, thank you for your support from day one when I decided to pursue my graduate studies. I truly appreciate your long drives to bring me home cooking and providing me the opportunity to focus on my goals.

Finally, I would like to express my deepest gratitude to the various sources of funding that I received throughout my graduate studies. I acknowledge funding support from the National Sciences and Engineering Research Council of Canada, Schulich School of Medicine and Dentistry, and the University of Western Ontario.

# Table of Contents

Abstract.....	i
Co-Authorship Statement.....	iii
Acknowledgments.....	v
Table of Contents .....	vii
List of Tables .....	xii
List of Figures .....	xiii
List of Abbreviations .....	xvi
List of Appendices .....	xviii
CHAPTER 1 .....	1
1 INTRODUCTION .....	1
1.1 Overview and Motivation .....	1
1.2 Drug Efficacy.....	3
1.2.1 Challenges to Drug Bioavailability.....	4
1.2.2 Therapeutic Window and Drug Distribution .....	5
1.2.3 Drug Effectiveness and Adverse Effects (references) .....	7
1.3 Diagnostics.....	7
1.3.1 Magnetic Resonance Imaging.....	7
1.4 Concurrent Theranostic Applications .....	11
1.4.1 Challenges to Concurrent Applications .....	12
1.5 Nanoparticles for theranostics.....	13
1.5.1 Drug Delivery .....	15
1.5.2 Imaging .....	17
1.6 Motivation.....	20



1.7 Thesis Objectives .....	21
1.8 References .....	24
CHAPTER 2 .....	39
2 ENGINEERING LARGE GELATIN NANOSPHERES COATED WITH QUANTUM DOTS FOR TARGETED DELIVERY TO HUMAN OSTEOSARCOMA CELLS WITH ENHANCED CELLULAR INTERNALIZATION.....	39
2.1 Introduction.....	39
2.2 Materials and Methods.....	41
2.2.1 Study Design.....	41
2.2.2 Gelatin Nanosphere Synthesis .....	41
2.2.3 Functionalization of CdSe/ZnS Core Shell Quantum Dots .....	42
2.2.4 Bioconjugation of GNs with anti-human Immunoglobulin G Fab .....	44
2.2.5 QDs incorporating with GNs .....	44
2.2.6 Materials Characterization .....	45
2.2.7 Conjugation Efficiency .....	45
2.2.8 Cell Viability.....	47
2.2.9 Statistical Analysis.....	47
2.3 Results.....	48
2.4 Discussion.....	52
2.5 References.....	55
CHAPTER 3 .....	59
3 CELLULAR INTERACTION INFLUENCED BY SURFACE MODIFICATION STRATEGIES OF GELATIN-BASED NANOPARTICLES .....	59
3.1 Introduction.....	59
3.2 Materials and Methods.....	61
3.2.1 Study Design.....	61

3.2.2	Gelatin Synthesis .....	62
3.2.3	CdSe/ZnS Cysteamine Modified Quantum Dots .....	63
3.2.4	PEG-epoxide Synthesis.....	63
3.2.5	Functionalization Strategy .....	64
3.2.6	Confirmation of QD, anti-IgG and PEG modifications .....	65
3.2.7	Materials Characterization .....	65
3.2.8	Quantification of QD and anti-IgG.....	66
3.2.9	Biocompatibility .....	67
3.2.10	Statistical Analysis.....	67
3.3	Results.....	68
3.4	Discussion.....	75
3.5	References.....	79
CHAPTER 4 .....		83
4	<b>BIMODAL IMAGING COMPATIBLE THERANOSTIC NANOPARTICLES FOR ANTI-ANGIOGENIC TREATMENT</b> .....	83
4.1	Introduction.....	83
4.2	Materials and Methods.....	86
4.2.1	Study Design.....	86
4.2.2	UCNP synthesis surface modification with PEI.....	87
4.2.3	UCNP functionalization with anti-VEGF.....	88
4.2.4	Materials Characterization .....	88
4.2.5	Quantification of anti-VEGF conjugation .....	88
4.2.6	UCNP fluorescence.....	89
4.2.7	Magnetic Properties .....	89
4.2.8	Cell viability.....	89

4.2.9 Immunocytochemistry .....	89
4.2.10 Statistical Analysis.....	91
4.3 Results.....	91
4.4 Discussion.....	98
4.5 References.....	100
CHAPTER 5 .....	106
5 NANOSTRUCTURED BIOSENSOR FOR DETECTING GLUCOSE IN TEAR BY APPLYING FLUORESCENCE RESONANCE ENERGY TRANSFER QUENCHING MECHANISM. ....	106
5.1 Introduction.....	106
5.2 Materials and Methods.....	109
5.2.1 Study Design.....	109
5.2.2 Fabrication of patterned QDs decorated with ZnO nanorod arrays on silicone .....	110
5.2.3 Synthesis of Malachite Green Dextran .....	112
5.2.4 Synthesis and Optimization of the FRET Sensor .....	112
5.2.5 Sensor measurement .....	114
5.2.6 Fluorescence sensor signal converting to image pixel intensity.....	114
5.2.7 Animal tear test.....	115
5.2.8 Statistical Analysis.....	117
5.3 Results.....	117
5.4 Discussion.....	123
5.5 References.....	125
CHAPTER 6 .....	129
6 CONCLUSION AND FUTURE DIRECTIONS.....	129
6.1 Overview of Rationale and Research Questions.....	129

6.2 Summary and Conclusions .....	130
6.3 Limitations .....	132
6.3.1 Study Specific Limitations.....	132
6.3.2 General Limitations .....	134
6.4 Future Directions .....	135
6.4.1 Upconversion nanoparticle based contact lens biosensor for non- invasive glucose detection .....	135
6.4.2 Biomedical collaborations for treatment design .....	137
6.5 Significance and Impact.....	137
6.6 References.....	138
APPENDIX.....	141
Curriculum Vitae .....	144

## List of Tables

<b>Table 1-1.</b> Drug Release Kinetics .....	16
<b>Table 2-1.</b> Hybridization and conjugation quantification .....	49
<b>Table 3-1.</b> Impact of modification order on functionalization. ....	71
<b>Table 4-1.</b> Physical characterization of Gd-UCNPs.....	92
<b>Table 4-2.</b> Percent composition of Gd, Er, and Yb in UCNPs.....	93
<b>Table 5-1.</b> Glucose levels of in rat blood glucose vs tear glucose. ....	122

## List of Figures

<b>Figure 1-1.</b> Applications of antibodies for theranostics.....	2
<b>Figure 1-2.</b> Physical barriers to successful drug delivery .....	6
<b>Figure 1-3.</b> Paramagnetic interaction in Magnetic Resonance Imaging .....	9
<b>Figure 1-4.</b> Enhanced surface area to volume ratio property .....	14
<b>Figure 1-5.</b> Band gap energy of fluorescent quantum dots .....	18
<b>Figure 1-6.</b> Conventional downconversion and upconversion luminescence.....	19
<b>Figure 2-1.</b> Two-step desolvation method of gelatin nanosphere (GNs) synthesis .....	42
<b>Figure 2-2.</b> Synthesis scheme of CdSe/Zn/Cysteamine QDs.....	43
<b>Figure 2-3.</b> Functionalization scheme of Gelatin Nanospheres .....	44
<b>Figure 2-4.</b> Protein standard curve of anti-IgG Fab. ....	46
<b>Figure 2-5.</b> Standard curve of CdSe/ZnS/Cys QDs absorbance .....	47
<b>Figure 2-6.</b> TEM micrographs of 175 bloom GNs.....	48
<b>Figure 2-7.</b> Determination of the interaction between functionalized GNs and UTA-6 cells .....	50
<b>Figure 2-8.</b> Relative viability of osteosarcoma cells incubated with various concentrations of functionalized GNs for 24 hours. ....	52
<b>Figure 3-1.</b> Two-step desolvation method of gelatin nanoparticle (GNP) synthesis.....	62
<b>Figure 3-2.</b> Fluorescence Change of CdSe QD with Subsequent Modifications.....	63
<b>Figure 3-3.</b> Schematic of GNP modifications .....	65

<b>Figure 3-4.</b> Standard Curves .....	66
<b>Figure 3-5.</b> Microstructures of hybrid nanoparticles .....	69
<b>Figure 3-6.</b> Average particle size of functionalized nanoparticles via Paths A and B.....	70
<b>Figure 3-7.</b> Change of free primary amine groups in GNP with subsequent modifications relative to unmodified GNP .....	71
<b>Figure 3-8.</b> Interaction of Path A modified GNP with UTA-6 cells.....	72
<b>Figure 3-9.</b> Cellular Interaction of GNP-anti-Ig/GQD and GNP-anti-IgG/QD/PEG with UTA-6 cells.....	73
<b>Figure 3-10.</b> Average cell viability of functionalized GNP .....	74
<b>Figure 3-11.</b> Relative cellular viability of the GNP model capped with PEG after 24-h incubation.....	75
<b>Figure 4-1.</b> Schematic of the upconversion nanoparticle antibody model.....	86
<b>Figure 4-2.</b> Synthesis schematic of upconversion nanoparticles modified with PEI.....	87
<b>Figure 4-3.</b> Anti-VEGF protein assay standard curve.....	89
<b>Figure 4-4.</b> Chamber preparation for immunocytochemistry .....	90
<b>Figure 4-5.</b> Upconversion antibody model characterization by TEM .....	91
<b>Figure 4-6.</b> FTIR spectrum of the PEI modified NaGdF <sub>4</sub> : Er, Yb UCNPs.....	92
<b>Figure 4-7.</b> Upconversion fluorescence spectra of the NaGdF <sub>4</sub> : Er, Yb UCNPs.....	93
<b>Figure 4-8.</b> Magnetization of the UCNPs .....	94
<b>Figure 4-9.</b> UCNP T1-weighted signal with 3 T magnetic field.....	94
<b>Figure 4-10.</b> Relative cell viability of HUVECs with various treatments for 24 hours...	95

<b>Figure 4-11.</b> Change in cell length as a descriptor for angiogenesis .....	96
<b>Figure 4-12.</b> Confocal images of HUVECs treated with FITC tagged Gd-antiVEGF UCNPs .....	97
<b>Figure 4-13.</b> Confocal images of HUVEC cells .....	98
<b>Figure 5-1.</b> Illustration of the designed FRET transducer made of ConA-conjugating quantum dots (donor) and MG (acceptor) for detecting glucose .....	109
<b>Figure 5-2.</b> A photolithographic lift-off process for fabricating the patterned ZnO nanorod array on silicone hydrogel.....	111
<b>Figure 5-3.</b> Thin layer chromatography confirmation of MG-dextran conjugation .....	112
<b>Figure 5-4.</b> FRET signal optimization .....	113
<b>Figure 5-5.</b> Cell viability of the FRET glucose sensor .....	116
<b>Figure 5-6.</b> Characterization of nanomaterials by electron microscopy.....	118
<b>Figure 5-7.</b> FTIR spectra of the cysteamine (Cys) modified QDs and ZnO nanorod (NR), and the hybrid ZnO NR coated with QDs (ZnO NR-QDs) .....	118
<b>Figure 5-8.</b> Photoluminescence of the glucose sensor .....	120
<b>Figure 5-9.</b> Fluorescence images of the patterned FRET sensor on silicone hydrogel and the relative pixel intensities of the sensors responding to the concentrations of glucose. .....	121
<b>Figure 5-10.</b> Photoluminescence spectra of designed sensor responding to tear samples from rats with different glucose level in blood.....	122
<b>Figure 5-11.</b> Relative Sensing Signal ( $I_{\text{test sample}}/I_{\text{glucose}}$ ) to different biomolecules .....	123
<b>Figure 6-1.</b> UCNP-based glucose sensor .....	136



## List of Abbreviations

AMD	Age-Related Macular Degeneration
ANOVA	Analysis of Variance
Anti-IgG	Anti-Human Immunoglobulin G
Anti-VEGF	Anti-Vascular Endothelial Growth Factors
APS	3-Aminopropyltriethoxysilane
BCA	Bicinchoninic Acid
CDSE	Cadmium Selenium
Con A	Concanavalin A
CT	Computed Tomography
CYP2C9	Cytochrome P450 2C9
CYS	Cysteamine Hydrochloride
DMEM	Dulbecco's Modified Eagle's Medium
EPR	Enhanced Permeability and Retention Effect
Er	Erbium
FITC	Fluorescein Isothiocyanate
FRET	Fluorescence/Forster Resonance Energy Transfer
Gd	Gadolinium
GI	Gastrointestinal
GNs	Gelatin Nanospheres
GNPs	Gelatin Nanoparticles
HDA	hexyldecylamine
HER2	Sample Abbrev.
HUVECs	Human Umbilical Vascular Endothelial Cells
ICC	Immunocytochemistry
IM	Intramuscular
IV	Intravenous
I-131	Radioactive Iodine-131
MG	Malachite Green
MRI	Magnetic Resonance Imaging

MVGS	Microvascular Growth Supplement
NaF	Sodium Flouride
NR	Nanorod
NIR	Near-Infrared
PEG	Polyethylene Glycol
PEI	Polyethylenimine
PET	Positron Emission Tomography
PL	Photolumniscence
PMA	Phorbol 12-Myristate 13-Acetate
PR	Photoresist
RF	Radio-Frequency
SC	Stratum Corneum
SE	Selenium
SEM	Scanning Electron Microscopy
SPECT	Single-Photon Emission Computer Tomography
SPR	Surface Plasmon Resonance
STG	Streptozotocin
TEM	Transmission Electron Microscope
TNBS	2,4,6-Trinitrobenzemesulfonic Acid
TOP	Trioctyl Phosphine
TOPO	Trioctyl Phosphine Oxide
UCNPs	Upconversion Nanoparticles
VSM	Vibrating Sample Magnetometer
Yb	Ytterbium
ZnS	Zinc Sulfide
<sup>18</sup> F	Flourine-18
<sup>99m</sup> Tc	Technetium-99m
<sup>131</sup> I	Iodine-131

## **List of Appendices**

<b>APPENDIX A: Permission for Republication of Scientific Article .....</b>	<b>141</b>
---	------------

## CHAPTER 1

*This chapter provides a general introduction to theranostics, a combination of therapeutics and diagnostics.<sup>1,2</sup> A literature review of current developments and challenges of theranostics is included in this chapter. The motivation and objectives of applying the benefits of nanoparticles for theranostics will be presented.*

### 1 INTRODUCTION

#### 1.1 Overview and Motivation

Theranostics is a constantly evolving field to provide new opportunities in developing new healthcare technologies and medicine at an affordable price.<sup>1</sup> The term theranostic is a combination of therapeutics and diagnostics, spanning a spectrum of research areas such as classical pharmacology and physiology to emerging fields like biotechnology and molecular biology.<sup>2</sup>

Theranostics employ personalized medicine as a core value to provide the best response and highest safety margin to patient care.<sup>3</sup> Variability in drug response is attributed to ethnic diversity, age, epigenetic factors, nutrition, and physiology; which are all routed in genetics.<sup>1,4</sup> As a result of these differences from patient to patient, therapy treatments must be tailored to reflect genetic composition through the selection of appropriate drugs and treatment regimens.

Pharmacogenetics has provided theranostics the framework to build the drug efficacy of personalized medicine, by studying the inherited genetic differences in drug metabolic pathways.<sup>5,6</sup> Non-genetic factors such as age, organ function, and concomitant therapy can affect the treatment process.<sup>7</sup> Through determining genetic makeup, clinicians are able to determine an individual's therapeutic and adverse response to drugs. An example is the anticoagulant warfarin. Through pharmacogenetics, cytochrome P450 2C9 (CYP2C9), the primary enzyme responsible for the metabolism of non-steroidal anti-inflammatory drugs was identified. Variations in the VKORC1 gene that encodes the targeting of warfarin determines the dosage required to elicit an effect.<sup>4</sup> In comparison to

Caucasians, African Americans require a higher dosage of warfarin compared to Asians, who require a lower dose.

Another application of theranostics is in the diagnosis of diseases for treatment planning. Typical technologies include molecular biology, diagnostic radiology, and imaging to diagnose or prognosticate diseases for treatment planning. These technologies work as a cohesive unit, to determine the best course of treatment. Imaging modalities such as magnetic resonance imaging (MRI), computed tomography (CT), and ultrasound, are typically non-invasive unless a tracer or contrast agent is required, provide an anatomical view of tissue, organs, and vasculature hidden by skin and bones.<sup>8-11</sup> In conjunction with molecular biology, diseases can be classified by probing for molecular targets with antibodies for antigens, cell surface receptors, and over-expressed molecules (**Figure 1-1**).<sup>12,13</sup> HER2, the human epidermal growth factor receptor 2 oncogene, is a measurable and detectable tyrosine kinase amplified in 15-20% of breast cancers and gastrointestinal cancers.<sup>5,14</sup> Accurate determination of the HER2 status is critical in optimizing patient response to clinical treatments.

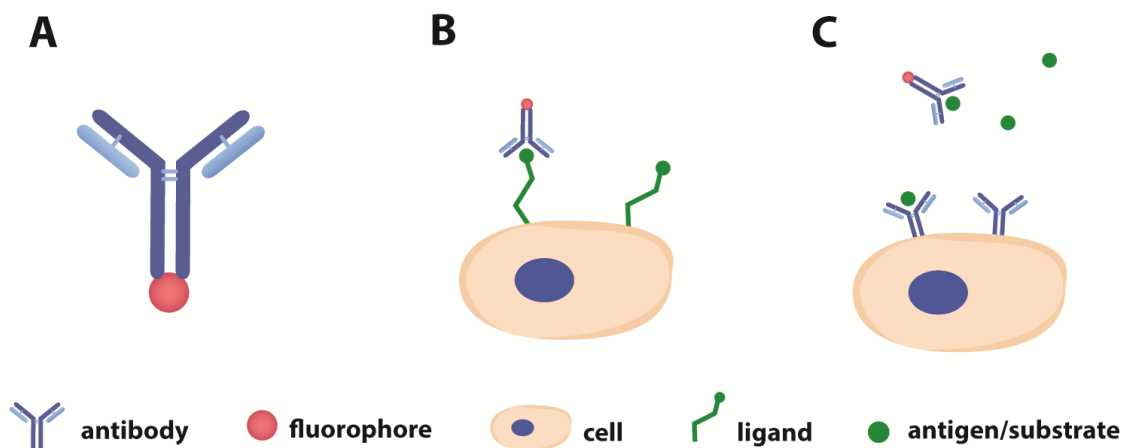


**Figure 1-1.** Antibody applications for theranostics. A) Fluorophore tagged antibody structure for molecular biology. B) Provide cellular specificity by targeting cell surface ligands for identification or treatment. C) Extracellular targeting of free floating antigens or substrates to inhibit signal transduction.

Concurrent applications for simultaneous therapy and diagnostics are possible. The earliest known theranostic particle was through the use of radioactive iodine-131 (I-131,

<sup>131</sup>I) to provide diagnostic capabilities and therapeutic abilities.<sup>15</sup> With a half-life of approximately 8 days, it is suitable to provide both pre-therapy and post-therapy imaging in addition to treating thyroid cancer. Other instances include radiolabeled and/or optically tagged enzyme inhibitors and binding antibodies as effective tools for imaging and therapy of cancer.<sup>13,16</sup> The optical tagged and radiolabeling provides a method of tracking and locating the molecules upon administration, whereas the antibody itself elicits a therapeutic response only.

The application of theranostics can be summarized with 3 possible scenarios:

- a) drug efficacy – assessment of drug effectiveness;
- b) diagnostics – diagnosis followed by therapy;
- c) concurrent – simultaneous application of therapy and diagnostics.

As current medical technologies continue to evolve and improve, a deeper understanding of potential drawbacks and disadvantages must be understood and addressed in order to move forward. Disadvantages such as adverse effects of drugs,<sup>6,17-19</sup> overcoming physiological barriers (e.g. blood-brain barrier, retinal-blood barrier, membranes and linings)<sup>20-22</sup> and imaging limitations are pertinent in evolving pharmaceuticals.<sup>23-26</sup>

## 1.2 Drug Efficacy

The earliest and most rudimentary forms of therapeutic treatment are as old as humanity itself utilizing natural remedies to treat wounds and diseases.<sup>27</sup> Remedies were prepared by boiling ingredients in water; a primitive liquid dosage form or mixing with components (e.g. fats) to enable a prolonged effect on the application site. As our understanding of medicine deepened and broadened, the evolution of therapeutic technology and diagnostic capabilities developed to reflect this. Advanced fields of pharmacokinetics and biopharmacy emerged from advancements in pharmacology and physiology.

Early developments in pharmaceuticals consisted primarily of simple, fast-acting low molecular weight molecules applied orally as solid and liquids or administered by injection or infusion.<sup>28</sup> These traditional dosage forms were highly time consuming to

make in addition to a fast drug release resulting in the high frequency of intake. The first generation of controlled release or rate-programmed drug release systems materialized in the 1970s with the aim of prolonging drug release.<sup>28,29</sup> These formulations released the drug of choice at a predictable and predetermined rate to minimize intake and maintaining constant drug levels to maintain a therapeutic effect.<sup>27</sup> Other forms of administration include pills, injections, and suppositories whose release is controlled by dissolution, diffusion, erosion, or osmotic mechanisms.<sup>27,30</sup>

Typical routes of drug administration include enteric (oral, peroral, rectal), parenteral (intravascular, intramuscular, subcutaneous), or topical (skin and mucosal membranes).<sup>31,32</sup> Therapeutics formulated for these administrative routes through pharmacokinetic studies, are optimized for bioavailability, efficacious delivery to the appropriate site, minimize toxicity, reduced side effects, and improved stability of the drug.<sup>32,33</sup> These typical administrative routes have respective advantages and disadvantages.

### **1.2.1 Challenges to Drug Bioavailability.**

Bioavailability, the rate and extent drug molecules are absorbed and become available at the site of action,<sup>34</sup> can be affected by routes of administration<sup>5,32</sup> which in turn are limited by biological barriers.<sup>20,21</sup> Common routes of administration include oral, injections, and topical are impeded by physiological barriers which aid to naturally protect the human body.

Oral delivery of drugs is limited by the gastrointestinal digestive environment, intestinal epithelial cells, and tight junctions.<sup>21</sup> The gastrointestinal (GI) environment degrades macromolecules with the help of digestive enzymes and its acidic environment to limit its effectiveness.<sup>32</sup> Furthermore, assuming the drug maintains its chemical structure, absorption through intestinal epithelial cells present at the small intestine and colon can be further impeded. The intestinal epithelial barrier presents a large absorptive surface requiring cell penetrating peptides for endocytosis and/or diffusion, and transcytosis to facilitate drug transport.<sup>21,35,36</sup> Highly dependent on its chemical properties, a lipophilic drug may simply pass through the phospholipid bilayer through simple diffusion, whereas

polarized drugs require endocytosis as a mechanism to facilitate transport into systemic circulation. Drugs considered unsuitable for oral delivery or causes patient discomfort with swallowing may require other routes of administration such as injections or topical applications.

Injections of pharmaceuticals can be subcutaneous, intramuscular (IM), or intravenous (IV) to yield rapid absorption and distribution by bypassing the GI tract. By far IV administration produces the quickest response, though systemic circulation can rapidly dilute the drug. IM administration in comparison has a longer duration of effect as its formulation is designed to provide slow, sustained release over a period of time into the blood stream.<sup>37</sup> IV injections can prevent local irritation, induration, skin discoloration, inflammation, and granuloma formation associated with subcutaneous and IM injections but may cause discomfort as it is invasive.<sup>37,38</sup>

Topical administration replaces the need for invasive drug administrative techniques which may cause discomfort. Topical applications include lotions, creams, and eye drops applied to a localized area rather than systematically.<sup>17,39</sup> Applications to the skin is limited by the outermost few microns of skin, the stratum corneum (SC), is the least permeable of skin layers.<sup>40</sup> Permeability from the skin's surface to the site of action is limited by the lipophilicity of the drug to diffuse through the SC and its aqueous solubility once through the barrier. Diffusion is key to the transport of topical drugs through the skin, but requires high concentrations with the risk of skin irritation.<sup>39,41</sup>

Regardless of the method of drug delivery, the key limitation to an appropriate route of administration lies with a patient's comfort as well as the bioavailability of the drug once it is systematically absorbed. Once absorbed, the remaining limitation lies in the drug's ability to diffuse to the site of action from the site of administration.

## **1.2.2 Therapeutic Window and Drug Distribution**

The therapeutic window or safety window refers to a range of doses that defines efficacy and toxicity commonly studied by pharmacodynamics.<sup>42,43</sup> Efficacious effect at the site of action requires a minimal threshold of the drug to illicit its therapeutic effect; however



natural physiological processes may hinder a drug's ability to be delivered. Processes such as hepatic first pass,<sup>39,42,43</sup> loss by diffusion through fenestrations into the capillary endothelium,<sup>36,44</sup> and previously mentioned barriers in addition to limitations of drug administration routes all contribute to lowered drug concentrations (**Figure 1-2**).<sup>34</sup>

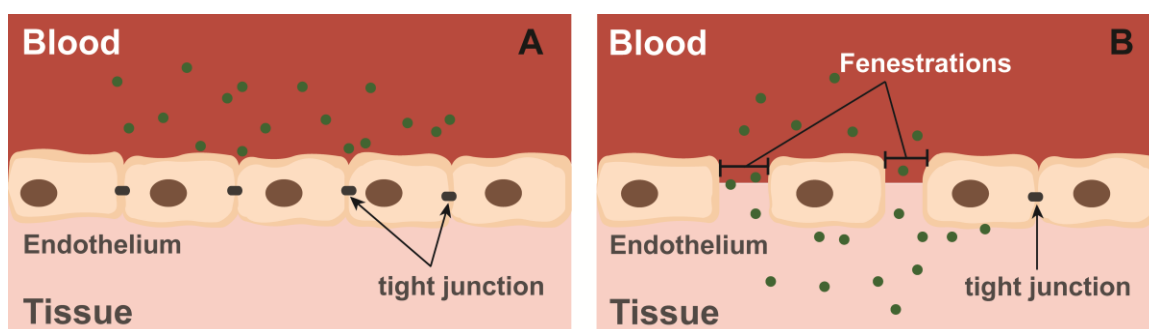


**Figure 1-2.** Physical barriers to successful drug delivery. A) Natural barriers such as the blood-brain barrier and blood-retinal barrier are composed of tight junctions preventing the diffusion and transfer of solutes through the barrier to the tissue of interest. B) Diffusion from the tissue through fenestrations in the capillary endothelium into the blood stream or vice versa is caused by the concentration gradient of solutes.

Upon oral administration, drug elimination is hindered by the first pass effect or pre-systemic metabolism where drug concentration is greatly reduced by hepatic portal system before reaching systemic circulation.<sup>42,45</sup> This effect can occur in the GI tract but the liver is mainly responsible for drug metabolism for elimination as it has the highest metabolic biotransformation capacity.<sup>45</sup> The splanchnic system's organs are arranged such that the intestines and liver act as a barrier for drug distribution.

Diffusion between the interstitial space and the capillary for system circulation in addition to the capillary endothelium are barriers to overcome. The diffusion pharmacokinetics can be assessed using a compartment model of the vascular circulation through capillaries and interstitial space.<sup>32,36</sup> Essentially the flux of drug particles drive diffusion through a biological membrane into either side of the compartment model depending on the concentration gradient. In the case of IV, the first pass effect is avoided leading to direct diffusion into the site of action. However for IM administration, localization at the site of action for drugs smaller than 69 kDa becomes ineffective, as

capillaries in general circulation possess fenestrated gaps between 6-7 nm for transcytosis.<sup>36,46</sup>

### **1.2.3 Drug Effectiveness and Adverse Effects (references)**

A drug's effectiveness is evaluated on potency, efficacy, or effectiveness.<sup>47</sup> Potency measures the minimal amount of drug required to produce an effect. Efficacy measures the drug's capacity to produce an indicated effect or the strength of the indicated effect. The effectiveness however, a measure of how well a drug works, encompasses potency, efficacy, and potential adverse drug reactions. Effectiveness of a drug for pharmaceutical applications requires risk-benefit analysis, dosage scheduling for duration of effect, and adverse effects.

Adverse effects are a general umbrella term to describe unintended effects that occur within the therapeutic range – the dosage range in blood plasma or serum required to achieve a therapeutic effect. Adverse effects are common forms of iatrogenic injury resultant of overdosing accidentally or enhanced absorption by alternate routes during appropriate use, and at times interactions between multiple drugs.<sup>17,18</sup> Aside from overingestion, overdosing can occur through topical and systemic routes.<sup>17</sup> Careful control of drug administration routes and dosages are required to maximize effectiveness.

## **1.3 Diagnostics**

Diagnostic components of theranostics is realized by molecular imaging techniques, medical imaging modalities, and immunoassays.<sup>12,48</sup> These techniques aid disease diagnoses from the molecular level to the macroscopic level such as the identification of specific cell markers to the localization of anatomical features. The segmentation of regions of interest in diagnostic imaging is complemented by immunoassays for disease confirmation.

### **1.3.1 Magnetic Resonance Imaging**

Magnetic resonance (MR) relies on certain atomic nuclei to absorb and emit radio frequency (RF) energy when placed in an external magnetic field. Hydrogen atoms being

the most abundant nuclei in biological organisms, found in water and fat, are often used to generate a detectable RF signal which can be translated into an image.

Atomic nuclei possess spin or intrinsic spin angular momentum rotating about an axis at a constant rate.<sup>49</sup> MR measurements consider a collection of similar spins as a single entity. Consider an arbitrary volume of hydrogen atoms (protons) placed into an external magnetic field ( $B_0$ ). The protons will precess about the magnetic field or rotate perpendicularly. Their axis of precession is parallel to  $B_0$  even if the proton vectors are tightly slightly away. The rate or frequency of precession shown in **Equation 1-1** is proportional to the strength of the magnetic field is expressed by the Larmor Frequency.<sup>49</sup>

### Equation 1-1

$$\omega_0 = \frac{\gamma B_0}{2\pi}$$

Where Larmor Frequency ( $\omega_0$ ) is expressed in megahertz (MHz) and  $B_0$  in tesla (T). The atom specific  $\gamma$ , the gyromagnetic ratio, is expressed in  $s^{-1}T^{-1}$ . As a result, the protons have a net magnetization ( $M_0$ ) that is parallel and proportional to  $B_0$  (Equation 1-2)<sup>50</sup>.

### Equation 1-2

$$M_0 = \chi B_0$$

The magnetic susceptibility ( $\chi$ ) is a dimensionless proportionality constant characterizing a material's readiness to develop a magnetic moment on exposure to an external magnetic field. Positive values of  $\chi$  are called paramagnetic materials, whereas negative are diamagnetic.<sup>51</sup>

In MRI, the net magnetization ( $M_0$ ) is manipulated with a short RF burst of excitation energy ( $B_1$ ). During the pulse, the protons absorb a portion of energy at its Larmor Frequency resulting in a shift in the vector of  $M_0$  such that it is no longer perpendicular to  $B_0$ . If enough energy is absorbed,  $M_0$  may rotate into the transverse plane due to 90° pulse. Once  $B_1$  is turned off, the protons will realign with  $B_0$  while emitting energy at  $\omega_0$  (**Figure 1-3a**).<sup>49,50</sup>

Magnetic resonance imaging can provide anatomical and morphological references, as well as *in vivo* bioactivity for disease diagnoses based on the detected radio waves.<sup>23,25</sup> In addition, heavy metal-based contrast agents are valuable assets in enhancing contrast in images and perfusion analyses.<sup>9,52</sup> Monitoring of vascular, cerebral, and tumour perfusion is possible by deriving tracer concentration-time curve.<sup>9,52,53</sup>

Gadolinium-based compounds are typical T1 weighted MRI contrast agents, a chelated paramagnetic metal, which enhances the longitudinal relaxation of tissue's net magnetization vector.<sup>50</sup> The paramagnetic property is a result of unpaired electron spins in certain electron orbital shells of transition and lanthanide metals which exhibit a different magnetic susceptibility that is higher than protons.<sup>49</sup> Protons in close contact with the paramagnetic material experience both the magnetic field of the contrast agent and  $B_0$ , resulting in an increase in perceived magnetic fields, thus altering T1 imaging. The resulting image does not visualize the contrast agent but rather the MR signal of surrounding protons have a shortened relaxation time.<sup>50</sup> The paramagnetic materials, which have the positive  $\chi$ , pulls the magnetic field into the materials whereas objects with negative  $\chi$  pushes (**Figure 1-3b**).<sup>51</sup>

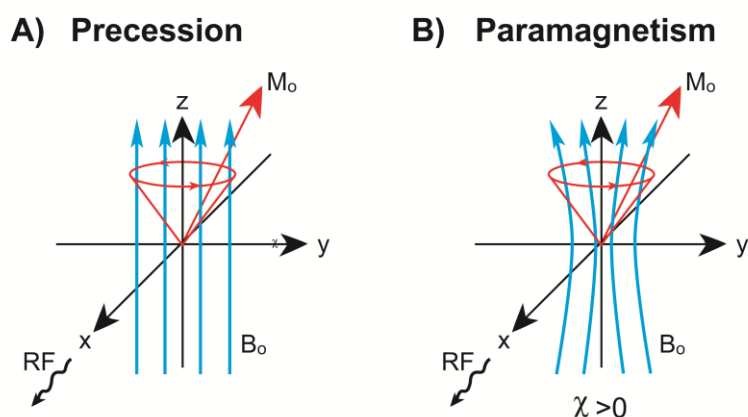


**Figure 1-3.** Paramagnetic interaction in Magnetic Resonance Imaging. A) Precession of protons in a magnetic field. B) Paramagnetic materials, materials with a magnetic susceptibility greater than zero ( $\chi > 0$ ), will influence the surrounding protons by pulling the magnetic field inwards resulting in the increase of relaxation rates (T1 and T2 rates) and signal intensity on T1-weighted images.

### 1.3.1.1 Challenges to Magnetic Contrast Agents

Application of gadolinium-based contrast agents can result in adverse reactions. Heavy metal toxicity is a possible adverse effect if gadolinium is isolated in its free ionic form ( $Gd^{3+}$ ) where it can precipitate in various tissues with no natural excretion pathway. A weak binding between Gd and its chelator, as determined by its dissociation constant, can result in transmetallation where it is replaced by endogenous iron, calcium, zinc, and copper.<sup>23,24,54</sup> Upon release, Gd can bind phosphates to interfere with cation channels leading to splenic degeneration, liver necrosis, enzyme inhibition, interference with synaptic transmitters/receptors, and hematological abnormalities.<sup>23</sup> Immediate adverse hypersensitivity reactions are possible in 0.06-0.3% of patients within 1 hour of contrast exposure, resulting in allergy-like symptoms and physiological responses such as nausea, vomiting, and altered taste.<sup>54</sup>

Though gadolinium-based contrast agents have been introduced into clinical practice roughly 3 decades ago, recent pharmacokinetic findings from analytical techniques have detected the presence of insoluble gadolinium salts (eg: gadolinium phosphate, bicarbonate) in the brain; normally undetectable by both T1 and T2 imaging.<sup>55</sup> Cases of neurotoxicity as reported by Hui et al.<sup>56</sup> and Maramattom et al.<sup>57</sup> is resultant of gadolinium accumulation in patients receiving repeated or large doses of contrast agents. Accumulation has been reported within the extracellular neural tissue, endothelial walls, and basal ganglia, with impaired renal function has been confirmed as a factor contributing to the increased accumulation.<sup>24,55,58</sup> It is known intravenously administrated Gd slowly pass through the blood brain barrier through proposed mechanisms involving transmetallation, specific metal transports, passage through the cerebral spinal fluid, perivascular spaces, and even the glymphatic system.<sup>24</sup> This unexpected finding is attributed to nephrogenic systemic fibrosis, encephalopathy, and inhibition of regular neurological function (eg: visual memory and reasoning, reading comprehension, and math abilities).<sup>23,58</sup>

## 1.4 Concurrent Theranostic Applications

Molecular imaging is an effective demonstration of concurrent theranostic applications – to provide critical diagnostic information with regards to anatomic or cellular targets to induce a therapeutic effect *in vivo* and *in vitro*. An example of early clinical applications utilizes traditional nuclear medicine for the treatment of differentiated thyroid cancer. Radioactive iodine (ex: I-131), dating back to the mid-1940s, was the first theranostic agent to provide both diagnostic and therapeutic capabilities.<sup>15,48</sup> This high energy tracer was used diagnostically for both pre-therapy imaging and radiopharmaceutical post-therapy CT imaging due to its 8 day half-life. As an adjunct therapeutic treatment, <sup>131</sup>I was used in ablative therapy for differentiated thyroid cancers and metastatic diseases.<sup>48</sup> With advancements in molecular biology, new approaches emerged through the use of therapeutic drugs or antibodies to achieve specificity coupled with alternative modes of imaging.

Biocompatible applications require the direct conjugation of fluorescent dyes, radionuclides, and contrast agents to antibodies or enzymes to customize a trackable therapeutic agents to interfere with aberrant targets or disease pathways.<sup>16,59–61</sup> Radionuclides have diverse applications aside from CT as they are compatible with Positron Emission Tomography (PET, ex: <sup>18</sup>F)<sup>62</sup> and Single-Photon Emission Computer Tomography (SPECT, ex: <sup>99m</sup>Tc, <sup>131</sup>I)<sup>13,61</sup> which provide metabolic and functional information to complement CT and MRI anatomic images. Current theranostic applications for cancer utilize antibodies to target the cell membrane or ligands with the addition of radionuclides to increase treatment efficacy.<sup>16</sup> These same conjugates can also be applied to immunohistochemistry for cell biomarker assessment, such as the Hercep Test for breast tumors.<sup>5,14</sup> In clinical practices, scans of the radionuclides may be performed repetitively to assess modulation over time and the bioavailability measured.

The same technology can be applied to MRI by conjugating the therapeutic antibody directly to the gadolinium chelator to promote localization within tumours. As Orcutt et al. have demonstrated, with DOTA chelated with various radionuclides (yttrium, lutetium, and gadolinium) modified with the monoclonal antibody 2D12.5 to enhance

accumulation within the tumor.<sup>59</sup> Grum et al. presented a two domain fusion protein Zarvin capable of binding to a therapeutic immunoglobulin G antibody for targeting while facilitating high affinity binding sites for Gd.<sup>63</sup>

A fluorescent alternative can be produced for superficial and *in vitro* applications as demonstrated by fluorescent microscopy, which has widely been used in the fields of molecular biology, immunochemistry, and assays to identify proteins of choice.<sup>64</sup> The same can be applied by conjugating fluorescent dyes to therapeutics which can be antibodies, microRNAs, antibiotics to study their effects.<sup>12,65,66</sup> As Oosten et al. have demonstrated, fluorescently labelled vancomycin able to identify gram-positive bacterial infections in a murine model *in vivo* and a human cadaver in real time. As for miRNA, it is understood their dysregulated expression is implicated in various human diseases. The addition of a fluorescent tag, provides valuable information in gene expression and results in further understanding pathways to target in cancer.<sup>65</sup> Its implementation can extend to cardiovascular diseases, neurological diseases, and viral diseases.<sup>67-69</sup>

### 1.4.1 Challenges to Concurrent Applications

Though current diagnostic imaging techniques have proven to be effective, there are limitations which may inhibit a product to reach its maximum potential. As previously mentioned, the application of gadolinium-based contrast agents can result in adverse effects. Another limitation in order for the contrast agent to be effective is to achieve a minimal threshold to which it can yield its effect. The chance of unnecessary overexposure to ionizing radiation when using CT or radioisotopes have also prompted a shift towards other imaging modalities such as MRI and fluorescence.<sup>70</sup>

Fluorescence imaging, in addition to being a nonisotopic method of detection, can open new possibilities for ultrasensitive high-resolution detection. One concern is photobleaching, where a fluorophore loses its fluorescent signal over time as a result of repetitive stimulation.<sup>71,72</sup> In clinical applications, fluorescence imaging lacks tissue penetration as the very small structures and boundaries in cells absorb and scatter photons in the visible range.<sup>73</sup> The reciprocal of the absorption coefficient ( $\mu_a$ ) and scattering coefficient ( $\mu_s$ ), with units  $\text{cm}^{-1}$  or  $\text{mm}^{-1}$ , yields the mean free path or the average distance

traveled. Cytochroms and hemoglobin are the most common absorbers in cells, resulting in a mean free path of less than 1cm ( $\mu_a \gg 1\text{cm}^{-1}$ ). The fluorescence excitation wavelength, typically 350 nm to 800 nm, can result in genotoxic effects-damage to the genetic structure.<sup>74</sup> Though the mechanisms of light-induced genotoxicity vary by wavelength, the implications of mutagenicity and carcinogenicity resultant of light irradiation is clear.<sup>75-77</sup>

## 1.5 Nanoparticles for theranostics

Early application of nanoparticles dates back to the 9<sup>th</sup> century in Mesopotamia and the middle ages where colloidal silver and gold was used to produce luster. This metallic film was applied to the transparent surface of a glazing to provide a glittering effect on the surface of pots.<sup>78,79</sup> This film was found to resist atmospheric oxidation and weathering. The metal salts in combination with vinegar, ochre, and clay under a reducing atmosphere and a kiln heated to 600°C was the ideal environment to form nanoparticle aggregates with specific colours and optical effects.<sup>79</sup> It was Faraday who first provided the scientific description for the observed optical effects in 1857.<sup>80,81</sup>

It was not until the last few decades that our knowledge and understanding in science brought nanoparticles to the forefront of enhancing biomedical technology. Partially because of the diversity in material composition, these same particles exhibit size-related properties at the nanoscale ( $10^{-9}$  m) not seen in their bulk form; quantum confinement,<sup>82-86</sup> surface plasmon resonance,<sup>87,88</sup> superparamagnetism,<sup>89,90</sup> paramagnetism,<sup>91,92</sup> and high surface area to volume ratio (**Figure 1-4**).<sup>93</sup> As a result, these material dependent characteristics can be tailored or modified for specific applications or integrated together for more versatile biomedical purposes.

One key advantage of nanoparticles for biomedical applications such as; biosensors, multimodal compatible imaging, and drug delivery is the potential for personalized medicine at a fraction of the cost of current healthcare. A nanosized particle customized to meet the needs of an individual patient may potentially cross natural barriers and enter tissue through different portals of entry or interact with biomolecules in the blood.<sup>94</sup> In the case of cancer, molecular targets and chemotherapy drugs are often rendered



ineffective as the cancer cells will evolve ways to survive one oncogenic pathway.<sup>95</sup> It is more beneficial to target several pathways simultaneous with a drug cocktail than to target an isolated pathway. Nanoparticles offer the potential to not only encapsulate and provide sustained release of cancer drugs, but also aid to localize the cells within tumours as they lack lymphatic drainage to eliminate the nanoparticles enhanced permeability and retention effect (EPR).<sup>96</sup>

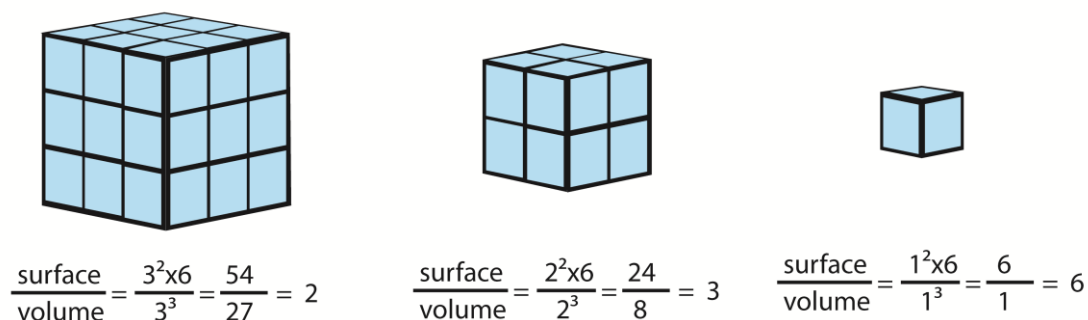


**Figure 1-4.** Enhanced surface area to volume ratio. The increased surface area to volume maximizes ample surface area for nanoparticle post-synthesis modifications.

The material-dependent properties extend beyond those of metals. Organic biodegradable polymers (ie: gelatin, chitosan, liposomes)<sup>97-99</sup> and synthetic biocompatible polymers (ie: poly-lactic acid, poly-caprolactone)<sup>100,101</sup> exhibit material specific set of characteristics perfect for drug encapsulation and sustained drug release. Unlike its metallic counterparts which are synthesized into a crystal lattice solid core organized at the atomic level, biodegradable and biocompatible nanoparticles form hollow shells with morphological pores in some cases. Encapsulation process, release profiles, and even pore size can be controlled during the synthesis process to tune its physical characteristics.<sup>102-104</sup>

The development of nanoparticles is a revolutionary advancement for biomedical technology. The nanoscale particulates exemplify a unique set of characteristics through reshaping materials in current technologies such as gelatin for soft gel encapsulation<sup>105</sup> or gadolinium for imaging.<sup>106</sup> Applications of nanoparticles in biotechnology include improved drug delivery and enhanced accumulation by EPR, new imaging technologies, and highly sensitive biosensors that can mitigate negative effects or enhance overall effectiveness.

### 1.5.1 Drug Delivery

Nanoparticle drug encapsulators demonstrate various advantages over current delivery technologies. Varying in material, drug delivery nanoparticles offer both biodegradability and biocompatibility. These systems provide a matrix for therapeutic immobilization, adsorption, bioconjugation/attachment, and encapsulation, allowing for controlled release profiles which directly affects drug bioavailability and its therapeutic index.<sup>103,104</sup> The controlled release profiles differ according to the method and conditions of synthesis, base material, and potential modification. The consensus regardless of material and method demonstrates the following advantages: 1) drug loading in nanoparticles achieved is relatively high with the preservation of drug activity, 2) provide site-specific localization with ligand modification, 3) improve pharmacokinetics and reduced adverse reactions, and 4) increased stability of drug by protecting against chemical and enzymatic degradation, and elimination.<sup>30,32,103,104,107</sup>

Organic nanoparticles synthesized from animal proteins (ex: gelatin, collagen, chitosan) have a low cytotoxic end product (metabolite or product of degradation).<sup>98,108</sup> As demonstrated by Vandervoort et al., the successful encapsulation of a drug was dependent on the solubility of the drug of choice in the synthesis environment.<sup>109</sup> Exemplified by gelatin nanoparticles synthesized by a desolvation method, the dehydration of protein in an aqueous solution with an organic solvent (alcohol or acetone) to change from a stretched to coiled conformation, demonstrated a higher encapsulation efficiency for hydrophilic drugs rather than hydrophobic drugs. Synthesis methods employed for drug encapsulation include desolvation, coacervation, emulsification, ionic gelation and nanoprecipitation.<sup>97,104,110</sup>

Regardless of material and synthesis method, drug loading and drug release are key factors for a successful drug delivering nanoparticle. Firstly, drug loading is achieved by incorporation during the synthesis process or post-synthesis by mixing the carrier with a concentrated drug solution (adsorption or absorption).<sup>111</sup> Drug loading is characterized by the ratio of drug encapsulated or absorbed (moles or mg) per nanoparticle weight

(mg), which can be optimized by measuring the encapsulation efficiency or ratio of drug loaded to the total amount of drug used (Equation 1-3).<sup>36</sup>

### Equation 1-3

$$\text{Encapsulation Efficiency (\%)} = \frac{(W - w)X100}{W} = \frac{\text{Amount Loaded}}{\text{Total Amount Used}} X100$$

Drug release however is governed by not only the solubility of the drug, but the diffusion through the nanoparticle matrix or pores, nanoparticle degradation, and the processes of erosion and diffusion.<sup>32,111</sup> Typical release is governed by zero order kinetics or first order kinetics, a function of time or concentration, respectively (**Table 1-1**).<sup>32,112</sup>

**Table 1-1.** Drug Release Kinetics

Zero Order	First Order
$C_t = C_0 + K_0t$	$\ln C_t = \ln C_1 - Kt$

t: time, C<sub>0</sub>: initial burst release of drug, K<sub>0</sub>: zero-order rate constant, C<sub>1</sub>: initial concentration of drug, K: first order rate constant

Furthermore, the surface chemistry of protein nanoparticle can be functionalized due to the presence of surface functional groups to affect biodistribution, biocompatibility, and stability.<sup>113,114</sup> Typical surface functional groups of the protein (amine, carboxyl, and thiol groups) exposed by the conformational changes of the protein macromolecules can be crosslinked to provide stability and/or bioconjugation of ligands (targeting moieties and therapeutic protein).<sup>107,115,116</sup> As a result of post-synthesis surface modifications, 290003476271 these nanoparticles demonstrated enhanced cellular uptake and association. Balthasar et al., demonstrated the attachment of biotinylated anti-CD3 antibodies to the surface of gelatin nanoparticles were promising carriers for delivering drugs to T-lymphocytes through the formation of an avidin-biotin complex.<sup>117</sup> The addition of polyethylene glycol (PEG), an example of a targeting moiety, to the surface of nanoparticles can lengthen circulation time of drug loaded nanoparticles and decrease immunogenicity to increase bioavailability and biodistribution in patients.<sup>118,119</sup>

## 1.5.2 Imaging

In contrast to organic nanoparticles, metallic nanoparticles exhibit a completely different set of properties suitable for imaging such as downconversion fluorescence, upconversion fluorescence, paramagnetism, and superparamagnetism.<sup>83,84,90,92</sup> Applications for such imaging technology not only address the limitations of current imaging technologies such as toxicity, adverse reactions, and photobleaching, but allow for the sensitivity to track individual cells and tuning of detectable optical spectra. Voura et al., demonstrated the *in vivo* application of quantum dots to study the extravasation of tumour cells as a model for tracking metastasizing cancer cells.<sup>82</sup> The physical composition of the nanoparticle, transition and post-transition metals (ie: iron, cadmium, lead, indium) or lanthanides (ie: gadolinium, erbium, ytterbium), attributes to the various optical and magnetic properties measured or observed.<sup>72,89,120</sup>

### 1.5.2.1 Quantum Dots

Semiconductive nanoparticles or quantum dots (QDs) exhibit quantum confinement properties resistant to photobleaching as observed in fluorescent dyes.<sup>121,122</sup> The resultant photobleaching involves the triplet state, where upon photon absorption, a fluorophore transits from the ground to first singlet-excited state.<sup>123</sup> This can also transition into the triplet-excited state, associated with higher energy (>1 eV) and longer lifetime ( $\sim 10^2$   $\mu$ s), facilitates chemical reactions that results in fluorophore bleaching.<sup>123-125</sup> The photoluminescence observed is the result of quantum confinement in the nanoscale dimension where an electron is confined to dimensions smaller than its Bohr radius. The density of states decreases near the conduction band and valence band to form discrete quantifiable energy states or band gaps characterized by an electron-hole pair (**Figure 1-5**). This band gap energy is responsible for the observed emissions that can be tuned by controlling nanoparticle size; an increased energy is associated with decreasing nanoparticle size.<sup>122,126</sup> With a broad excitation spectra, an exciton (electron to be excited) will jump into the covalent band or excited state, leaving a hole. Upon returning to ground state and recombining with the hole, electromagnetic energy with a narrow profile will be emitted within the UV to near infrared spectra.<sup>126</sup>

QDs are synthesized from organometallic precursors at temperatures of 300°C or higher and varying nucleation duration to control the growth of nanoparticles in a solvothermal reaction.<sup>71,82</sup> Nanoparticles from both group II-VI (eg: CdSe, CdTe, and CdS) and group III-V (eg: InP and InAs) have been extensively studied.<sup>71,121</sup> This method of synthesis requires surface functionalization to render them water-soluble and biocompatible.<sup>127,128</sup>

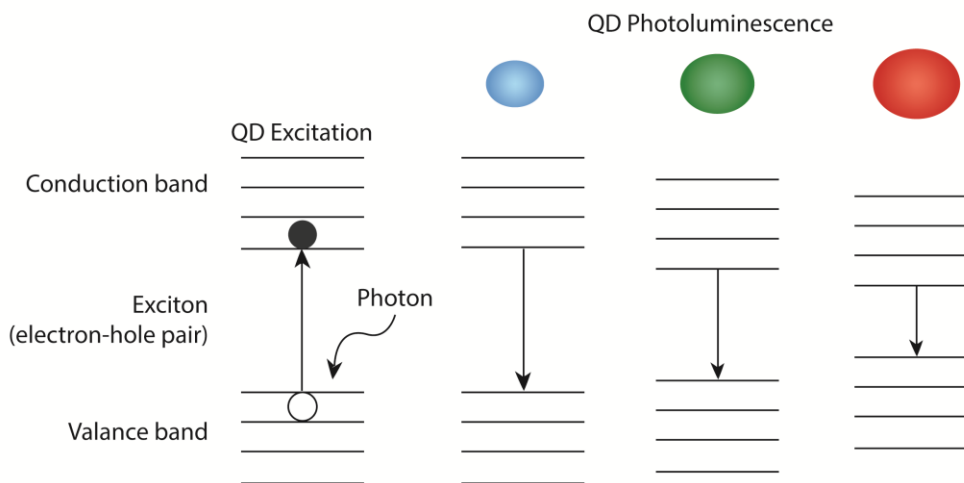


**Figure 1-5.** Band gap energy of fluorescent quantum dots. QD fluorescence is defined by its band gap, which corresponds to its size, to produce the detected fluorescence. A larger band gap is associated with a smaller QD to cause a blue Stokes Shift resulting in a higher energy emission.

With a modicum of success, QDs have demonstrated biocompatible applications for cellular imaging and molecular biology. Modified QDs exhibited internalization by cell lines such as HeLa, UTA-6 osteosarcoma, hepatocytes by receptor-mediated endocytosis or phagocytosis demonstrated low cytotoxicity.<sup>70,72,120,128,129</sup> Furthermore, upon introduction into murine models, QDs were visualized through the skin in capillaries hundreds of micrometers deep.<sup>127</sup> In murine with C4-2 tumour xenografts, the QDs were uptaken and retained within the tumor cells.<sup>72,84</sup>

### 1.5.2.2 Upconversion Nanoparticles

Where QDs exhibit a Stokes shift when excited, emitted photon with a longer wavelength and lower energy than the absorbed light, upconversion nanoparticles (UCNPs) demonstrate the opposite (**Figure 1-6**).<sup>130</sup> Upconversion through a multiphoton

conversion process transmits multiple lower energy photons from near-infrared (NIR) lights to a higher energy photon which is emitted.<sup>85,86</sup> Similar to QDs, UCNPs are synthesized at high temperatures through a solvothermal or hydrothermal reactions with lanthanide pairs to produce the upconversion phenomena from NIR light (700-1700 nm).<sup>86,120,131</sup> The resultant lanthanide dopant pairs, donors (ex:  $\text{Yb}^{3+}$ ) and acceptors (ex:  $\text{Tm}^{3+}$ ,  $\text{Pr}^{3+}$ , and  $\text{Er}^{3+}$ ), form an energy-transfer network within a single nanoparticle.<sup>85,106,131–133</sup>

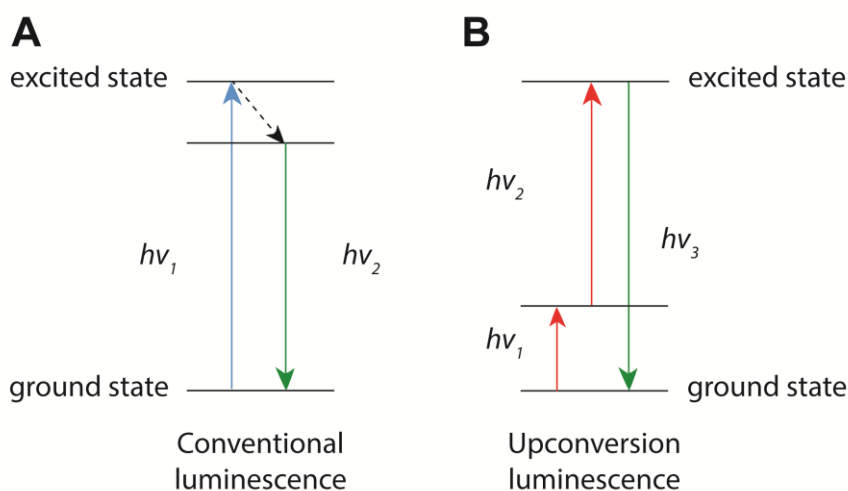


**Figure 1-6.** Conventional downconversion and upconversion luminescence. A) Conventional downconversion luminescence is characterized by a higher energy excitation photon and a lower energy emission photon ( $h\nu_1 > h\nu_2$ ). B) Upconversion luminescence, through a multiphoton excitation method will cause transfer the lower energies of multiple excitation photons to a higher energy emission photon ( $h\nu_3 > h\nu_1, h\nu_2$ ).

The application of NIR UCNPs for biotechnology is desirable for its “optical transparency window” which provides deeper light penetration and reduced photodamaging effects.<sup>106,133,134</sup> Photodamage or phototoxicity can result from the application of higher energy light such as UV as an excitation source resulting in damage to DNA.<sup>75,77,135</sup> The cytotoxicity of the UCNPs are not only less than that of QDs, but possess a stronger fluorescence signal as well.<sup>134</sup> In comparison, the lanthanide pairs of Yb/Er or Yb/Tm has been reported to show seven orders of magnitude higher than that of CdSe-ZnS QDs.<sup>127,134</sup>

### 1.5.2.3 Gadolinium-based contrast agents and Bimodal Imaging

The next generation of gadolinium-based contrast agents is a potential for bimodal magnetic resonance and upconversion fluorescence imaging. The crystal lattice structure of fluoride-based nanoparticle provides the optimal stability to prevent lanthanide ion dissociation.<sup>120,134,136,137</sup> Similar to the synthesis of upconversion nanoparticles, the core constituent of NaGdF<sub>4</sub> that provides magnetic resonance compatibility is doped with lanthanide pairs for upconversion fluorescence.<sup>138,139</sup>

Applications for cellular and tissue imaging as alternatives to organic dyes and QDs for luminescent probes have demonstrated success.<sup>140,141</sup> Wysokińska et al. reviewed the potential interactions of NaGdF<sub>4</sub>:Yb<sup>3+</sup>, Er<sup>3+</sup> UCNPs with murine macrophage and fibroblast cells.<sup>142</sup> They concluded the addition of a PEG coating or silica shell greatly improved the viability of cells, but also enhanced the interaction. Other groups have demonstrated the successful non-toxic interactions between 16HBE, HeLA, MCF-7, and KB cells after incubation with UCNPs.<sup>143,144</sup> *In vivo* murine models with and without tumour xenografts, UCNPs exhibited localization within the tumour and liver, demonstrating its effectiveness as a contrast agent.<sup>91,106,145</sup> Furthermore, Zhou et al. compared the NaGdF<sub>4</sub>-based UCNPs to Magnevist<sup>®</sup> (Gd ions chelated to diethylenetriaminepentaacetic acid) and found UCNPs contained a higher concentration Gd resulting in a stronger T1-weighted MRI signal.<sup>106</sup>

## 1.6 Motivation

The potential of nanoparticles to enhance biomedical applications is massive. By themselves, nanoparticles are a blank slate, capable of molding, and designing the ideal composition for specific applications. In combining imaging compatible nanoparticles coupled with a targeting ligand/antibodies and potentially in conjunction with a drug encapsulating reservoir, the ideal theranostic vehicle can be designed to provide both purpose and cellular specificity.<sup>94,146</sup> As individual components, it is understood nanoparticles possess far superior properties than can address the shortcomings of current biomedical technology. However as a whole, much is still to be investigated to

characterize cellular interactions, identify ideal synthesis and modification procedures, and compare its effectiveness to current technologies.

On the other hand, proteins and antibodies provide both specificity and function to the nanoparticle where it lacks. First pioneered in the 1960s, nanoparticles were conceptualized as a “magic bullet” to target specific disease with accuracy and specificity.<sup>29</sup> One vital proposed clinical application of nanoparticles is for the treatment of wet age-related macular degeneration (AMD), characterized by abnormal neovascularization in the choroid of the eye, prevalent in those aged 50 or older.<sup>147,148</sup> Currently several anti-vascular endothelial growth factors have been proven to be effective against neovascularization in AMD and improve visual acuity.<sup>148–150</sup> However, the effects demonstrated last several weeks, prompting repeated dosages injected into the eye to control the neovascularization. Nanoparticles have been proposed to deliver nucleic acid fragments such as oligonucleotide and neurotrophic factors to inhibit VEGF secretion and mRNA expression as alternative treatments to increase time between dosages.<sup>147</sup> Furthermore, cell adhesion molecules or receptors are required to minimize unwanted side effects.<sup>147</sup>

The nanoparticle and protein conjugation process, a molecular level understanding, is pertinent to ensure the successful incorporation of the individual components into a theranostic vehicle as a cohesive unit. A thorough analysis is required to assess the potency of the theranostic vehicle especially if intended for *in vivo* or clinical applications. The cellular level of understanding the nanoparticle and cellular protein interaction is relevant to ensure the desired outcome is achieved with minimal adverse effects.

## 1.7 Thesis Objectives

The overarching theme of this thesis is to understand effects of the interaction between nanoparticles and proteins at the molecular level (ie: synthesis and bioconjugation strategies) and at the cellular level (ie: cellular interaction) and develop novel biomedical applications in the realms of drug delivery, medical imaging, and biosensing. The specific objectives of each chapter of this thesis are introduced below.



In Chapter 2, the objective was to quantitatively assess our hybridized drug delivery model composed of a gelatin nanoparticle drug reservoir and CdSe QDs modified with a non-cell specific targeting antibody anti-human immunoglobulin G. The goal was to assess the cytotoxic effects on U20S human osteosarcoma cell derived UTA-6 cells as a proof of concept for potential drug delivery applications with fluorescent tracking. We hypothesized our model would associate on the surface of the cells to provide a stable reservoir for drug release.

In Chapter 3, the objective was to assess and compare the gelatin nanoparticles model in Chapter 2 of different sizes functionalized via different strategies and its influence on the compatibility with UTA-6 cells. We hypothesized both size and modifications order are crucial to the success of the theranostic vehicle as a whole. We identified the location of the nanoparticle model relative to the cell and contrasted the larger to the smaller nanoparticle model for effectiveness as a non-cytotoxic drug carrier.

In Chapter 4, the objective was to develop a theranostic model with bimodal tracking capabilities and anti-VEGF functionalization for anti-angiogenesis treatment. The proposed model core, NaGdF<sub>4</sub>: Er, Yb, is compatible with both magnetic resonance and fluorescent imaging. We assessed the model as a whole to inhibit angiogenesis in human umbilical vascular endothelial cells stimulated to exhibit angiogenic properties such as migration and proliferation. We hypothesized the model would provide the relevant theranostic properties suitable for *in vivo* tracking as it exerts its therapeutic effect.

In Chapter 5, the objective was to develop a safe and non-invasive biosensor for the detection of tear glucose. We proposed the use of upconversion nanoparticles for Förster Resonant Energy Transfer (FRET) as a means to detect changes in tear glucose on a contact lens-based substrate fluorometrically. Tear glucose can reflect the blood glucose concentration, albeit rather slowly. We assessed our sensor's sensitivity and compared that to a glucose meter that is commercially available. We hypothesized our glucose biosensor is non-cytotoxic and can detect low levels of tear glucose with high accuracy.

In Chapter 6, an overview and summary of the important findings and conclusions of Chapters 2-5 will be presented. The limitations of current technology will be presented

and discussed with potential solutions. The thesis ends with a roadmap for future studies that could build on the groundwork of knowledge generated by this research.

## 1.8 References

1. Vogenberg, F. R., Isaacson Barash, C. & Pursel, M. Personalized medicine: part 1: evolution and development into theranostics. *Pharm. Ther.* **35**, 560–576 (2010).
2. Xie, J., Lee, S. & Chen, X. Nanoparticle-based theranostic agents. *Adv. Drug Deliv. Rev.* **62**, 1–32 (2010).
3. Limaye, N. Pharmacogenomics, theranostics and personalized medicine - The complexities of clinical trials: Challenges in the developing world. *Appl. Transl. Genomics* **2**, 17–21 (2013).
4. Yasuda, S. U., Zhang, L. & Huang, S. M. The role of ethnicity in variability in response to drugs: focus on clinical pharmacology studies. *Clin. Pharmacol. Ther.* **84**, 417–423 (2008).
5. Pye, H. *et al.* A HER2 selective theranostic agent for surgical resection guidance and photodynamic therapy. *Photochem. Photobiol. Sci.* **5**, 341–354 (2016).
6. Weinshilboum, R. Inheritance and drug response. *N. Engl. J. Med.* **348**, 529–537 (2003).
7. Wood, A. J. J., Evans, W. E. & McLeod, H. L. Pharmacogenomics — Drug Disposition, Drug Targets, and Side Effects. *N. Engl. J. Med.* **348**, 538–549 (2003).
8. Faradan, V. K., Chen, L. & Xie, J. *Nanomedicine: Design and Applications of Magnetic Nanomaterials, Nanosensors and Nanosystems.* (Wiley, 2008).
9. Johns, C. S., Swift, A. J., Hughes, P. J. C., Schiebler, M. & Wild, J. M. Pulmonary MR angiography and perfusion imaging – a review of methods and applications. *Eur. J. Radiol.* **86**, 361–370 (2016).
10. Park, M. J., Kim, M. J., Lee, Y. J., Park, S. & Lee, W. J. Use of imaging to Predict complete response of colorectal liver Metastases after chemotherapy: MR Imaging

versus CT Imaging. **0**, 1–9 (2017).

11. Frydrychowicz, A. *et al.* Hepatobiliary MR Imaging with Gadolinium Based Contrast Agents. *J. Magn. Reson. Imaging* **35**, 492–511 (2012).
12. Knutson, S., Raja, E., Bomgarden, R., Nlend, M. & Chen, A. Development and Evaluation of a Fluorescent Antibody-Drug Conjugate for Molecular Imaging and Targeted Therapy of Pancreatic Cancer. *PLoS One* **11**, 1–25 (2016).
13. Pillai, M. R. A., Nanabala, R., Joy, A., Sasikumar, A. & Russ Knapp, F. F. Radiolabeled enzyme inhibitors and binding agents targeting PSMA: Effective theranostic tools for imaging and therapy of prostate cancer. *Nucl. Med. Biol.* **43**, 692–720 (2016).
14. Perez, E. A., Cortés, J., Gonzalez-Angulo, A. M. & Bartlett, J. M. S. HER2 testing: Current status and future directions. *Cancer Treat. Rev.* **40**, 276–284 (2014).
15. Sheikh, A., Polack, B., Rodriguez, Y. & Kuker, R. Nuclear Molecular and Theranostic Imaging for Differentiated Thyroid Cancer. *Mol. Imaging Radionucl. Ther.* **26**, 50–65 (2016).
16. Fleuren, E. D. G. *et al.* Theranostic applications of antibodies in oncology. *Mol. Oncol.* **8**, 799–812 (2014).
17. Farkouh, A., Frigo, P. & Czejka, M. Systemic side effects of eye drops : a pharmacokinetic perspective. *Clin. Ophthalmol.* **10**, 2433–2441 (2016).
18. Nebeker, J. R., Barach, P. & Samore, M. H. Improving Patient Care Clarifying Adverse Drug Events : A Clinician’s Guide to Terminology. *Ann. Intern. Med.* **140**, 795–802 (2004).
19. Goldstein, D. B. Pharmacogenetics in the laboratory and the clinic. *N. Engl. J. Med.* **348**, 553–556 (2003).
20. Shiraishi, K., Wang, Z., Kokuryo, D., Aoki, I. & Yokoyama, M. A polymeric

- micelle magnetic resonance imaging (MRI) contrast agent reveals blood–brain barrier (BBB) permeability for macromolecules in cerebral ischemia-reperfusion injury. *J. Control. Release* **253**, 165–171 (2017).
21. Lundquist, P. & Artursson, P. Oral absorption of peptides and nanoparticles across the human intestine: Opportunities, limitations and studies in human tissues. *Adv. Drug Deliv. Rev.* **106**, 256–276 (2016).
  22. Sukriti, S., Tauseef, M., Yazbeck, P. & Mehta, D. Mechanisms regulating endothelial permeability. *Pulm. Vasc. Reseach Inst.* **4**, 535–551 (2015).
  23. Natalin, R. A., Prince, M. R., Grossman, M. E., Silvers, D. & Landman, J. Contemporary applications and limitations of magnetic resonance imaging contrast materials. *J. Urol.* **183**, 27–33 (2010).
  24. Tedeschi, E. *et al.* Gadolinium retention in the body: what we know and what we can do. *Radiol. Med.* **122**, 1–12 (2017).
  25. Andreucci, M., Solomon, R. & Tasanarong, A. Side Effects of Radiographic Contrast Media : Pathogenesis , Risk Factors , and Prevention. *Biomed Res. Int.* **2014**, 1–21 (2014).
  26. Bae, K. T. Intravenous Contrast Medium Administration and Scan Timing at CT: Considerations and Approaches. *Radiology* **256**, 32–61 (2010).
  27. Carmen Alvarez-Loreno, A. C. *Smart Materials for Drug Delivery Volume 1.* (RSC Publishing, 2013).
  28. Grund, S., Bauer, M. & Fischer, D. Polymers in drug delivery-state of the art and future trends. *Adv. Eng. Mater.* **13**, 61–87 (2011).
  29. Hoffman, A. S. The origins and evolution of ‘controlled’ drug delivery systems. *J. Control. Release* **132**, 153–163 (2008).
  30. Ding, C. & Li, Z. A review of drug release mechanisms from nanocarrier systems.

- Mater. Sci. Eng. C* **76**, 1440–1453 (2017).
31. Mignani, S., El Kazzouli, S., Bousmina, M. & Majoral, J. P. Expand classical drug administration ways by emerging routes using dendrimer drug delivery systems: A concise overview. *Adv. Drug Deliv. Rev.* **65**, 1316–1330 (2013).
  32. Bruschi, M. L. *Strategies To Modify The Drug Release From Pharmaceutical Systems*. (Woodhead Publishing, 2015).
  33. Kumari, A., Yadav, S. K. & Yadav, S. C. Biodegradable polymeric nanoparticles based drug delivery systems. *Colloids Surfaces B Biointerfaces* **75**, 1–18 (2010).
  34. Heaney, R. Bioavailability of Nutrients and Other Bioactive Components from Dietary Supplements. *J. Nutr.* **131**, 1376–1382 (2001).
  35. Lee, S. H. Intestinal Permeability Regulation by Tight Junction: Implication on Inflammatory Bowel Diseases. *Intest. Res.* **13**, 11 (2015).
  36. Saltzman, W. M. *Drug Delivery: Engineering Principles for Drug Therapy*. (Oxford University Press, Inc., 2001).
  37. Nicoll, L. H. & Hesby, A. Intramuscular injection: An integrative research review and guideline for evidence-based practice. *Appl. Nurs. Res.* **15**, 149–162 (2002).
  38. Jin, J. F. *et al.* The optimal choice of medication administration route regarding intravenous, intramuscular, and subcutaneous injection. *Patient Prefer. Adherence* **9**, 923–942 (2015).
  39. Karande, P. & Mitragotri, S. Enhancement of transdermal drug delivery via synergistic action of chemicals. *Biochim. Biophys. Acta - Biomembr.* **1788**, 2362–2373 (2009).
  40. Naik, A., Kalia, Y. N. & Guy, R. H. Transdermal drug delivery: Overcoming the skin's barrier function. *Pharm. Sci. Technol. Today* **3**, 318–326 (2000).
  41. Paudel, K. S. *et al.* Challenges and opportunities in dermal/transdermal delivery.

- Ther. Deliv.* **1**, 109–131 (2010).
42. Gavhane, Y. N. & Yadav, A. V. Loss of orally administered drugs in GI tract. *Saudi Pharm. J.* **20**, 331–344 (2012).
  43. Becker, D. E. Drug therapy in dental practice: general principles. Part 2 - pharmacodynamic considerations. *Anesth. Prog.* **54**, 19-23–5 (2007).
  44. Yuan, S. Y. & Rigor, R. R. *Regulation of Endothelial Barrier Function*. (Morgan & Claypool Life Sciences, 2011).
  45. Back, D. K., Rogers, S. M. Review: first-pass metabolism by the gastrointestinal mucosa. *Aliment. Pharmacology Ther.* **1**, 339–357 (1987).
  46. Rippe, B. & Haraldsson, B. Transport of macromolecules across microvascular walls: the two-pore theory. *Physiol. Rev.* **74**, 163–219 (1994).
  47. Lehne, R. A. *Pharmacology for Nursing Care*. (Elsevier Inc., 2007).
  48. Lee, D. Y. & Li, K. C. P. Molecular Theranostics : A Primer for the Imaging Professional. *Am. J. Roentgenol.* **197**, 318–324 (2011).
  49. Brown, M. A. & Semelka, R. C. *MRI: basic principles and applications*. (Wiley-Blackwel/John Wiley & Sons, 2010).
  50. Bushong, S. C. & Clarke, G. *Magnetic resonance imaging: physical and biological principles*. (Elsevier Mosby, 2015).
  51. Levitt, M. H. *Spin dynamics: basics of nuclear magnetic resonance*. (John Wiley & Sons, 2008).
  52. Lanzman, B. & Heit, J. J. Advanced MRI Measures of Cerebral Perfusion and Their Clinical Applications. *Top. Magn. Reson. Imaging* **26**, 1 (2017).
  53. Liu, X. *et al.* Advanced Neuroimaging in the Evaluation of Spinal Cord Tumors and Tumor Mimics: Diffusion Tensor and Perfusion Weighted Imaging. *Semin.*

*Ultrasound, CT MRI* **38**, 163–175 (2016).

54. Fraum, T. J., Ludwig, D. R., Bashir, M. R. & Fowler, K. J. Gadolinium-based contrast agents: A comprehensive risk assessment. *J. Magn. Reson. Imaging* **46**, 338–353 (2017).
55. Quattrocchi, C. C. & Molen, A. J. Van Der. Gadolinium Retention in the Body and Brain : Is It Time for an International Joint. *Radiology* **282**, 12–16 (2017).
56. Hui, F. K. & Mullins, M. Persistence of Gadolinium Contrast Enhancement in CSF : A Possible Harbinger of Gadolinium Neurotoxicity? *Am. J. Neuroradiol.* **30**, 3174 (2009).
57. Maramattom, B. V, Manno, E. M., Wijdicks, E. F. & Lindell, E. P. Gadolinium encephalopathy in a patient with renal failure. *Neurology* **64**, 1276–1278 (2005).
58. Ramalho, J., Ramalho, M., Jay, M., Burke, L. M. & Semelka, R. C. Gadolinium toxicity and treatment. *Magn. Reson. Imaging* **34**, 1394–1398 (2016).
59. Orcutt, K. D. *et al.* Engineering an antibody with picomolar affinity to DOTA chelates of multiple radionuclides for pretargeted radioimmunotherapy and imaging. *Nucl. Med. Biol.* **38**, 223–233 (2011).
60. Elvas, F. *et al.* (99m)Tc-Duramycin SPECT Imaging of Early Tumor Response to Targeted Therapy: A Comparison with (18)F-FDG PET. *J. Nucl. Med.* **58**, 665–670 (2017).
61. Liu, C., Zhang, X., Song, Y., Wang, Y. & Zhang, F. SPECT and fluorescence imaging of vulnerable atherosclerotic plaque with a vascular cell adhesion molecule 1 single-chain antibody fragment. *Atherosclerosis* **254**, 263–270 (2016).
62. Laverman, P. *et al.* Immuno-PET and Immuno-SPECT of Rheumatoid Arthritis with Radiolabeled Anti-Fibroblast Activation Protein Antibody Correlates with Severity of Arthritis. *J. Nucl. Med.* **56**, 778–784 (2015).



63. Grum, D. *et al.* Design of a Modular Protein-Based MRI Contrast Agent for Targeted Application. *PLoS One* **8**, 4–11 (2013).
64. Ntziachristos, V. Fluorescence Molecular Imaging. *Annu. Rev. Biomed. Eng.* **8**, 1–33 (2006).
65. Sekar, T. V, Mohanram, R. K., Foygel, K. & Paulmurugan, R. Therapeutic Evaluation of microRNAs by Molecular Imaging. *Theranostics* **3**, (2013).
66. van Oosten, M. *et al.* Real-time in vivo imaging of invasive- and biomaterial-associated bacterial infections using fluorescently labelled vancomycin. *Nat. Commun.* **4**, 2584 (2013).
67. Ono, K., Kuwabara, Y. & Han, J. MicroRNAs and cardiovascular diseases. *FEBS J.* **278**, 1619–1633 (2011).
68. Hu, Y., Ehli, E. A. & Boomsma, D. I. MicroRNAs as Biomarkers for Psychiatric Disorders With a Focus on Autism Spectrum Disorder: Current Progress in Genetic Association Studies, Expression Profiling, and Translational Research. *Autism Res.* (2017).
69. Zhao, Y. *et al.* Critical Role of the Virus-Encoded MicroRNA-155 Ortholog in the Induction of Marek ' s Disease Lymphomas. *PLOS Pathog.* **7**, 13 (2011).
70. Chan, W. C. W. & Nie, S. Quantum Dot Bioconjugates for Ultrasensitive Nonisotopic Detection. *Science* **281**, 2016–2018 (1998).
71. Chan, W. C. W. *et al.* Luminescent quantum dots for multiplexed biological detection and imaging. *Curr. Opin. Biotechnol.* **13**, 40–46 (2002).
72. Gao, X. *et al.* In vivo molecular and cellular imaging with quantum dots. *Curr. Opin. Biotechnol.* **16**, 63–72 (2005).
73. Schulz, R. B. & Semmler, W. in *Molecular Imaging I* (ed. Wolfhard Semmler, M. S.) 3–23 (Springer-Verlag Berlin Heidelberg, 2008).

74. Ge, J. *et al.* Standard Fluorescent Imaging of Live Cells is Highly Genotoxic. *Cytometry A* **83**, 552–560 (2014).
75. Brash, D. E. *et al.* A role for sunlight in skin cancer : UV-induced p53 mutations in squamous cell carcinoma. *Proc. Natl. Acad. Sci. USA* **88**, 10124–10128 (1991).
76. Shibutani, S., Takeshita, M. & Grollman, A. P. Insertion of Specific Bases during DNA Synthesis Past the Oxidation-Damaged Base 8-OxodG. *Nature* **349**, 431–434 (1991).
77. Wood, M. L., Dizdaroglu, M., Gajewski, E. & Essigmann, J. M. Mechanistic Studies of Ionizing Radiation and Oxidative Mutagenesis : Genetic Effects of a Single 8-Hydroxyguanine ( 7-Hydro-8-oxoguanine ) Residue Inserted at a Unique Site in a Viral Genome1. *Biochemistry* **29**, 7024–7032 (1990).
78. Sattler, K. D. *Handbook of Nanophysics: Nanoparticles and Quantum Dots.* (CRC Press, 2010).
79. Kham, F. A. *Biotechnology Fundamentals.* (CRC Press, 2011).
80. Faraday, M. The Bakerian Lecture : Experimental Relations of Gold and Other Metals) to Light. *Philos. Trans. R. Soc. London* **147**, 145–181 (1857).
81. Beilby, G. T. The Effects of Heat and of Solvents on Thin Films of Metal. *Proc. R. Soc. London* **72**, 226–235 (1903).
82. Voura, E. B., Jaiswal, J. K., Mattoussi, H. & Simon, S. M. Tracking metastatic tumor cell extravasation with quantum dot nanocrystals and fluorescence emission-scanning microscopy. *Nat. Med.* **10**, 993–998 (2004).
83. Padmanabhan, P., Kumar, A., Kumar, S., Kumar, R. & Gulyás, B. Nanoparticles in practice for molecular-imaging applications : An overview. *Acta Biomater.* **41**, 1–16 (2016).
84. Gao, X., Cui, Y., Levenson, R. M., Chung, L. W. K. & Nie, S. In vivo cancer

- targeting and imaging with semiconductor quantum dots. *Nat. Biotechnol.* **22**, 969–976 (2004).
85. Liu, B., Li, C., Yang, P., Hou, Z. & Lin, J. 808-nm-Light-Excited Lanthanide-Doped Nanoparticles : Rational Design , Luminescence Control and Theranostic Applications. *Adv. Mater.* **29**, (2017).
  86. Hong, G., Antaris, A. L. & Dai, H. Near-infrared fluorophores for biomedical imaging. *Nat. Biomed. Eng.* **1**, 1–22 (2017).
  87. Zijlstra, P., Paulo, P. M. R. & Orrit, M. Optical detection of single non-absorbing molecules using the surface plasmon resonance of a gold nanorod. *Nat. Nanotechnol.* **7**, (2012).
  88. Amendola, V., Pilot, R., Frasconi, M., Maragò, O. M. & Iati, M. A. Surface plasmon resonance in gold nanoparticles : a review. *J. Phys. Condens. Matter* **29**, 1–48 (2017).
  89. Serkova, N. J. Nanoparticle-Based Magnetic Resonance Imaging on Tumor-Associated Macrophages and Inflammation. *Front. Immunol.* **8**, 1–7 (2017).
  90. Li, K., Nejadnik, H. & Daldrup-link, H. E. Next-generation superparamagnetic iron oxide nanoparticles for cancer theranostics. *Drug Discov. Today* **0**, (2017).
  91. Hou, Y. *et al.* NaGdF<sub>4</sub> Nanoparticle-Based Molecular Probes for Magnetic Resonance Imaging of Intraperitoneal Tumor Xenografts in Vivo. *ACS Nano* **7**, 330–338 (2013).
  92. Zhang, K. *et al.* Gd<sub>2</sub>O<sub>3</sub> and GH combined with red blood cells to improve the sensitivity of contrast agents for cancer targeting MR imaging. *Biomater. Sci.* **5**, 46–49 (2017).
  93. Seleci, M., Seleci, D. A., Jonczyk, R., Stahl, F. & Blume, C. Smart multifunctional nanoparticles in nanomedicine. *Bionanomaterials* **17**, 33–41 (2016).

94. Chang, E. H. *et al.* Nanomedicine: Past, present and future – A global perspective. *Biochem. Biophys. Res. Commun.* **468**, 511–517 (2015).
95. Gravit, L. Therapy: this time it's personal. *Nature* **509**, S52–S54 (2014).
96. Choi, K. Y., Liu, G., Lee, S. & Chen, X. Theranostic nanoplateforms for simultaneous cancer imaging and therapy: current approaches and future perspectives. *Nanoscale* **4**, 330–342 (2012).
97. Mahapatro, A. & Singh, D. K. Biodegradable nanoparticles are excellent vehicle for site directed in-vivo delivery of drugs and vaccines. *J. Nanobiotechnology* **9**, 55 (2011).
98. Koukaras, E. N., Papadimitriou, A., Bikiaris, D. N. & Froudakis, G. E. Insight on the Formation of Chitosan Nanoparticles through Iontropic Gelation with Tripolyphosphate. *Mol. Pharm.* **9**, 2856–2862 (2012).
99. Sachin, M., Sachin, D. & Dinesh, S. Voyage of Theranostic Liposomes for Imaging and Therapy. *J. Cosmet. Laser Ther.* **4172**, (2017).
100. Göke, K. *et al.* Novel strategies for the formulation and processing of poorly water-soluble drugs. *Eur. J. Pharm. Biopharm.* (2017).
101. Reis, C. P. & Neufeld, R. J. Nanoencapsulation I. Methods for preparation of drug-loaded polymeric nanoparticles. *Nanomedicine Nanotechnology, Biol. Med.* **2**, 8–21 (2006).
102. Ju, E., Saeed, L. & Khan, A. Studies on the characteristics of drug-loaded gelatin nanoparticles prepared by nanoprecipitation. *Bioprocess Biosyst. Eng.* **35**, 297–307 (2012).
103. Sayed, E., Ruparelia, K., Arshad, M. S., Chang, M. & Ahmad, Z. Porous Inorganic Drug Delivery Systems — a Review. *AAPS PharmSciTech* (2017). doi:10.1208/s12249-017-0740-2

104. Tarhini, M., Greige-gerges, H. & Elaissari, A. Protein-based nanoparticles : From preparation to encapsulation of active molecules. *Int. J. Pharm.* **522**, 172–197 (2017).
105. Proietti, S., Carlomagno, G., Dinicola, S. & Bizzarri, M. Soft gel capsules improve melatonin ' s bioavailability in humans Soft gel capsules improve melatonin ' s bioavailability in humans. *Expert Opin. Drug Metab. Toxicol.* **5255**, (2017).
106. Zhou, J. *et al.* Dual-modality in vivo imaging using rare-earth nanocrystals with near-infrared to near-infrared ( NIR-to-NIR ) upconversion luminescence and magnetic resonance properties. *Biomaterials* **31**, 3287–3295 (2010).
107. Jonassen, H., Kjørniksen, A. & Hiorth, M. Stability of Chitosan Nanoparticles Cross-Linked with Tripolyphosphate. *Biomacromolecules* **13**, 3747–3756 (2012).
108. Leo, E., Vandelli, M. A., Cameroni, R. & Forni, F. Doxorubicin-loaded gelatin nanoparticles stabilized by glutaraldehyde : Involvement of the drug in the cross-linking process. *Int. J. Pharm.* **155**, 75–82 (1997).
109. Vandervoort, J. & Ludwig, A. Preparation and evaluation of drug-loaded gelatin nanoparticles for topical ophthalmic use. *Biopharmaceutics* **57**, 251–261 (2004).
110. Fan, W., Yan, W., Xu, Z. & Ni, H. Formation mechanism of monodisperse , low molecular weight chitosan nanoparticles by ionic gelation technique. *Colloids Surfaces B Biointerfaces* **90**, 21–27 (2012).
111. Mohanraj, V. J. & Chen, Y. Nanoparticles – A Review. *Trop. J. Pharm. Res.* **5**, 561–573 (2006).
112. Narayanan, D. *et al.* Poly-(ethylene glycol) modified gelatin nanoparticles for sustained delivery of the anti-inflammatory drug Ibuprofen-Sodium : An in vitro and in vivo analysis. *Nanomedicine Nanotechnology, Biol. Med.* **9**, 818–828 (2013).
113. Pathak, Y. & Thassu, D. *Drug Delivery Nanoparticles Formulation and*

*Characterization*. (CRC Press, 2009).

114. Hafidz, R. M. Chemical and functional properties of bovine and porcine skin gelatin. *Int. Food Res. J.* **817**, 813–817 (2011).
115. CJ Coester, K Langer, H Von Briesen, J. K. Gelatin nanoparticles by two step desolvation - a new preparation method, surface modifications and cell uptake. *J. Microencapsul.* **17**, 187–193 (2000).
116. Zeineldin, R. *Cancer Nanotechnology*. (Springer Science+Business Media LLC, 2017).
117. Balthasar, S., Michaelis, K., Dinauer, N., Briesen, H. Von & Langer, K. Preparation and characterisation of antibody modified gelatin nanoparticles as drug carrier system for uptake in lymphocytes. *Biomaterials* **26**, 2723–2732 (2005).
118. Suk, J. S., Xu, Q., Kim, N., Hanes, J. & Ensign, L. M. PEGylation as a strategy for improving nanoparticle-based drug and gene delivery. *Adv. Drug Deliv. Rev.* **99**, 28–51 (2016).
119. Madan, J. *et al.* Long-circulating poly(ethylene glycol ) -grafted gelatin nanoparticles customized for intracellular delivery of noscapine : preparation , in-vitro characterization , structure elucidation , pharmacokinetics , and cytotoxicity analyses. *Anticancer Drugs* **22**, 543–555 (2011).
120. Chen, L., Tse, W. H., Siemiarczuk, A. & Zhang, J. Special properties of luminescent magnetic NaGdF<sub>4</sub>:Yb<sup>3+</sup>, Er<sup>3+</sup> upconversion nanocubes with surface modifications. *RSC Adv.* **7**, 26770–26775 (2017).
121. Farkhani, S. M. & Valizadeh, A. Review : three synthesis methods of CdX ( X = Se , S or Te ) quantum dots. *IET Nanobiotechnology* **8**, 59–76 (2014).
122. Petryayeva, E., Algar, W. R. & Medintz, I. L. Quantum Dots in Bioanalysis: A Review of Applications Across Various Platforms for Fluorescence Spectroscopy and Imaging. *Focal Point Rev.* **67**, 215–252 (2013).

123. Zheng, Q. & Lavis, L. D. Development of photostable fluorophores for molecular imaging. *Curr. Opin. Chem. Biol.* **39**, 32–38 (2017).
124. Song, L. Influence of the Triplet Excited State on the Photobleaching Kinetics of Fluorescein in Microscopy. *Biophys. J.* **70**, 2959–2968 (1996).
125. Widengren, J. & Rigler, R. Mechanisms of photobleaching investigated by fluorescence correlation spectroscopy. **4**, 149–157 (1996).
126. Pisanic 2nd, T. R., Zhang, Y. & Wang, T. H. Quantum dots in diagnostics and detection : principles and paradigms. *Analyst* **139**, 2968–2981 (2014).
127. Larson, D. R. *et al.* Water-Soluble Quantum Dots for Multiphoton Fluorescence Imaging in Vivo. *Science* **300**, 1434–1436 (2003).
128. Lee, C., Jang, D. & Cheong, S. Surface engineering of quantum dots for in vivo imaging. *Nanotechnology* **21**, (2010).
129. Derfus, A. M., Chan, W. C. W. & Bhatia, S. N. Probing the Cytotoxicity of Semiconductor Quantum Dots. *Nanoletters* **4**, 11–18 (2004).
130. Lakowicz, J. R. *Principles of Fluorescence Microscopy*. (Springer, 2006).
131. Guo, L., Wang, Y., Zeng, W., Zhao, L. & Han, L. Band structure and near infrared quantum cutting investigation of GdF<sub>3</sub>:Yb<sup>3+</sup>, Ln<sup>3+</sup> (Ln = Ho, Tm, Er, Pr, Tb) nanoparticles. *Phys. Chem. Chem. Phys.* **15**, 14295–14302 (2013).
132. Xu, X. *et al.* Depth-profiling of Yb<sup>3+</sup> sensitizer ions in NaYF<sub>4</sub> upconversion nanoparticles. *Nanoscale* **9**, 7719–7726 (2017).
133. Chen, G., Qiu, H., Prasad, P. N. & Chen, X. Upconversion Nanoparticles : Design , Nanochemistry , and Applications in Theranostics. *Chem. Rev.* **114**, 5161–5214 (2014).
134. Li, Z., Zhang, Y. & Jiang, S. Multicolor Core / Shell-Structured Upconversion Fluorescent Nanoparticles. *Adv. Mater.* **20**, 4765–4769 (2008).

135. Ananthaswamy, H. N. & Pierceall, W. E. Molecular Mechanisms of Ultraviolet Radiation Carcinogenesis. *Photochem. Photobiol.* **52**, 1119–1136 (1990).
136. Kwon, O. S., Song, H. S., Kim, H., Artzi, N. & Kim, J. Dual-Color Emissive Upconversion Nanocapsules for Differential Cancer Bioimaging In Vivo. (2016).
137. Su, X., Sun, X. & Wu, S. Manipulating the emission intensity and lifetime of NaYF<sub>4</sub>:Yb<sup>3+</sup>,Er<sup>3+</sup> simultaneously by embedding it into CdS photonic crystals. *Nanoscale* **9**, 7666–7673 (2017).
138. Ramasamy, P., Chandra, P., Rhee, S. W. & Kim, J. Enhanced upconversion luminescence in NaGdF<sub>4</sub>:Yb,Er nanocrystals by Fe<sup>3+</sup> doping and their application in bioimaging †. *Nanoscale* **5**, 8711–8717 (2013).
139. Holmberg, R. J., Aharen, T. & Murugesu, M. Paramagnetic Nanocrystals: Remarkable Lanthanide-Doped Nanoparticles with Varied Shape, Size, and Composition. *J. Phys. Chem. Lett.* (2012).
140. Wang, F., Deng, R. & Liu, X. Preparation of core-shell NaGdF<sub>4</sub> nanoparticles doped with luminescent lanthanide ions to be used as upconversion-based probes. *Nat. Protoc.* **9**, 1634–1644 (2014).
141. Wong, H. T. *et al.* In vitro cell imaging using multifunctional small sized KGdF<sub>4</sub>:Yb<sup>3+</sup>,Er<sup>3+</sup> upconverting nanoparticles synthesized by a one-pot solvothermal process. *Nanoscale* **5**, 3465–3473 (2013).
142. Wysokińska, E. *et al.* Cytotoxic interactions of bare and coated NaGdF<sub>4</sub>:Yb(3+):Er(3+) nanoparticles with macrophage and fibroblast cells. *Toxicol. Vitro.* **32**, 16–25 (2016).
143. Zhou, L., Zheng, X., Gu, Z., Yin, W. & Zhang, X. Biomaterials for targeted drug delivery and multimodal imaging. *Biomaterials* **35**, 7666–7678 (2014).
144. Zhang, L. *et al.* Biomaterials Inorganic photosensitizer coupled Gd-based upconversion luminescent nanocomposites for in vivo magnetic resonance imaging



- and near-infrared-responsive photodynamic therapy in cancers. *Biomaterials* **44**, 82–90 (2015).
145. Xue, Z. *et al.* Biomaterials Upconversion optical / magnetic resonance imaging-guided small tumor detection and in vivo tri-modal bioimaging based on high-performance luminescent nanorods. *Biomaterials* **115**, 90–103 (2017).
  146. Muthu, M. S., Leong, D. T., Mei, L. & Feng, S. Nanotheranostics - Application and Further Development of Nanomedicine Strategies for Advanced Theranostics. *Theranostics* **4**, 660–677 (2014).
  147. Birch, D. G. Age-related macular degeneration: a target for nanotechnology derived medicines. *Int. J. Nanomedicine* **2**, 65–77 (2007).
  148. Kovach, J. L. *et al.* Anti-VEGF Treatment Strategies for Wet AMD. *J. Ophthalmology* **2012**, 1–7 (2012).
  149. Miyamoto, N., Kojima, H. & Shimozone, M. Response of eyes with age-related macular degeneration to anti-VEGF drugs and implications for therapy planning. *Clin. Ophthalmology* **11**, 809–816 (2017).
  150. Cabral, T. *et al.* Aqueous vascular endothelial growth factor and clinical outcomes correlation after single intravitreal injection of bevacizumab in patients with neovascular age - related macular degeneration. *Int. J. Retin. Vitre.* **3**, 4–11 (2017).

## CHAPTER 2

*To quantitatively assess our hybridized drug delivery model composed of a gelatin nanoparticle drug reservoir and CdSe QDs modified with a non-cell specific targeting antibody anti-human immunoglobulin G. The goal was to assess the cytotoxic effects on U2OS human osteosarcoma cell derived UTA-6 cells as a proof of concept for potential drug delivery applications with fluorescent tracking.*

*The contents of this chapter was previously published in the Proceedings of the 14th IEEE International Conference on Nanotechnology: WH. Tse, L. Gyenis, DW. Litchfield, and J. Zhang. Engineering Large Gelatin Nanospheres Coated with Quantum Dots for Targeted Delivery to Human Osteosarcoma Cells with Enhanced Cellular Internalization. Proceedings of the 14th IEEE International Conference on Nanotechnology 2014; 672-677. doi: 10.1109/NANO.2014.6967978*

## **2 ENGINEERING LARGE GELATIN NANOSPHERES COATED WITH QUANTUM DOTS FOR TARGETED DELIVERY TO HUMAN OSTEOSARCOMA CELLS WITH ENHANCED CELLULAR INTERNALIZATION**

### **2.1 Introduction**

Larger sized nanoparticles, nanospheres (>250 nm), synthesized from different polymers such as gelatin<sup>1,2</sup> and chitosan<sup>1,3</sup> have been extensively studied as carriers for drug delivery due to their superior biocompatibility. Most studies focus on drug release profiles dependent on various sized nanocarriers.<sup>4,5</sup> To realize optimal results of cancer treatment, suitable surface modification is required to deliver drug-loaded nanospheres to a targeted area.<sup>6</sup> Gelatin nanospheres (GNs) have been used to deliver genes and different drugs in *in vitro* studies<sup>7</sup> and animal models<sup>8</sup> by modifying the surface potential to become cationic. Quite recently, efforts on using nanomaterials in theranostics have been attempted by loading fluorophores into these biopolymer nanoparticles for simultaneous cell-tracking and drug-delivery.<sup>9</sup> Theranostics, a combination of diagnostics and therapy, can be applied in three scenarios: a) pharmacogenetics; b) treatment planning; or c)

simultaneous diagnosis and therapy.<sup>10,11</sup> Properly engineered nanospheres, as a platform, have the potential for co-development into a drug carrier with bio-imaging capabilities, as described in the latter scenario.

Compared to the nature of synthetic organic dyes, quantum dots (QDs) have high fluorescence intensity, minimal photobleaching, and tunable emission peaks, i.e. the smaller the QDs the larger the associated band gap which correlates to a more blue fluorescence, and the reverse results in a more red emission.<sup>12,13</sup> Unfortunately, they can be cytotoxic; especially those synthesized from cadmium.<sup>14</sup> Modified QDs have shown improved stability,<sup>15</sup> reduced cytotoxicity,<sup>16</sup> and potentials in *in vivo* tumour targeting studies.<sup>17</sup>

Immobilization of small quantities of QDs onto biopolymer nanospheres through covalent bonds may reduce the cytotoxicity of QDs, improve photostability, and impose fluorescent properties onto biopolymer nanospheres for easy detection. Previous studies show GNs demonstrate a long circulation time and high accumulation in tumour tissues.<sup>10,18</sup> Gelatin is considered a suitable base material for QD immobilization or bioconjugation due to the various functional groups available on its surface for post synthesis modification, including hydroxyl (-OH), amino (-NH<sub>2</sub>), and carboxylic (-COOH) groups.<sup>19</sup> The varying functional groups offer many possibilities for QD-immobilization onto the surface of nanocarriers.

Furthermore, these same functional groups allow for the bioconjugation of antibodies for targeted drug delivery. However, few studies provide the quantitative analysis on the surface modification and bioconjugation of nanosized materials. In addition, it is noted that the amount of drug payload encapsulated in larger nanoparticles is easily controlled as compared to that of smaller nanoparticles. Unfortunately, it is yet quite challenging to transport nanomaterials with large diameters >150 nm into cells due to the selective and semipermeable cell membranes.<sup>20</sup> Therefore a larger sized hybridized inorganic and organic nanoparticles capable of imaging and targeted drug delivery with good cellular internalization would be the next step in the evolution of a functional theranostic molecule. The capacity of our hybrid nanospheres will be assessed on human osteosarcoma

cells, bone cancer which commonly develops during the teenage growth spurt.<sup>21</sup> Human osteosarcoma cells are normally used in biomedical studies on either targeted therapy or companion diagnostics for the treatment of this cancer.<sup>22</sup> Very few studies on using such cells for theranostic assessment have been reported yet.

## **2.2 Materials and Methods**

### **2.2.1 Study Design**

Nanosphere compatibility was assessed in human osteosarcoma U2OS cell line derived UTA-6 cells cultured in Dulbecco's Modified Eagle's medium (DMEM, Thermo) supplemented with 10% FBS, 100 units/mL penicillin and 100 µg/mL streptomycin at 37°C with 5% CO<sub>2</sub> under sterile conditions. Cells were grown until 80% confluent and then transferred into multi-well culture plates where they were kept for an additional 24 hours to ensure complete adherence to the surface of the culture dish.

The interaction of the conjugated GNs was assessed quantitatively with a plate reader and visually with a Nikon Ti Eclipse inverted microscope outfitted with an incubation chamber for live cell imaging. 2D brightfield and FITC-filtered 2D images and 3D z-stack images were collected to visualize the depth of GNs interaction with cells. The microscope was focused at 150 µm, which pertained to the height of which the surface of the cells was clearly visible.

Biocompatibility was assessed colorimetrically with a MTT cell viability Assay (Sigma-Aldrich) in triplicate incubated with 5, 10, 20, and 40 µg of GNs for 24 hours.

### **2.2.2 Gelatin Nanosphere Synthesis**

GNs were synthesized from Type A gelatin derived from porcine skin (175 Bloom, Sigma-Aldrich) using a modified two-step desolvation method (**Figure 2-1**) described by Coester et al.<sup>23</sup> 1.25 g of gelatin was dissolved in 25 mL water under constant stirring and heating at 40°C. Once dissolved, 25 mL of acetone was added as a desolvating agent. The low molecular weight gelatin contained in the supernatant of the gelatin solution centrifuged at 5000 rpm for 15 minutes was discarded. The remaining gelatin was re-

dissolved in 25 mL of deionized water acidified with hydrochloric acid (pH 2.5 - 3.0) under constant stirring and heating at 40°C. Gelatin was desolvated again by the dropwise addition of 75 mL of acetone under constant stirring and heating at 40°C. After 10 minutes of stirring, 250  $\mu$ L of a 25% glutaraldehyde solution was added to crosslink the gelatin at 40°C. The produced nanoparticles were dried at 50°C in an oven.

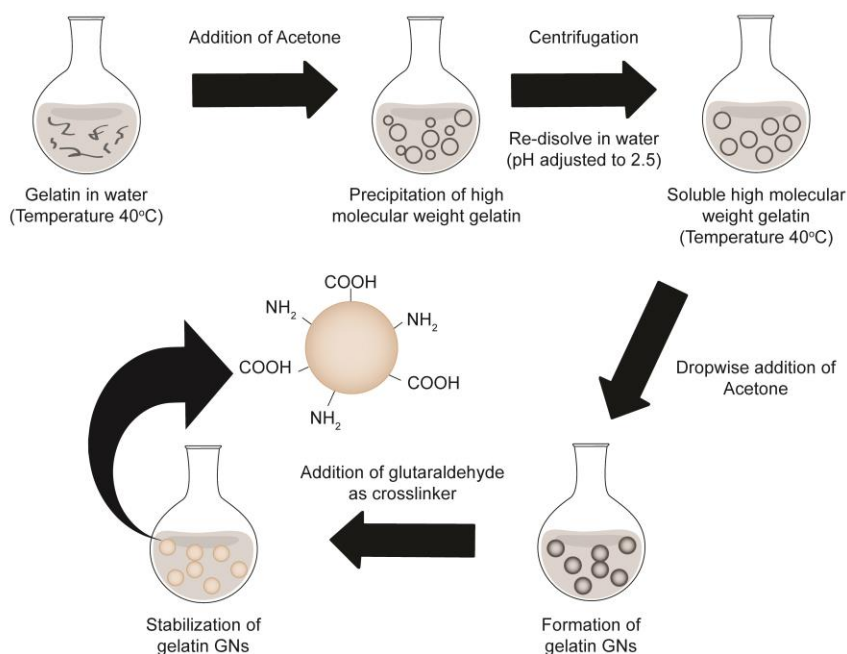


**Figure 2-1.** Two-step desolvation method of gelatin nanosphere (GNs) synthesis. Stabilization of GNs was achieved by crosslinking with glutaraldehyde.

### 2.2.3 Functionalization of CdSe/ZnS Core Shell Quantum Dots

Zinc sulfide capped cadmium selenium core-shell quantum dots (CdSe/ZnS) were synthesized from a modified method based on previous reports (**Figure 2-2**).<sup>24,25</sup> First CdSe quantum dots (QDs) were synthesized. A selenium precursor solution was prepared by dissolving 0.79 g selenium (Se) in 10 mL of trioctyl phosphine (TOP). A cadmium (Cd) solution was prepared by dissolving 0.46 g cadmium acetate dissolved in 10 mL of TOP and heated to 100°C under argon for 1 hour. The Se precursor was then injected into the Cd solution and allowed to stay at 80°C. Meanwhile, 20 g of trioctyl phosphine oxide (TOPO), 10 g of hexyldecylamine (HDA), and 5 mL of TOP was heated to 120°C under

vacuum for 2- 3 hours. This mixture was further heated to 340°C under argon protection and the CdSe solution as injected. The produced CdSe QDs were stored in hexane. Following that, a ZnS shell was applied to the CdSe QD to reduce its cytotoxic effects. 4 g of HDA, 8 g of TOPO were mixed at 180°C. 50 mg of CdSe QD dispersed in 2 mL of chloroform was added to the solution. Once the chloroform was pumped away, argon gas was introduced into reactor. A mixture of zinc acetate (54 mg), bis(trimethylsilyl)sulfide (0.05 mL) was dissolved in 1 mL each of TOP and oleylamine and injected dropwise into the QDs solution. The reaction was allowed to proceed for 1 hour at 180-185°C. CdSe/ZnS QDs were stored in hexane after centrifuging. In addition, cysteamine-functionalized CdSe/ZnS QDs were further developed to be water-soluble and capable of conjugation with GNs.<sup>26</sup> Briefly, CdSe/ZnS QDs were dispersed in a ratio of 20 mg of QDs per 3 mL of chloroform. Meanwhile, 100 mg of cysteamine hydrochloride was dissolved in 5 mL of deionized water. The solutions were combined and sonicated until the chloroform layer was clear. Free cysteamine was removed by reacting with 20 mM of 2-mercaptoethanol. The cysteamine functionalized CdSe/ZnS/QDs were collected after a threefold centrifugation and redispersed in deionized water at 8000 rpm for 10 minutes.

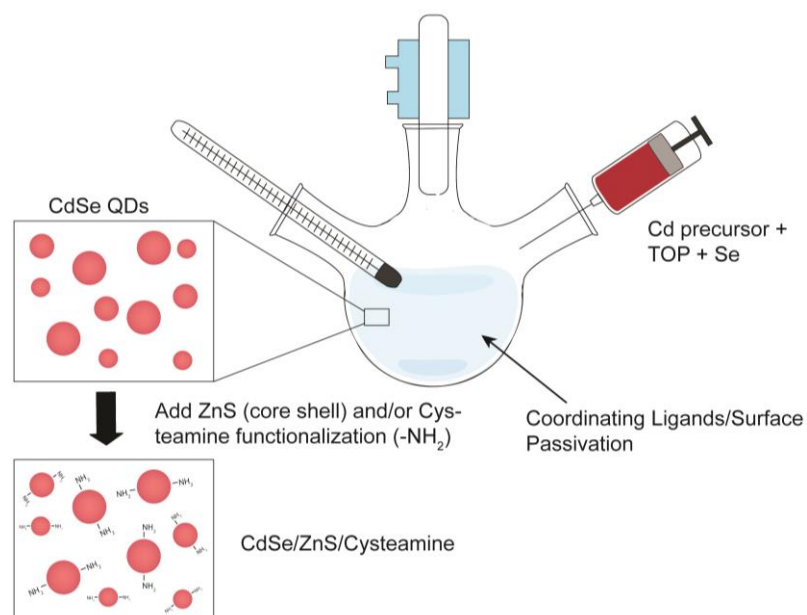


**Figure 2-2.** Synthesis scheme of CdSe/Zn/Cysteamine QDs. Organometallic synthesis of the CdSe QD core was subject to ZnS capping to form a core shell entity. Amine (-NH<sub>2</sub>) functionalization to render the QDs water-soluble and biocompatible was achieved through a thiol-exchange reaction with cysteamine hydrochloride.

## 2.2.4 Bioconjugation of GNs with anti-human Immunoglobulin G Fab

GNs were conjugated with anti-human immunoglobulin G (anti-IgG) Fab purchased from Sigma, Aldrich. The anti-IgG Fab contains the antigen binding site. 5 mg of GNs in 1 mL borate buffer (pKa of 9.14 at 25°C) mixed with 20  $\mu$ L of fluorescence FITC-tagged anti-IgG Fab solution and stock anti-human IgG Fab (4 mg/mL), respectively. The sample was agitated gently for 2 hours. Conjugated GNs were collected through a 0.5 mL 100 kDa cut-off centrifugal filter with deionized water. GNs modified with FITC-anti IgG Fab were used in comparison to GNs modified with anti-IgG Fab and QDs as shown in **Figure 2-3**.

## 2.2.5 QDs incorporating with GNs

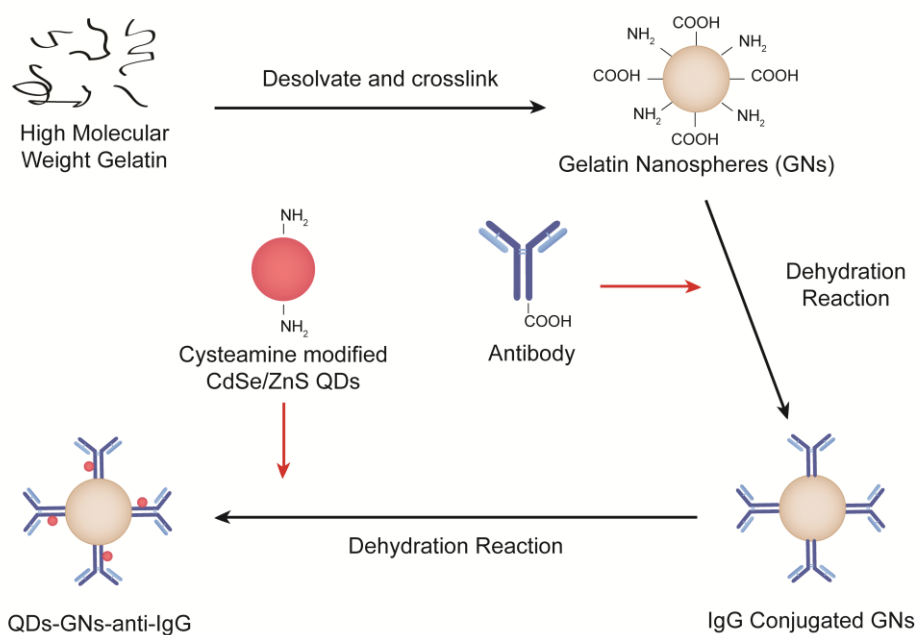


**Figure 2-3.** Functionalization scheme of Gelatin Nanospheres. Exploitation of the functional groups present on GN surface allows for the hybridization of QDs and bioconjugation of anti-IgG through a series of dehydration reactions.

In 1 mL of borate buffer, approximately 5mg of GNs with and without conjugation of anti-IgG Fab mixed with 13  $\mu$ L of a 3.75 mg/mL solution of cysteamine modified CdSe/ZnS QDs following gentle agitation for 2 hours (**Figure 2-3**). GNs with and

without antibody-conjugation were further tagged by cysteamine modified CdSe/ZnS QDs. Samples were collected after a threefold centrifugation through a 10 kDa cut-off centrifugal filter and re-dispersed with deionized water. Centrifugation occurred at 7000 rpm for 10 minutes.

### 2.2.6 Materials Characterization

Materials microstructure were investigated by a Philips CM-10 transmission electron microscope (TEM) operating at 100 kv and a high resolution TEM (JEOL 2010 F, operating at 200 kv). The diameter of the nanospheres were analyzed with ImageJ software (National Institutes of Health, USA) with an ANOVA and Kruskal-Wallis ( $p < 0.0001$ ). The Zeta ( $\zeta$ ) potential of the GNs was measured by Malvern Zetasizer 3000HSA, and calculated as the mean of 5 individual measurements. In addition, the photoluminescence (PL) of fluorescent nanomaterials was investigated by a QuantaMaster™ 40 Spectrofluorometer (Photon Technology International Inc).

### 2.2.7 Conjugation Efficiency

#### *Quantification of anti-IgG Fab Conjugated to GNs*

The amount of FITC-anti-IgG Fab conjugated to the 5 mg of GNs was determined by measuring the absorbance at 280 nm ( $A_{280\text{nm}}$ ) with a UV/Vis spectrophotometer (Agilent Technologies Cary 60) in triplicate. The protein concentration (M) of FITC-anti-IgG Fab was measured using the formula provided by ThermoScientific.

#### **Equation 2-1**

$$\text{Protein Concentration (M)} = \frac{[A_{280} - (A_{\text{max}} \times CF)]}{\epsilon} \times \text{dilution factor}$$

Where  $A_{\text{max}}$  is the absorbance (A) of a dye solution measured at the wavelength maximum ( $\lambda_{\text{max}}$ ) for the dye molecule. The correction factor (CF) of 0.36 was obtained from the manufacturer of the FITC-anti-IgG Fab protein. The molar extinction coefficient of the anti-IgG Fab ( $\epsilon$ ) was taken to be approximately 210,000 M<sup>-1</sup> cm<sup>-1</sup>.



In the situation of the non-fluorescent anti-IgG Fab, the concentration of the non-conjugated anti-IgG Fab collected from the filtrate was determined colorimetrically by a Thermo Scientific Micro BCA Protein Assay Kit relative to a standard curve (**Figure 2-4**) generated from the anti-IgG stock solution (4 mg/mL). In short, the bicinchoninic acid was reduced by specific amino acids in an alkaline environment to form a water-soluble product of which its absorbance was measured at 560 nm.

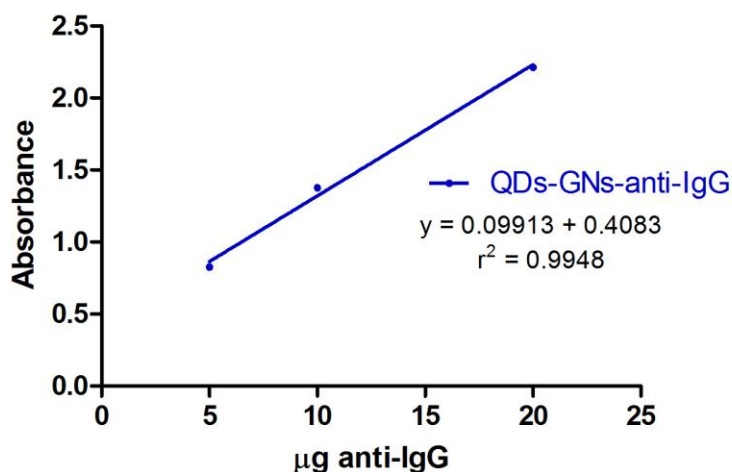


**Figure 2-4.** Protein standard curve of anti-IgG Fab. Standard curve was used to determine the amount of unbound anti-IgG from the bioconjugation with GNs using a BCA assay kit.

#### *Ratio of QD to GNs with and without antibody conjugation*

Both UV absorbance intensity and fluorescence emission intensity ( $\lambda_{\text{ex}}$ : 490nm) of produced QDs were measured as a function of the amount of modified QDs-GNs, respectively. The amount of QDs tagged onto the GNs with and without antibody bioconjugation were estimated based on the standard curves (**Figure 2-5**).

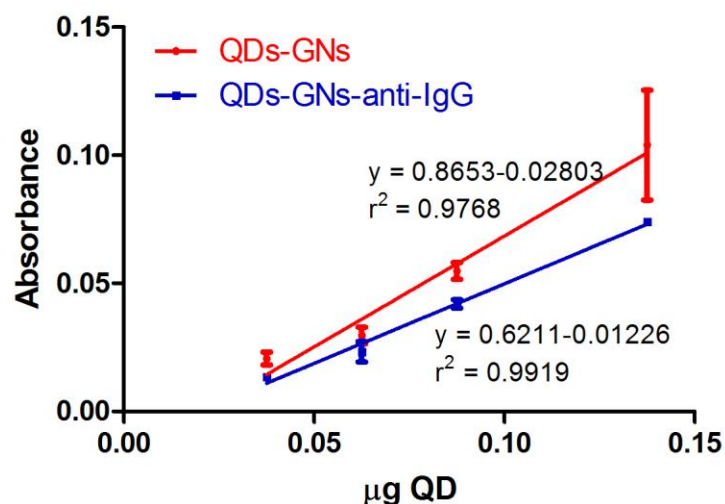


**Figure 2-5.** Standard curve of CdSe/ZnS/Cys QDs absorbance. The absorbance of the QDs-GNs was measured to determine the amount of QDs hybridized.

## 2.2.8 Cell Viability

24-hour cell viability of the functionalized GNs was assessed. Approximately 50,000 cells were seeded into each well of a 24 well plate and cultivated overnight at 37°C. UTA-6 cells were incubated with 5, 10, 20, and 40 µg of samples for 24 hours at 37°C in triplicate. The cell media was aspirated and rinsed twice with sterile PBS to remove free nanoparticles. Each well was incubated with 200 µL of growth media and 50 µL of sterile 0.5% MTT solution (0.5 mg MTT formazan powder/mL of deionized water) for 4 hours. The media was aspirated and wells were twice rinsed with sterile PBS. 150 µL of DMSO was added to each well to lyse the cells and to dissolve the tetrazolium salt. The absorbance of the plates was measured at 490 nm.

## 2.2.9 Statistical Analysis

In order to determine the statistical significance in size as a result of hybridization and bioconjugation with anti-IgG, we performed a One-Way analysis of variance (ANOVA) using GraphPad Prism (GraphPad Software Inc, La Jolla, CA, USA). Bioconjugation with FITC-anti-IgG and anti-IgG was assessed with a Mann Whitney t-test to indicate no significant difference in the bioconjugation amount. Furthermore, we compared the

increase in cellular interaction between GNs-anti-IgG-FITC and QDs-GNs-anti-IgG with a t-test relative to the GNs-QDs signal. Cell viability was assessed with a Two-Way ANOVA to study the impact as a result of modification and concentration. All statistical analyses were assessed at the 95% confidence level.

## 2.3 Results

GNs with and without functionalization were characterized by using transmission electron microscope (TEM, **Figure 2-6A**). The average particle size of bare GNs is estimated at  $270 \pm 50$  nm; whereas the average size of the hybrid fluorescent GNs conjugated with antibodies significantly increases up to  $480 \pm 50$  nm. Moreover, high crystallized CdSe/ZnS QDS ( $5 \pm 2$  nm) sporadically surrounding the surface of the GNs was identified by the high resolution TEM (**Figure 2-6B**).

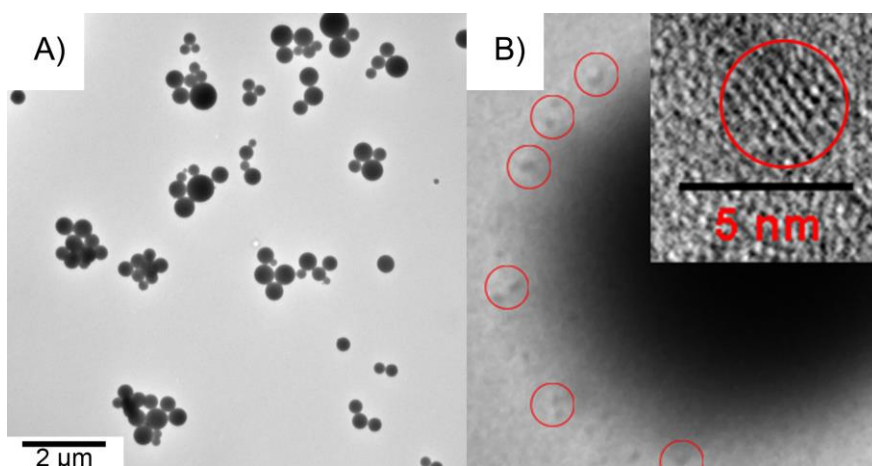


**Figure 2-6.** TEM micrographs of 175 bloom GNs. A) GNs without modifications were determined to be  $270 \pm 50$  nm. B) Hybrid GNs (i.e. QDs-GN-anti-IgG) were estimated to be  $480 \pm 50$  nm in diameter. The QDs, as indicated by the red outlines, were visualized with TEM. A high-resolution inset of the CdSe/ZnS hybridized QDs is included.

To quantitatively study the bioconjugation of the hybrid GNs, we produced GNs with the conjugation of FITC labelled anti-IgG Fab (GN-anti-IgG-FITC) using the same method. The amount of FITC-labelled anti-IgG Fab bioconjugating onto GNs was determined by comparing with the standard curve of the fluorescence emission intensity of FITC as a function of the amount of FITC. Meanwhile, free anti-IgG Fab protein which are not conjugated to the GNs were quantitatively measured by a colorimetric assay with a

Thermo Scientific Micro BCA Protein Assay Kit. Taking the molecular weight of the antibody fragment to be 50 kDa (50,000 g/mol), it was estimated that  $12.773 \pm 0.695 \mu\text{g}$  of anti-IgG Fab has been conjugated onto 1 mg of FITC tagged GNs (**Table 2-1**). Analysis indicated no significant difference ( $p = 0.2000$ ) in the amount of anti-IgG with and without FITC-tagging bioconjugated onto GNs. It suggests the bioconjugation of anti-IgG onto GNs is successful. **Table 2-1** also shows the calculated amount of anti-IgG Fab conjugated to the QDs tagged GNs (1mg) is  $12.167 \pm 0.216 \mu\text{g}$ .

In addition, the amount of QDs hybridized onto the GNs with/without anti-IgG Fab was also estimated by comparing the standard curves. It is estimated that  $0.0404 \pm 0.003 \mu\text{g}$  and  $0.0432 \pm 0.005 \mu\text{g}$  of QDs are covalently bound onto the surface of 1 mg of GNs with/without anti-IgG Fab, respectively (**Table 2-1**).

**Table 2-1.** Hybridization and conjugation quantification

<b>Hybrid</b>	<b>Amount of anti-IgG Fab (<math>\mu\text{g}</math>) conjugated on GNs (1 mg)</b>	<b>Amount of QDs (<math>\mu\text{g}</math>) tagged on GNs (1 mg)</b>
QDs-GN	----	$0.0432 \pm 0.005$
GN-anti-IgG-FITC	$12.733 \pm 0.0491$	----
QDs-GN-anti-IgG	$12.167 \pm 0.216$	$0.0404 \pm 0.003$

\*Significance of difference ( $p = 0.2000$ ) determined by one-way analysis of variance.

Bioconjugation of FITC-tagged anti-IgG on to GNs (GN-anti-IgG-FITC) was used as a reference for the QDs-GN-anti-IgG model to ensure the hybridization of QDs did not affect the anti-IgG bioconjugation.

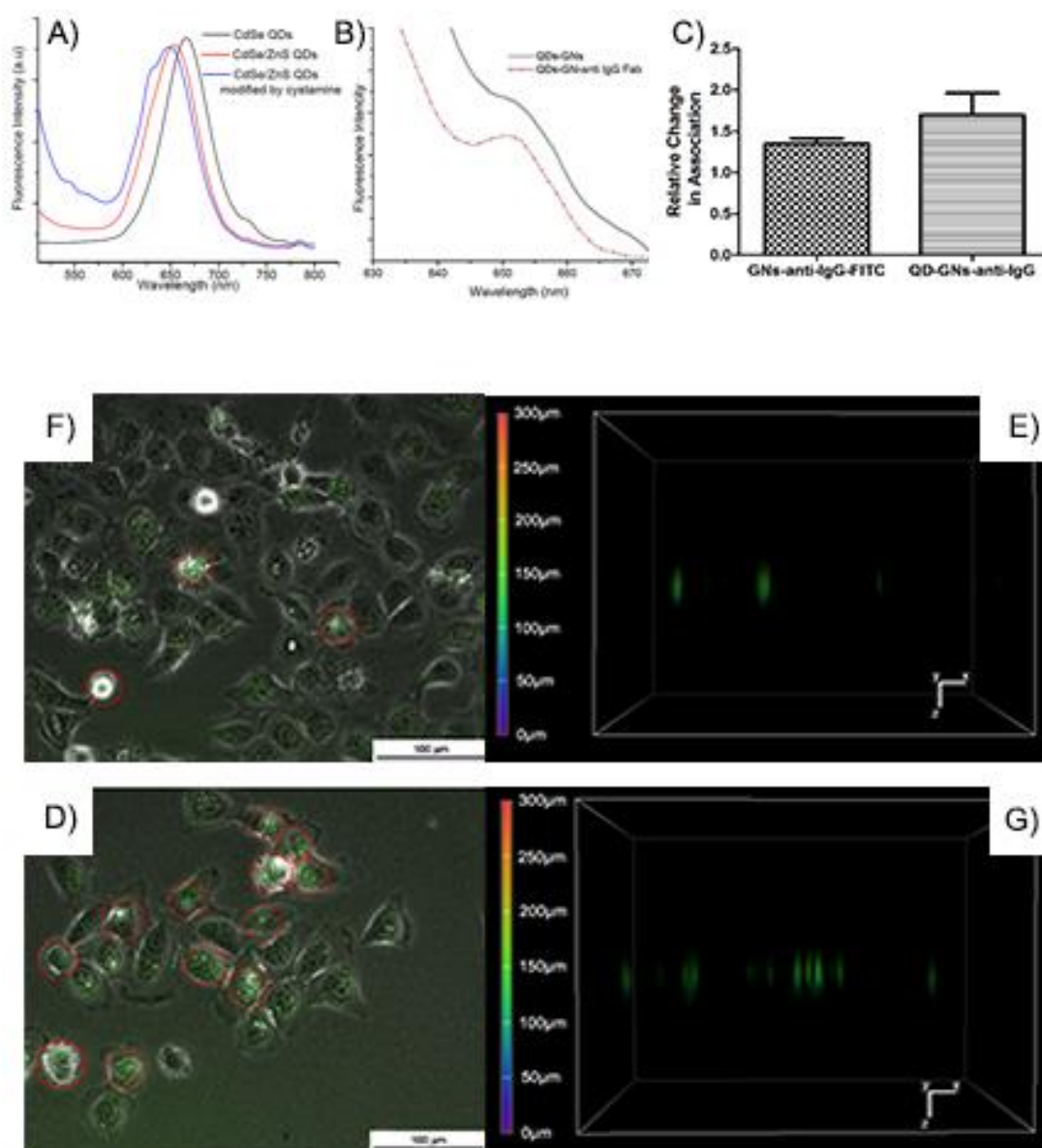


**Figure 2-7.** Determination of the interaction between functionalized GNs and UTA-6 cells. A) Photoluminescence spectra of modified QDs. B) Photoluminescence spectra of the QDs-GNs and QDs-GNs-anti-IgG (Fab) interaction. C) Relative interaction of GNs-anti-IgG-FITC (Fab) and QDs-GNs- anti-IgG (Fab) normalized to QDs-GNs. D) Fluorescent image of cells treated with QDs-GNs. E) 3D z-stack of internalized QDs-GNs. F) Fluorescent image of cells treated with QDs-GNs-anti-IgG. G) 3D z-stack of internalized QDs-GNs-anti-IgG.

\*location of the nanospheres are outlined in red.

**Figure 2-7A** shows the emission wavelength ( $\lambda_{em}$ ) of CdSe QDs centered at 667 nm measured by a QuantaMaster™ 40 Spectrofluorometer. The 13 nm blue shift of the  $\lambda_{em}$  is observed by the CdSe/ZnS QDs ( $\lambda_{em} = 654$  nm). Furthermore, there is no observed shift in fluorescent emission between QDs-GNs and QDs-GN-anti- IgG Fab (**Figure 2-7B**). It further indicates that the conjugations between antibody to GN and QDs to GN are independent due to the two different functional groups (-OH and -COOH) on a single GN.

On the other hand, the interaction of the conjugated hybrid GNs and UTA-6 cells was assessed visually with a Nikon Ti Eclipse inverted microscope outfitted with an incubation chamber for live cell imaging. A fluorescence spectrometry affiliated with the microscope was applied to quantitatively study the interaction. The GNs conjugated with anti-IgG Fab associate significantly more with the cells than those without ( $p = 0.0023$ ). When normalized against QDs-GNs, the hybrid GNs conjugated with antibody fragments and QDs exhibit insignificant difference in interaction that their fluorescent tagged counterpart (**Figure 2-7C**) when statistically assessed ( $p=0.3770$ ). This result further confirms with our quantitative analysis of the amount of antibody fragment conjugated on GNs.

The 2D images of the hybridized QDs-GNs (**Figure 2-7D**) and antibody fragment-bioconjugated QDs-GNs (**Figure 2-7F**) indicate the interaction between cells and GNs with and without antibody conjugation. Upon closer examination, we obtain more details through 3D z-stacking images on hybrid GNs associated on the cell surface (GNs-QDs, **Figure 2-7E**) and cellular internalization (QDs-GNs-anti-IgG, **Figure 2-7G**). The majority of the fluorescence signals originating below the 150  $\mu\text{m}$  mark, suggests nanosphere internalization. The statistical analysis shows the anti-IgG Fab bioconjugated QDs-GNs is able to gain 50% higher in cellular uptake and internalization by UTA-6 osteosarcoma cells than its nonbioconjugated counterpart.

The relative cell (UTA-6 cell line) viability after incubation for 24 hours with various amounts (5, 10, 20, and 40  $\mu\text{g}$ ) of nanospheres decreased with increasing nanosphere amount. In **Figure 2-8**, cell viability decreases with increasing nanosphere concentration.

The relative cell viability remained at or above 80% even when incubated with 40  $\mu\text{g}$  of nanospheres. A two-way ANOVA indicated no significant difference ( $p=0.8074$ ) in cell viability between the different samples as result of concentration changes.

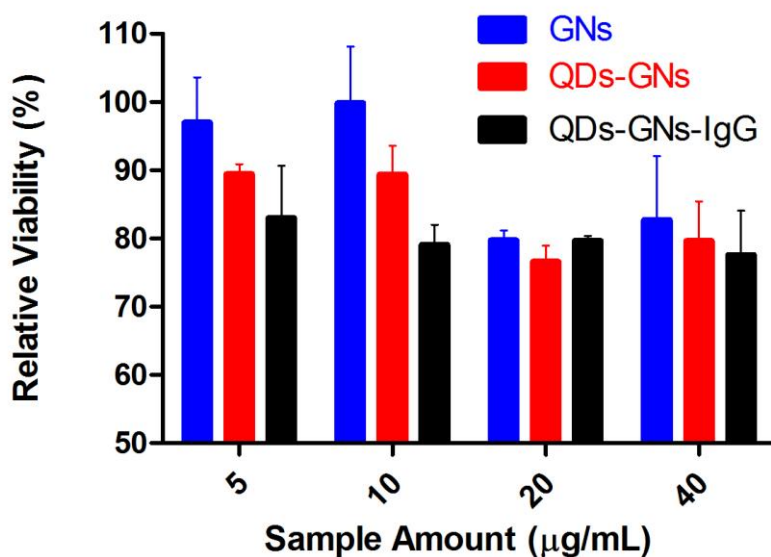


**Figure 2-8.** Relative viability of osteosarcoma cells incubated with various concentrations of functionalized GNs for 24 hours. Viability was assessed in triplicate.

## 2.4 Discussion

Our GNs model provides insight into the impact of modifications on the potential for GNs to be utilized in a theranostic fashion for *in vivo* fluorescent imaging and enhanced cellular interaction for prospective therapeutic delivery.

Several groups have already studied the *in vitro* or *in vivo* release profile of drug-encapsulated in GNs and demonstrated sustained release. Our group and that of Arbab et al. demonstrated Fickian diffusion, where drug diffusion and polymer morphology can control the overall rate of drug release, for *in vitro* applications of GNs with sustained release of protein for up to 7 days.<sup>27,28</sup> *In vivo* applications demonstrate a non-Fickian sustained release profile of up to 24 hours as a result of degradation and erosion in a biological environment.<sup>29,30</sup>

Applications of GNs for therapeutic applications require targeted selectivity to ensure accurate delivery to the site of interest to release its therapeutic payload. Covalent bonding is optimal to ensure the protein target or antibody of choice is “superglued” to the GN surface. With the  $\zeta$  potential of GNs is measured at  $24.1 \pm 0.4$  mV, i.e. uncharged surface. In the other words, both functional groups, i.e. (-COOH) and (-NH<sub>2</sub>), are available on the surface of GNs for post synthesis modifications.

Our modification analysis suggests the QDs covalently bind into the GNs through the reaction between the amine groups of cysteamine modified on the QDs and the carboxylic groups on the exterior of the GNs (**Table 1**). Due to the covalent bonding, the hybridization performed post nanoparticle synthesis will not affect the drug loading process nor contribute to the release of QDs as seen in the method described by Chen et al.<sup>31</sup> In addition, the intra-particle space for drug encapsulation would be retained with the hybridization method, which could be suitable for the nanoprecipitation method. For instance, Narayanan et al.<sup>32</sup> load the anti-inflammatory drug Ibuprofen-sodium successfully with an entrapment efficiency of ~70%.

The insignificant difference in the quantity of QDs on GNs with/without the bioconjugation of anti-IgG Fab suggest the QDs were hybridized in a stable manner onto the GNs. In addition, the quantitative analysis suggests neither surface modification procedures interfere with the other, indicating the molecules reacted non-competitively with the functional groups on the GNs surface. As such, a one-pot reaction to both hybridization and bioconjugation of the GNs is possible (**Figure 2-3**).

The fluorescent component of the QDs is detrimental to the detection of the GNs. We observed an obvious blue shift of the cysteamine modified CdSe/ZnS QDs ( $\lambda_{em}$  = 647 nm) as shown in **Figure 2-7A,B**, which could be caused by the positively charged surface of the cysteamine modified QDs.<sup>33</sup> It may result from the band-to-band recombination in the nanocrystal core.<sup>13</sup> After conjugating the modified CdSe/ZnS QDs onto the GNs through covalent bond, the  $\lambda_{em}$  of the hybrid fluorescent nanospheres is around 652 nm, similar to the emission of CdSe/ZnS QDs. As shown in **Figure 2-7** through live cell imaging (**D, F**) and z-stack imaging (**E, G**), we were successful in localizing the GNs



with respect to the cell. We observed an increase in cell surface interaction and internalization as a direct result of the anti-IgG conjugation (**Figure 2-7C**).

Our *in vivo* investigation of the GNs' interaction with osteosarcoma cells demonstrated potential for targeted therapeutic delivery. It is noted the relative cell viability of human fibroblasts treated with 10  $\mu\text{g/mL}$  bare GNs is about 100% viability in comparison to our observed  $\sim 80\%$  at 40  $\mu\text{g/mL}$  (**Figure 2-8**). The difference in cell viability could be attributed to the size distribution of our model and the functional groups involved in the modification processes. Gupta et al. demonstrated their GNs ( $37 \pm 0.84$  nm) produced via microemulsion affected cellular proliferation/viability.<sup>6</sup> Through immunostaining, it was determined phagocytosed nanoparticles caused vacuole formation within the cell body resulting in a disrupted cytoskeleton. The F-actin was organized in an anisotropic fashion with poorly developed filament bundles. Tubulin was observed to be disrupted and dispersed. Together, these disruptions inhibited cytokinesis. From our observed internalization, we concluded the size of our nanoparticle in the same sense disrupted the organization of these important fibres by filling much of the cell area thus compromising cytokinesis. The cellular membrane was observed to remain intact in our case.

Another cause of our relatively decreased viability of hybrid GNs could be attributed to cell cycle arrest caused by amino-modified QDs. As shown by Kim et al.,<sup>34</sup> the amino-modified polystyrene nanoparticles interfered with the cell cycle as cell numbers did not increase over longer incubation times. They observed the accumulation of cells between the transition points G1/S and G2/M phases of mitosis. It was unlikely the amino-modified QDs hybridized onto GNs arrested mitosis simply due to the amino groups, though it may have contributed. The size of our nanoparticle would likely have been the factor in inhibiting cytokinesis.

## 2.5 References

1. Leong, K. W., Mao, H., Roy, K., Walsh, S. M. & August, J. T. DNA-polycation nanospheres as non-viral gene delivery vehicles. *J. Control. Release* **53**, 183–193 (1998).
2. Ding, D. *et al.* Implantable Hydrogel as a Trans-Tissue Drug Delivery System. *ACS Nano* 2520–2534 (2011).
3. Tan, L., Wan, A., Li, H. & Lu, Q. Novel quantum dots – carboxymethyl chitosan nanocomposite nitric oxide donors capable of detecting release of nitric oxide in situ. *Acta Biomater.* **8**, 3744–3753 (2012).
4. Li, P. *et al.* Targeting study of gelatin adsorbed clodronate in reticuloendothelial system and its potential application in immune thrombocytopenic purpura of rat model. *J. Control. Release* **114**, 202–208 (2006).
5. Ju, E., Saeed, L. & Khan, A. Studies on the characteristics of drug-loaded gelatin nanoparticles prepared by nanoprecipitation. *Bioprocess Biosyst. Eng.* **35**, 297–307 (2012).
6. Gupta, A. K., Gupta, M., Yarwood, S. J. & Curtis, A. S. G. Effect of cellular uptake of gelatin nanoparticles on adhesion, morphology and cytoskeleton organisation of human fibroblasts. *J. Control. Release* **95**, 197–207 (2004).
7. Azarmi, S., Huang, Y. & Chen, H. Optimization of a two-step desolvation method for preparing gelatin nanoparticles and cell uptake studies in 143B osteosarcoma cancer cells. *J. Pharm. Pharm. Sciences* **9**, 124–132 (2006).
8. Kaul, G. & Amiji, M. Biodistribution and targeting potential of poly(ethylene glycol)-modified gelatin nanoparticles in subcutaneous murine tumor model. *J. Drug Target.* **12**, 585–591 (2005).
9. Jiang, S., Eltoukhy, A. A., Love, K. T., Langer, R. & Anderson, D. G. Lipidoid-Coated Iron Oxide Nanoparticles for Efficient DNA and siRNA delivery.

- Nanoletters* **13**, 1059–1064 (2013).
10. Choi, K. Y., Liu, G., Lee, S. & Chen, X. Theranostic nanoplatfoms for simultaneous cancer imaging and therapy: current approaches and future perspectives. *Nanoscale* **4**, 330–342 (2012).
  11. Chan, W. C. W. & Nie, S. Quantum Dot Bioconjugates for Ultrasensitive Nonisotopic Detection. *Science* **281**, 2016–2018 (1998).
  12. Resch-genger, U., Grabolle, M., Cavaliere-jaricot, S., Nitschke, R. & Nann, T. Quantum dots versus organic dyes as fluorescent labels. *Nat. Methods* **5**, 763–775 (2008).
  13. Gao, X. *et al.* In vivo molecular and cellular imaging with quantum dots. *Curr. Opin. Biotechnol.* **16**, 63–72 (2005).
  14. Jaiswal, J. K., Goldman, E. R., Mattoussi, H. & Simon, S. M. Use of quantum dots for live cell imaging. *Nat. Methods* **1**, 73–78 (2004).
  15. Larson, D. R. *et al.* Water-Soluble Quantum Dots for Multiphoton Fluorescence Imaging in Vivo. *Science* **300**, 1434–1436 (2003).
  16. Derfus, A. M., Chan, W. C. W. & Bhatia, S. N. Probing the Cytotoxicity of Semiconductor Quantum Dots. *Nanoletters* **4**, 11–18 (2004).
  17. Wong, C. *et al.* Multistage nanoparticle delivery system for deep penetration into tumor tissue. *PNAS* **108**, (2011).
  18. Hafidz, R. M. Chemical and functional properties of bovine and porcine skin gelatin. *Int. Food Res. J.* **817**, 813–817 (2011).
  19. Nobs, L., Buchegger, F., Gurny, R. & Alle, E. Biodegradable Nanoparticles for Direct or Two-Step Tumor Immunotargeting. *Bioconjug. Chem.* **17**, 139–145 (2006).
  20. Wang, Z., Tiruppathi, C., Cho, J., Minshall, R. D. & Malik, A. B. Critical Review

Delivery of Nanoparticle-complexed Drugs across the Vascular Endothelial Barrier via Caveolae. *IUBMB Life* **63**, 659–667 (2011).

21. Rodan, S. B. *et al.* Characterization of a Human Osteosarcoma Cell Line ( Saos-2 ) with Osteoblastic Properties. *Cancer Res.* 4961–4966 (1987).
22. Englert, C. *et al.* WT1 suppresses synthesis of the epidermal growth factor receptor and induces apoptosis. *EMBO J.* **14**, 4662–4675 (1995).
23. Coester, C. J., Langer, K., van Briesen, H. & Kreuter, J. Gelatin nanoparticles by two step desolvation - a new preparation method, surface modifications and cell uptake. *J. Microencapsul.* **17**, 187–193 (2000).
24. Talapin, D. V *et al.* CdSe / CdS / ZnS and CdSe / ZnSe / ZnS Core - Shell - Shell Nanocrystals. *J. Phys. Chem. B* 18826–18831 (2004).
25. Kortan, A. R. *et al.* Nucleation and Growth of CdSe on ZnS Quantum Crystallite Seeds , and Vice Versa , in Inverse Micelle Media. *J. Am. Chem. Soc.* 1327–1332 (1990).
26. Lee, C., Jang, D. & Cheong, S. Surface engineering of quantum dots for in vivo imaging. *Nanotechnology* **21**, (2010).
27. Azimi, B., Nourpanah, P., Rabiee, M. & Arbab, S. Producing Gelatin Nanoparticles as Delivery System for Bovine Serum Albumin. *Iran. Biomed. J.* **18**, 34–40 (2014).
28. Zhang, J., Bi, R., Hodge, W., Yin, P. & Tse, W. H. A nanocomposite contact lens for the delivery of hydrophilic protein drugs. *J. Mater. Chem. B* **1**, 4388–4395 (2013).
29. Suarasan, S. *et al.* Doxorubicin-Incorporated Nanotherapeutic Delivery System Based on Gelatin-Coated Gold Nanoparticles : Formulation , Drug Release , and Multimodal Imaging of Cellular Internalization. *Appl. Mater. Interfaces* **8**, 22900–22913 (2016).

30. Mahor, A. *et al.* Journal of Colloid and Interface Science Moxifloxacin loaded gelatin nanoparticles for ocular delivery : Formulation and in - vitro , in - vivo evaluation. *J. Colloid Interface Sci.* **483**, 132–138 (2016).
31. Chen, L., Willoughby, A. & Zhang, J. Luminescent gelatin nanospheres by encapsulating CdSe quantum dots. *Luminescence* **29**, 74–78 (2014).
32. Narayanan, D. *et al.* Poly-(ethylene glycol) modified gelatin nanoparticles for sustained delivery of the anti-inflammatory drug Ibuprofen-Sodium : An in vitro and in vivo analysis. *Nanomedicine Nanotechnology, Biol. Med.* **9**, 818–828 (2013).
33. Komarala, V. K., Rakovich, Y. P. & Bradley, A. L. Emission properties of colloidal quantum dots on polyelectrolyte multilayers. *Nanotechnology* **17**, 4117–4122 (2006).
34. Kim, J. A. *et al.* Low Dose of Amino-Modified Nanoparticles Induces Cell Cycle Arrest. *ACS Nano* **7**, 7483–7494 (2013).

## CHAPTER 3

*To quantitatively assess the effects of modification strategies of our hybridized drug delivery model composed of a gelatin nanoparticle drug reservoir and CdSe QDs modified with a non-cell specific targeting antibody anti-human immunoglobulin G (IgG). The goal was to assess the cytotoxic effects on U2OS human osteosarcoma cell derived UTA-6 cells as a direct result of modification order: i) QDs first followed by IgG; or ii) IgG first followed by QDs.*

*The contents of this chapter were previously published in the Journal of Biomaterials Applications: WH. Tse, L. Gyenis, DW. Litchfield, and J. Zhang. Cellular interaction influenced by surface modification strategies of gelatin-based nanoparticles. Journal of Biomaterials Applications. 2017: 31(7); 1087- 1096. doi: 10.1177/0885328216684651*

### **3 CELLULAR INTERACTION INFLUENCED BY SURFACE MODIFICATION STRATEGIES OF GELATIN-BASED NANOPARTICLES**

#### **3.1 Introduction**

Therapeutic advantages of using gelatin as a drug carrier include biodegradability, biocompatibility, and low toxicity due from its animal origin.<sup>1,2</sup> In its denatured form, gelatin has a long history in the clinical setting as a stabilizer in protein formulations and vaccines.<sup>3</sup> The gelatin backbone contains amino acid sequences such as Arg-Gly-Asp that can influence cell adhesion, which are not found in polymers.<sup>3</sup> Furthermore, from an engineering standpoint, gelatin's low cost and the presence of functional groups (–NH<sub>2</sub> and –COOH) allow for easy crosslinking to add stability and chemical modifications in its nanoparticle form.<sup>4</sup> Efforts to develop gelatin as a theranostic agent for concurrent application in diagnostics and therapeutics, have proved successful in *in vitro* and animal models.<sup>5,6</sup> In the past, attempts have been made by loading fluorophores or synthetic dyes into nanoparticles for simultaneous cell-tracking and drug-delivery.<sup>7-9</sup> However, due to photobleaching, alternatives such as semiconductor quantum dots (QDs) are required.<sup>8,10</sup>

QDs with a diameter in the range of tens of nm exhibit quantum confinement properties resulting in fluorescence under optical stimulation. Its emission peak is narrower than that of conventional dyes and can be tuned to emit at different frequencies depending on the particle's diameter.<sup>11</sup> Generally, these particles are thermally decomposed grown from heavy metals that are highly toxic.<sup>12</sup> Encapsulation methods have been developed to minimize toxicity and enhance its optical properties.<sup>13,14</sup> Cadmium-based QDs were one of the first types to be made and used in biological and biomedical research. Advancements in this area have led to the incorporation into drug delivery vehicles for optical confirmation. The results show promise for inclusion into a candidate model for targeted drug delivery.

One aspect of functionalization for targeted drug delivery is to reduce the therapeutic load through localized delivery. The premise is particles-modified with ligands and other cell-specific entities will circulate and associate directly with the tissue of choice and exert its therapeutic effects locally.<sup>15</sup> Compared to more traditional drug-delivery methods of intravenous infusions, injections, and oral capsules, the nanocarriers carry a smaller therapeutic load therefore minimizing adverse effects.<sup>16,17</sup>

Many approaches using various material compositions and surface modifications have been developed to enhance cellular interaction, minimize size, and more importantly increase cellular internalization of nanoparticles. Others have looked into the in vivo imaging properties and drug-delivery capabilities of nanoparticles.<sup>18-22</sup> Such instances include the addition of polyethylene glycol (PEG) polymers to increase circulation time and inhibit opsonization.<sup>23</sup> Through the process of PEGylation, coupling of PEG, nanoparticles can exhibit properties such as suppression of protein adsorption, increase in hydrophilicity, and decreased interaction with serum components to name a few that contribute to its lowered opsonization.<sup>24</sup> As demonstrated by Madan et al.,<sup>25</sup> PEGylated gelatin nanoparticles (GNPs) introduced in murine models show the improved bioavailability compared to the non-PEGylated GNP nanoparticles, which results in a longer circulation time. PEGylation prevents the formation of a protein corona which triggers opsonization, the elimination of foreign by endocytosis, through steric inhibition.<sup>25,26</sup>

The recombination of current technologies and reengineering may provide a suitable theranostic nanoparticle capable of simultaneous drug encapsulation and delivery, enhanced cellular association, and optical properties for visual confirmation of cellular association. Our model hybridizes organic, biocompatible GNPs with inorganic, semiconductive QDs to provide localized optically-identifiable drug-release vehicles for the purpose of minimizing disruptions to cellular mechanisms. The incorporation of targeting ligands directed towards extracellular surface association may prevent negative effects such as apoptosis or occupying the intracellular matrix to cause disruptions to normal cellular function. The functionalization strategies of the model carrier and its cellular interaction will aid to further understand the parameters of developing personalized medicine.

## **3.2 Materials and Methods**

### **3.2.1 Study Design**

Nanoparticle compatibility made from 90 bloom gelatin functionalized via 2 different pathways was assessed on human osteosarcoma U2OS cell derived UTA-6 cells<sup>27</sup> cultured in Dulbecco's Modified Eagle's medium (DMEM, Thermo Fisher Scientific) supplemented with 10% FBS, 100 units/mL penicillin and 100 µg/mL streptomycin at 37 °C with 5% CO<sub>2</sub> under sterile conditions. Cells were grown until 80% confluent and then transferred into multi-well culture plates where they were kept for an additional 24 hours to ensure complete adherence to the surface of the culture dish.

The effect as a result of modifications: i) QDs first followed by anti-IgG or ii) anti-IgG first followed by QDs, was assessed colorimetrically with a MTT cell viability assay. The interaction of the conjugated GNPs was visually with a Nikon Ti Eclipse inverted microscope outfitted with an incubation chamber for live cell imaging. 2D brightfield and FITC-filtered 2D images and 3D z-stack images were collected to visualize the depth of GNPs interaction with cells. The microscope was focused at 250 µm, which pertained to the height of which the surface of the cells was clearly visible.



### 3.2.2 Gelatin Synthesis

GNPs were synthesized according to the two-step desolvation method by Coester et al.<sup>28</sup> from 90 bloom Type A gelatin from porcine skin (**Figure 3-1**). In short, 2.5 g of gelatin was dissolved in 50mL of 18.2 MΩ•cm water under constant stirring at 40°C for 15 min. In all, 50mL of acetone was added to desolvate the gelatin for 5 min, which was then collected and centrifuged at 5000 G for 15 min. The supernatant containing lower molecular weight gelatin was discarded.

The gelatin was then redissolved in 50mL of acidified (pH 2.5) deionized water at 40 °C under constant stirring. A total of 150mL of acetone was added drop-wise to desolvate the gelatin. The gelatin was crosslinked with 500 mL of glutaraldehyde (25% solution) and allowed to stir at 40 °C for 30 min. The GNP was thrice collected and centrifuged at 6000 r/ min for 15 min thrice with ethanol. GNPs were redispersed in ethanol and dried.

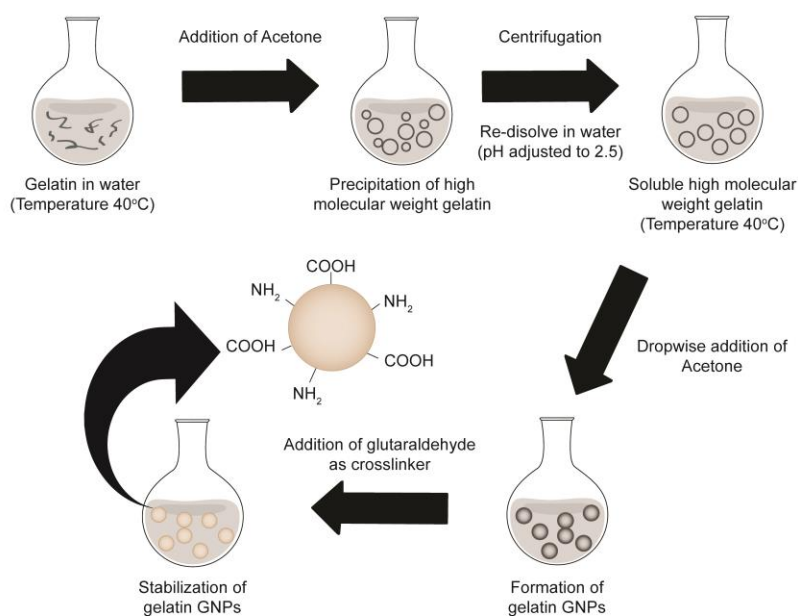


**Figure 3-1.** Two-step desolvation method of gelatin nanoparticle (GNP) synthesis. Stabilization of GNPs was achieved by crosslinking with glutaraldehyde.

### 3.2.3 CdSe/ZnS Cysteamine Modified Quantum Dots

Here we produced CdSe/ZnS QDs through a chemical method described by Duong and Rhee.<sup>29</sup> These QDs were further functionalized with cysteamine (HSCH<sub>2</sub>CH<sub>2</sub>NH<sub>2</sub>) through a thiol exchange method with primary amine groups to be water-soluble and primed for GNP hybridization.<sup>30</sup> The resultant sample CdSe/ZnS/Cys QDs from here on simply known as QDs was hybridized onto the surface of the GNP. In addition, the photoluminescence of the fluorescent QDs was investigated by a QuantaMaster™ 40 Spectrofluorometer (Photon Technology International Inc) is reported in **Figure 3-2**.

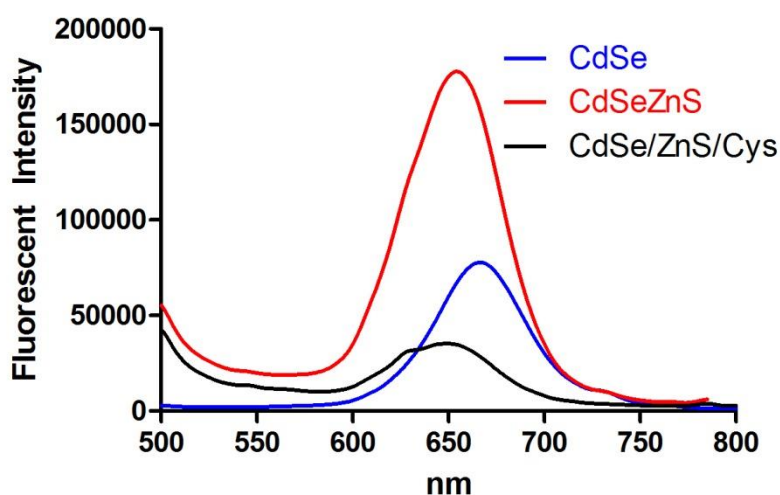


**Figure 3-2.** Fluorescence Change of CdSe QD with Subsequent Modifications. Modification of the CdSe with zinc sulfide (ZnS) and cysteamine hydrochloride (Cys) blue shifted the QD. As a result of the introduction of amine groups, a marked decrease in fluorescent intensity is observed.

### 3.2.4 PEG-epoxide Synthesis

As per the method of Kaul and Amiji<sup>31</sup> for PEG-epoxide synthesis, monomethoxy-poly(ethylene glycol) (PEG, MW: 5000 g/mol) was converted into an epoxide for conjugation. A 5-mM solution of monomethoxy- PEG in N,N-dimethylformamide containing 1% (w/v) of triethanolamine was heated at 40 °C for 4 h with constant stirring then cooled to room temperature. To this solution, 5:1 molar ratio of epichlorhydrin to PEG was added and stirred overnight under reflux conditions. The epoxide derivative

was precipitated in cold diethyl ether. The PEG-epoxide was washed thrice with diethyl ether and dried in vacuum.

### 3.2.5 Functionalization Strategy

The base GNP model was modified via two paths; Path A – QD first followed by anti-IgG and Path B – anti-IgG first followed by QD (**Figure 3-3**). The model utilizes a buffer to form covalent bonds through a dehydration reaction between carboxylic groups (-COOH) and primary amine groups (-NH<sub>2</sub>) to form an amide bond (-CONH-).

Approximately 50 mg of GNP was reacted in 5mL of pH 8.5 borate buffer with 50 mg of CdSe/ZnS/Cys QDs or 200 mL of a stock non-fluorescently tagged antihuman IgG Fab (4 mg/mL) solution for 2 h under constant agitation. The hybridized GNP was purified through a 100 kDa Eppendorf centrifugal tube filter thrice at 5000 r/min for 5 min with ethanol. Collected modified GNP was resuspended in the buffer to conjugate the remaining component or resuspended in ethanol for storage.

The model functionalized by Path A or Path B was then capped with PEG. In all, 25 mg of GNP-QD/anti-IgG or GNP-anti-IgG/QD was suspended in 5mL of the aforementioned buffer along with 10 mg of PEG-epoxide under constant agitation to bioconjugate overnight. PEG capped GNP was purified through a 100-kDa Eppendorf centrifugal tube filter thrice at 5000 r/min for 5 min with ethanol. The PEG modified particles were redispersed in ethanol and dried.

\*Post-synthesis functionalizations are listed in the order of modification in the sample designation. (ex: GNP-QD-anti-IgG; GNPs modified with QDs first followed by anti-IgG)

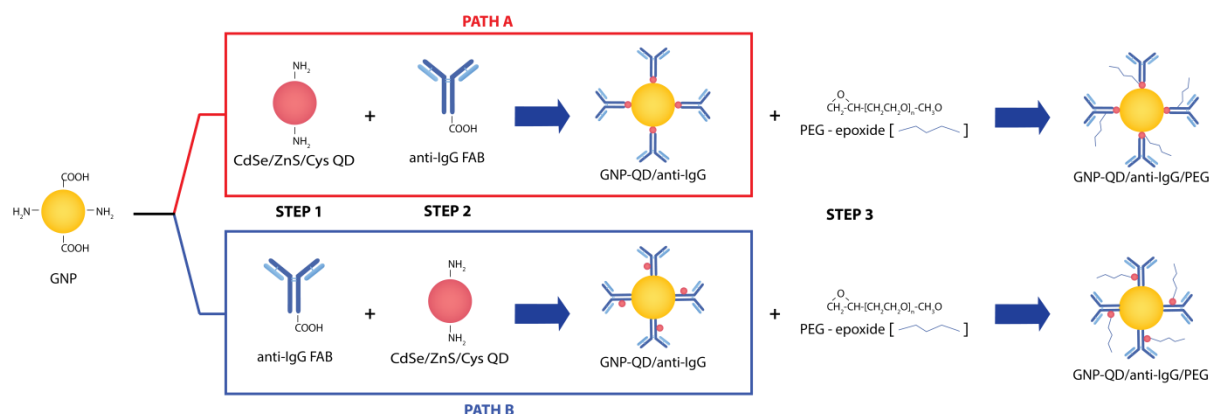


**Figure 3-3.** Schematic of GNP modifications. Modification paths of 90 bloom-based GNP: Path A - Cadmium Selenium Cysteamine modified Quantum Dots (CdSe/ZnS/Cys QD) first; Path B - anti-human Immunoglobulin G Fab (anti-IgG) first. The order of modification exposes different groups on the surface for subsequent modifications. Modifications rely on the formation of amide (-CONH-) bonds to covalently stabilized the constituents. \*constituents are listed in order of modification.

### 3.2.6 Confirmation of QD, anti-IgG and PEG modifications

A colorimetric assay was performed to confirm the successful incorporation of anti-IgG, QD, and PEG onto the surface of the GNP. In triplicate, 5 mg of the various modified and non-modified GNP samples suspended in 100 mL of deionized water was incubated with 5 mL of a 1 M solution of 2,4,6-trinitrobenzenesulfonic acid (TNBS). Samples were left at room temperature for 2 h to react the primary amine groups with TNBS. The absorbance measured at 405 nm was normalized to the measured non-modified GNP. Meanwhile, transmission electron microscopy (TEM, Philips CM-10 operated at 80 kV) was carried out to characterize the particle size of hybrid GNP with/without modifications.

### 3.2.7 Materials Characterization

Materials microstructure were investigated by a Philips CM-10 transmission electron microscope (TEM) operating at 100 kv and a high resolution TEM (JEOL 2010 F, operating at 200 kv). The diameter of the nanoparticles were analyzed with ImageJ software (National Institutes of Health, USA) with an ANOVA and Kruskal-Wallis ( $p < 0.0001$ ).

### 3.2.8 Quantification of QD and anti-IgG

#### *Quantification of QD*

The amount of QDs conjugated to the GNP and GNP anti-IgG was determined by measuring the absorbance at 490 nm in triplicate. The measured value was compared to a four-point standard curve to determine the amount of QDs on the functionalized GNP (**Figure 3-4A**).

#### *Quantification of anti-IgG*

Confirmation of anti-IgG bioconjugation onto the surface was confirmed measuring the residual anti-IgG content not conjugated to the GNP. The filtrate collected from the centrifugation process contained the remainder of the anti-IgG protein not conjugated to the GNP. The protein concentration of this solution was determined colorimetrically with a Thermo Scientific Micro BCA Protein Assay Kit using the anti-IgG stock solution to generate a four-point standard curve (**Figure 3-4B**). In short, the bicinchoninic acid (BCA) can be reduced by specific amino acids in an alkaline environment to form a water-soluble product, which has a typical absorbance at 560 nm.

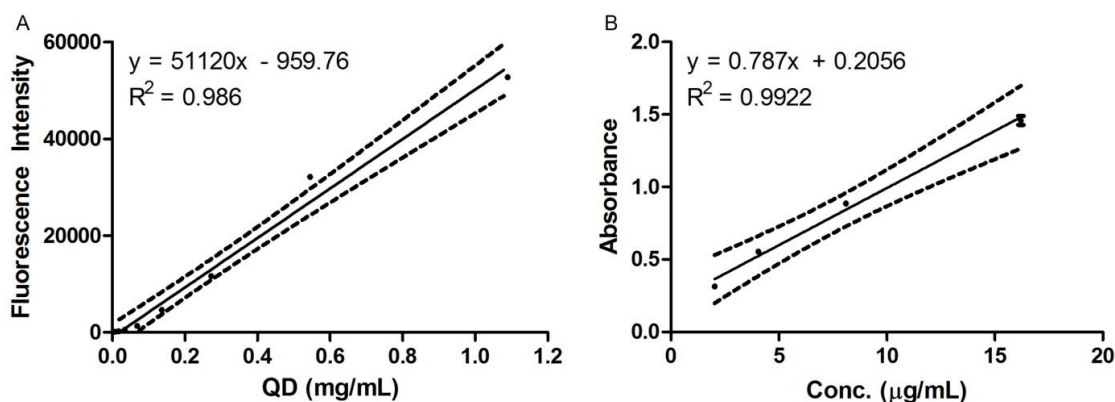


**Figure 3-4.** Standard Curves. A) Fluorescence intensity of QD. B) Absorbance of anti-IgG. The fluorescent standard curve was used to determine the amount of QD hybridized onto the GNP surface. The absorbance aided in determining the amount of anti-IgG remaining after the bioconjugation as a means to back calculate the amount that was bioconjugated.

### **3.2.9 Biocompatibility**

#### *Cell Viability*

24-hour cell viability of the functionalized GNPs was assessed. Approximately 50,000 cells were seeded into each well of a 24 well plate and cultivated overnight at 37 °C. UTA-6 cells were incubated with 5, 10, 20, and 40 µg of samples functionalized with QDs and anti-IgG with/without PEG for 24 hours at 37 °C in triplicate. The cell media was aspirated and rinsed twice with sterile PBS to remove free nanoparticles. Each well was incubated with 200 µL of growth media and 50 µL of sterile 0.5% MTT solution (0.5 mg MTT formazan powder/mL of deionized water) for 4 hours. The media was aspirated and wells were twice rinsed with sterile PBS. 150 µL of DMSO was added to each well to lyse the cells and to dissolve the tetrazolium salt. The absorbance of the plates was measured at 490 nm.

#### *Cellular Interaction*

The interaction of the conjugated GNP was assessed visually with a Nikon Ti Eclipse inverted microscope outfitted with an incubation chamber for live cell imaging where cells were incubated at 37°C in 5% CO<sub>2</sub>. Brightfield and FITC images of the cells were collected in 2D and 3D z-stack to visualize the depth of GNP interaction with cells.

Specificity of the conjugated GNP interaction with UTA-6 cells was assessed in 24-well plates; 125,000 cells were transferred into each well of a 24-well plate and incubated overnight. In triplicate, 100 mg of each type of fluorescently labeled GNP was incubated with cells for 30 min at 37 °C. After this incubation, the cells were rinsed twice with sterile PBS to remove free particles. Wells were made up to 400 µL with sterile PBS and excited at 490 nm.

### **3.2.10 Statistical Analysis**

In order to determine the statistical significance in size as a result of hybridization and bioconjugation with anti-IgG, QDs, and PEG, we performed a One-Way analysis of variance (ANOVA) using GraphPad Prism (GraphPad Software Inc, La Jolla, CA, USA).

Bioconjugation of QDs and anti-IgG was assessed with a t-test, to assess a potential difference in the bioconjugation amount as a result of functionalization pathway. Furthermore, we assessed the cell viability of GNPs functionalized with QDs, anti-IgG, and PEG with a Two-way ANOVA to study the impact of modification order and concentration. Cell viability was assessed with a Two-Way ANOVA to study the impact as a result of modification and concentration. Difference in amine groups to confirm functionalization assessed with a TNBS assay was statistically compared with a one-way ANOVA test. All statistical analyses were assessed at the 95% confidence level.

### 3.3 Results

Our research on 90 bloom-based GNP emphasizes the physical characterization and cellular interaction of functionalization with CdSe/ZnS/Cys QDs, anti-human IgG Fab, and PEG. GNP base modification with QD and anti-IgG was characterized using TEM. The diameters of the GNPs calculated with ImageJ are presented in **Figure 3-5B** along with a TEM micrograph of the hybridized QD. Highly crystallized CdSe/ZnS QDs ( $5 \pm 2$  nm) characterized by high-resolution TEM (**Figure 3-5A; inset**) was found to be hybridized sporadically along the surface of the nanoparticles. The average size of bare GNP is estimated to be  $167 \pm 43$  nm. With base modifications of QDs ( $180 \pm 37$  nm) and anti-IgG, a Kruskal-Wallis ANOVA analysis suggested the anti-IgG is the cause of the significant size increase ( $p < 0.0001$ ), resulting in an increase to  $227 \pm 50$  nm.

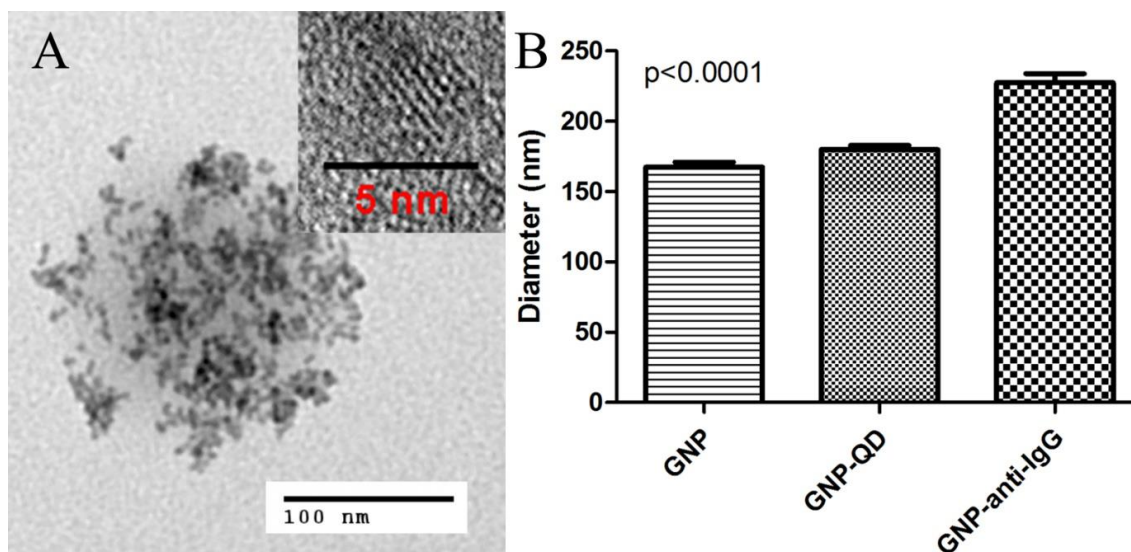


**Figure 3-5.** Microstructures of hybrid nanoparticles. A) TEM micrograph of hybrid nanoparticles GNP-QD is shown with clusters of hybridized QDs on the surface. B) Diameters of GNP indicate a significant increase with the bioconjugation of anti-IgG Fab from  $167 \pm 43$  nm to  $227 \pm 50$  nm ( $p < 0.0001$ ). The same is observed when hybridized with CdSe/ZnS/Cys QD ( $180 \pm 37$  nm).

GNP modified by Path A (QD first) and Path B (anti-IgG first), respectively, with free primary amine groups was capped with PEG to increase biocompatibility. A significant difference ( $p < 0.05$ ) in size between the two paths is observed as shown in **Figure 3-6**. The average particle size of GNP-QD/anti-IgG without and with PEG modification produced through Path A is estimated at  $246 \pm 68$  nm and  $264 \pm 79$  nm; whereas the average particles size of the hybrid GNPs without and with PEG modification produced through Path B is reduced to  $213 \pm 47$  nm and  $224 \pm 46$  nm.



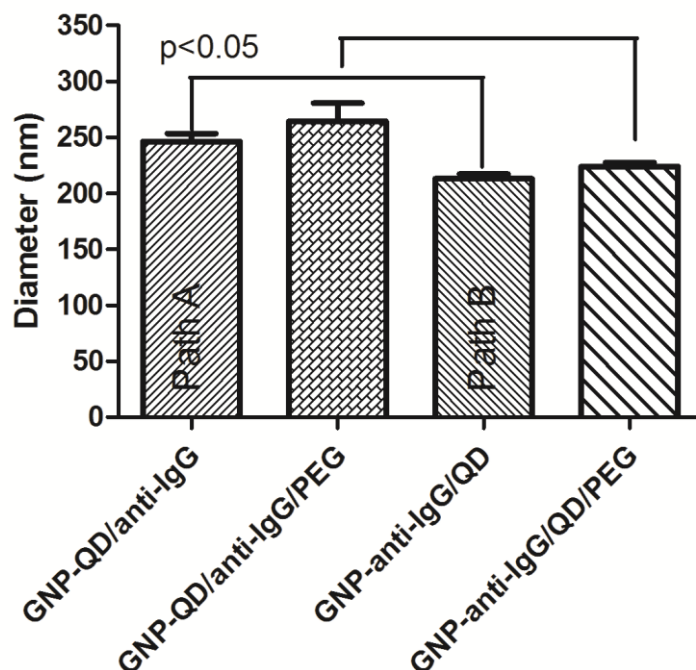


**Figure 3-6.** Average particle size of functionalized nanoparticles via Paths A and B. Particles modified via Path B (anti-IgG first) demonstrated a significantly smaller diameter in comparison to its respective counterpart when modified via Path A (QD first) with  $p < 0.05$ .

A TNBS assay performed was able to simultaneously confirm the successful Paths A and B modifications of the individual components; anti-IgG, QD, and PEG. The change in free primary amine groups was normalized to bare GNP. Increases and decreases in the relative change confirmed the successful hybridization of QD, bioconjugation of anti-IgG, and PEGylation. Shown in **Figure 3-7**, the TNBS assay was able to detect the minute changes in free primary amine groups relative to unmodified GNP as constituents were bonded to the model. **Figure 3-7B** ( $p = 0.0439$ ) demonstrated an increase in amine groups as a result of the QD hybridization. No significant changes in free primary amine groups were observed ( $p = 0.0508$ ) between modification with anti-IgG + QD versus anti-IgG + QD + PEG. Table 1 summarizes the effect of modification order on the amount of constituents that can be hybridized or conjugated onto the surface of GNP. T-test analysis on the order of modification, Path A or Path B, does not significantly impact the amount of anti-IgG ( $p = 0.1000$ ) or QD ( $p = 0.0727$ ) able to be amalgamated to the GNP surface.

It is noted that the results of a t-test analysis suggests no significant difference in conjugation amounts between the two paths of modification.

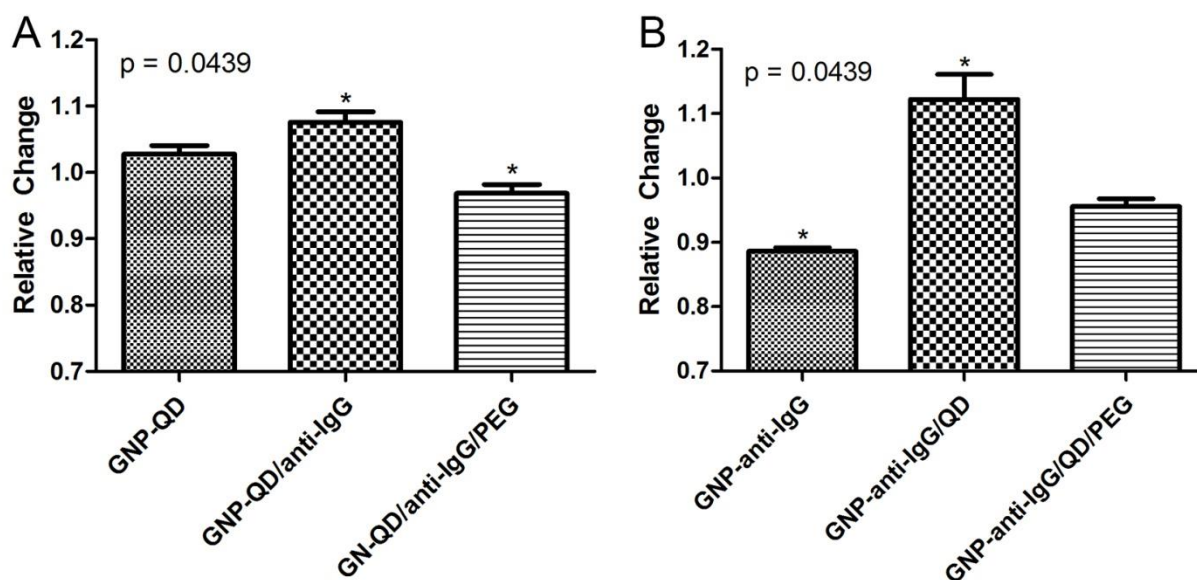


**Figure 3-7.** Change of free primary amine groups in GNP with subsequent modifications relative to unmodified GNP. A) Relative change after modification by Path A. Conjugation of PEG significantly reduces the amount of amine groups found on the surface ( $p = 0.0439$ ). B) Path B changes demonstrated the QDs add a significant amount of amine groups ( $p = 0.0439$ ) but is later reduced by the addition of PEG.

**Table 3-1.** Impact of modification order on functionalization.

Modification	Path A	Path B	p Value
Anti-IgG ( $\mu\text{g}/\text{mg}$ GNP)	$6.33 \pm 0.04$	$7.06 \pm 0.02$	0.1000
QD ( $\mu\text{g}/\mu\text{g}$ GNP)	$0.81 \pm 0.34$	$1.03 \pm 0.003$	0.0727

The corresponding cellular interaction and internalization of the GNPs modified via Path A and B were observed with a Nikon inverted microscope outfitted for live cell imaging. From **Figure 3-8**, we are able to visualize the interaction of bare GNP, GNP-QD/anti-IgG, and GNP-QD/anti-IgG/PEG with the UTA-6 cells. With the focus set to 250 nm, we visualized the internalization and surface association more clearly with lower fluorescence intensity. Of those visible internalized GNP, **Figure 3-8E** indicates more of

the PEG modified GNP accumulates within or near the surface of the UTA-6 cells compared to those without PEG, **Figure 3-8C**. Visual confirmation suggests more functionalized GNPs (**Figure 3-8B and D**) interact with UTA-6 cells in comparison to the bare GNP (**Figure 3-8A**). Similar results can be observed with GNP modified by Path B (**Figure 3-9**). Respective nanoparticles are outlined in red.

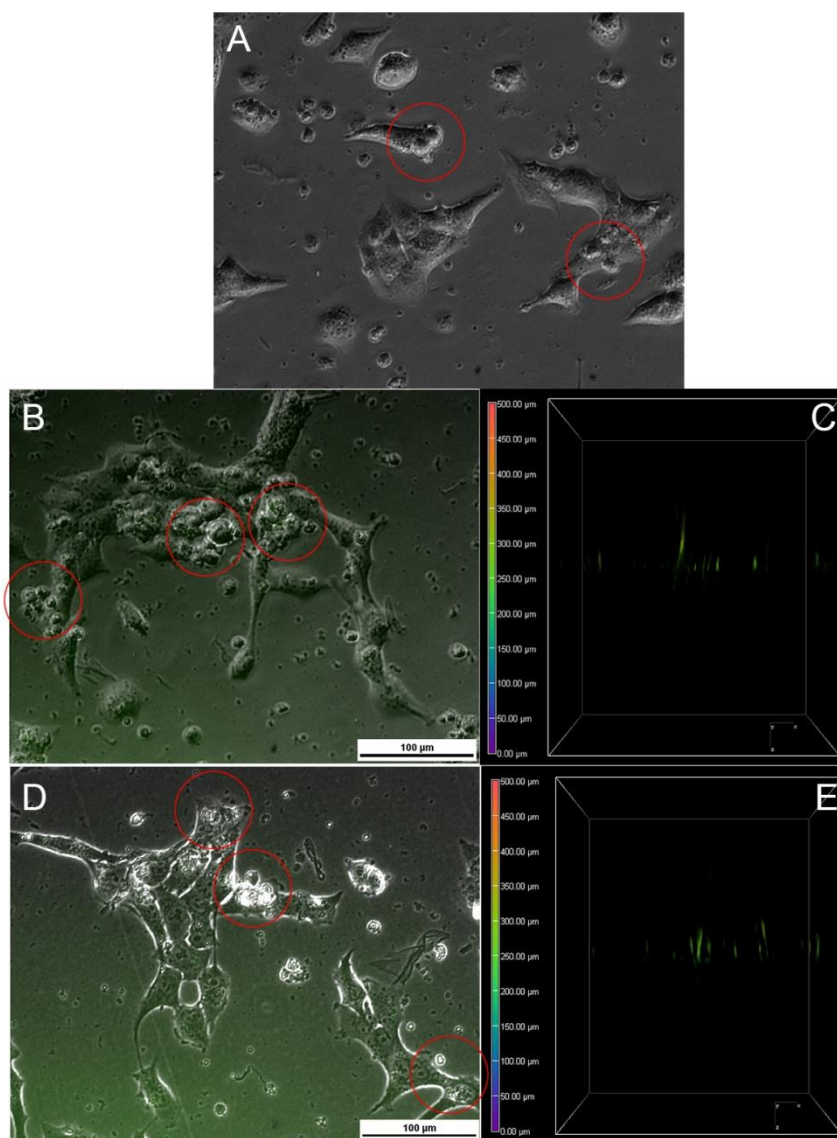


**Figure 3-8.** Interaction of Path A modified GNP with UTA-6 cells. A) Brightfield of bare GNP. B and C) GNP-QD/anti-IgG fluorescence and z-stack, respectively. D and E) GNP-QD/anti-IgG/PEG's corresponding overlay and z-stack, respectively. Functionalized GNPs exhibit increased cellular interaction and bright fluorescence that is optically trackable. Nanoparticles are outlined in red.

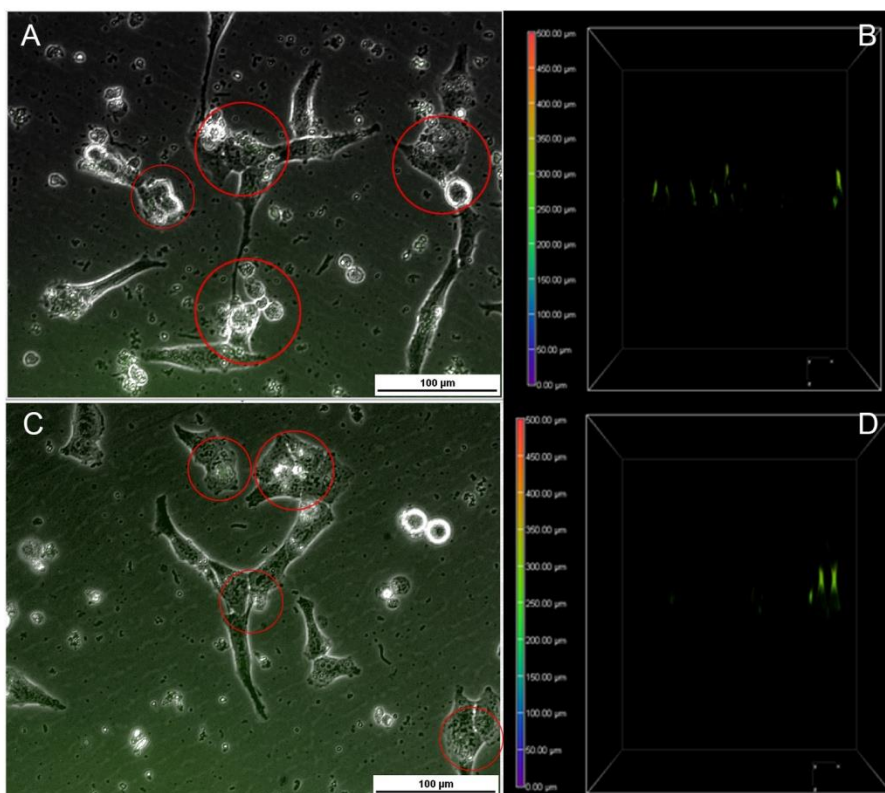


**Figure 3-9.** Cellular Interaction of GNP-anti-Ig/GQD and GNP-anti-IgG/QD/PEG with UTA-6 cells. Internalization and surface association is also observed in the fluorescent and brightfield overlay of A) GNP-anti-IgG/QD and B) GNP-anti-IgG/QD/PEG. Respective z-stacks are seen in B) and D). Taking 250  $\mu\text{m}$  as the cell surface, all fluorescent signals detected below it were considered internalized. Nanoparticles are outlined in red.

The effect of modification strategies on cellular viability was assessed with an MTT assay, to determine the cell viability in triplicate of 25,000 UTA-6 cells treated with various amounts of modified and unmodified GNPs: 5, 10, and 20 mg for 24 h. Shown in **Figure 3-10** are the relative cell viability results of GNP modified with anti-IgG and QD. The relative viability was calculated by normalizing the results to the absorbance of untreated UTA-6 cells. A two-way ANOVA of the relative viability is dependent on both sample type and sample amount. In comparison to the non-modified GNP, both the GNP-QD/anti-IgG and GNP-anti-IgG/QD exhibit a significant difference ( $p < 0.0001$ ) with a negative correlation with increasing amounts of sample. Furthermore, in comparing the

functionalized samples, anti-IgG/QD samples exhibited a significant decrease ( $p < 0.05$ ) in overall viability than QD/anti-IgG functionalized samples.

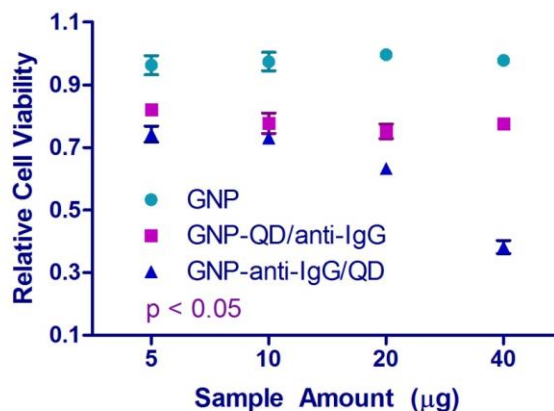


**Figure 3-10.** Average cell viability of functionalized GNP. Bare GNP demonstrated significant difference in viability with modified GNP ( $p < 0.001$ ). A decline in viability is observed with increasing concentration. At a concentration of 40 µg, there was an observed significant difference between GNP-QD/anti-IgG and GNP-anti-IgG/QD ( $p < 0.01$ ), with GNP-anti-IgG/QD at a greater rate of decline.

The GNP-QD/anti-IgG sample, shown in **Figure 3-11A**, exhibited a significantly higher relative cellular viability compared to its PEGylated counterpart (GNP-QD/ anti-IgG/PEG) with  $p = 0.0034$ . A two-way ANOVA analysis confirmed the PEG negatively affected the relative cell viability ( $p = 0.0034$ ). The opposite was observed for samples modified by Path B (**Figure 3-11B**;  $p = 0.0019$ ), where PEG aided in improving cellular viability.

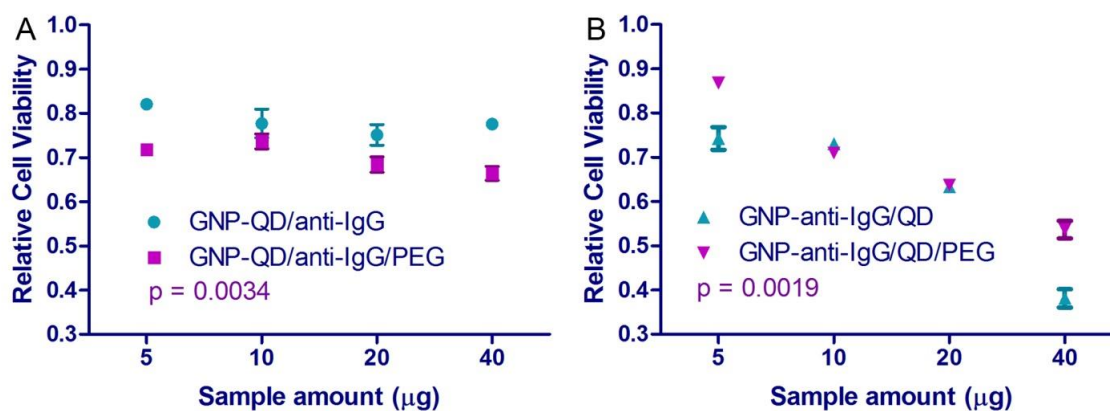


**Figure 3-11.** Relative cellular viability of the GNP model capped with PEG after 24-h incubation. A) Relative viability of PEG-capped GNP modified by Path A. In comparison to its PEG-capped counterpart, the GNP-QD/anti-IgG has a significantly higher relative viability ( $p = 0.0034$ ) at 5 and 40  $\mu\text{g}$ . The PEG modification decreased the relative viability consistently with increasing sample amount. B) Conversely, PEG mitigated the decrease in viability seen in GNP-anti-IgG/QD samples. PEG modification significantly increased the relative cell viability ( $p = 0.0019$ ) at 5 and 40  $\mu\text{g}$ .

### 3.4 Discussion

Our GNP model provides insight into the impact of modification strategy on the potential for GNPs to be utilized in a theranostic fashion for *in vivo* fluorescent imaging and enhanced cellular interaction.

From our investigation into the functionalization of the GNPs with anti-IgG, QDs, and PEG, it is evident that the source of the increase of amine groups is due to the addition of QDs as seen in Figure 3-7B; as to be expected due to the thiol exchange from the cysteamine onto the QDs. From both figures, it is evident the PEG and the anti-IgG are conjugating with primary amine groups, hence the visible decrease in relative amine presence. Furthermore, a comparison between relatively similar modifications, anti-IgG + QD and anti-IgG + QD + PEG, evidenced no significant change in free primary amine groups ( $p = 0.0508$ ). The functionalization is dependent on the formation of amide bonds which directly impacts the amount of QD or anti-IgG capable of being conjugated onto the GNP surface.

Fundamentally, the GNP modified by either paths exhibited similar physical characteristics (**Figure 3-3**). Modifications despite order did not significantly impact the amount of QD or anti-IgG able to be hybridized or bioconjugated, respectively (Table 1), while there was a significant difference in size ( $p < 0.05$ ) respective to Paths A and B modified with PEG (**Figure 3-6**). The main impact on size was the addition of anti-IgG (**Figure 3-5**). An enquiry into cellular interaction reveals differences in the interaction based on modification strategies.

Due to the physical chemical nature of the GNP, an accurate measure of the number of particles interacting with the UTA-6 cells could not be quantified. Not all particles could be tagged with a significant amount of QDs to generate a detectable signal (**Figure 3-8**). However, from the live cell imaging, a distinction between the cellular interaction between functionalized and bare GNP could be clearly observed. GNP modified with anti-IgG exhibited enhanced interaction properties compared to non-modified GNPs. **Figure 3-8 and 3-9** suggests the addition of PEG aids the GNP to be internalized more readily than those without.

Cellular toxicity is a factor to be considered in all therapeutic settings. A suitable nanocarrier must minimize the impact to healthy cells while executing its function. One primary goal of our nanocarrier was to maintain good cellular viability in efforts to manage the symptoms of incurable diseases and delay progression in a therapeutic capacity. The results indicate functionalization strategy: (a) type and (b) order of modification are major factors in overall viability.

The size of a nanoparticle can determine its feasibility to be internalized by a cell. As seen in the z-stacks in **Figure 3-8 and 3-9**, we observed functionalized nanospheres with and without PEG to be both associated onto the surface of the UTA-6 cells and internalized based on the location of the fluorescent signal. The result of internalization of small particles through endocytosis, though the internalization mechanism is still unclear, can be detrimental to the overall health of cells.<sup>32,33</sup>

The order of modification may attribute to the sharp decrease in overall viability as observed with increasing sample amount. From the viability data (**Figure 3-10**), we can

see particles hybridized with QD first (Path A) exhibit a higher relative cellular viability than those functionalized with anti-IgG first (Path B). The addition of anti-IgG to the hybridized GNP-QD resulted in the capping of the amine groups found on the surface of the QD leading to a minimized exposure to the cell. On the other hand, the addition of QD to the bioconjugated GNP-anti-IgG may have resulted in the presence of QD hybridizing to carboxylic acid groups on the surface of the anti-IgG antibody, thereby exposing its amine-rich surface. The resultant exposure of the amine rich QD to the cell may have contributed to the decreased viability seen with the GNP-anti-IgG/QD. As demonstrated by Kim et al.<sup>34</sup> with polystyrene-modified nanoparticles, different terminal functional groups can interfere with the natural progression of the cell cycle. The presence of amine groups caused the cell cycle to arrest at G1/S and G2/M phases in mitosis whereas carboxyl groups did not. In our model, the order of modification was vital to limiting the exposure of primary amine groups with the UTA-6 cells. Nanoparticles modified with QD first exhibited greater cell viability overall.

Furthermore, the significant difference in relative viability ( $p < 0.001$ ) between the GNP-QD/anti-IgG and GNP-anti-IgG/QD can be observed as shown in **Figure 3-11**. GNP-anti-IgG/QD exhibited a markedly lower viability at higher amounts (20  $\mu\text{g}$  +) of introduced particles. Therefore prompting an attempt to mitigate the lowered viability in general through the incorporation of PEG, which has been shown to enhance biocompatibility.<sup>24-26,29</sup> **Figure 3-11** shows the relative cell viability of the hybrid GNP with different surface modification results of the investigation on the addition of PEG. A series of analyses have demonstrated both order and PEG can play a role in affecting cellular viability. The PEG was able to increase relative viability of GNP-anti-IgG/QD significantly ( $p = 0.0019$ ), but not to the levels shown by Path A. Shown in **Figure 3-11**, the PEG substantially increased the overall viability, even with increasing sample amount. However, the addition of PEG to Path A, though having a negative impact, maintained viability above 65% at 40 mg while Path B dropped below 60%.

The addition of PEG to Path A modification may have promoted an increased accumulation at the site of interest in combination of a recognition element, in our case the anti-IgG.<sup>35</sup> The addition of PEG increases a free energy change during endocytosis



process allowing for a more readily internalized particle.<sup>36</sup> The direct result of enhanced internalization into the cytoplasm may lead to disruptions in cytoskeletal formations. Through immunostaining Gupta et al.<sup>37</sup> demonstrated their nanoscopic GNP ( $37 \pm 0.84$  nm) caused the formation of vacuoles within the cell body resulting in the anisotropic formation of F-actin with poorly developed filament bundles. The relative cell viability of our model corroborates with what Gupta et al. observed, a decrease in overall viability due to internalization. Furthermore, these cellular filaments were observed to protrude from the cell as a result of internalization.

### 3.5 References

1. Hans, M. L. & Lowman, A. M. Biodegradable nanoparticles for drug delivery and targeting. *Curr. Opin. Solid State Mater. Sci.* **6**, 319–327 (2002).
2. Lee, E. J., Khan, S. A. & Lim, K.-H. Gelatin Nanoparticle Preparation by Nanoprecipitation. *J. Biomater. Sci. Polym. Ed.* **22**, 753–771 (2011).
3. Elzoghby, A. O. Gelatin-based nanoparticles as drug and gene delivery systems: Reviewing three decades of research. *J. Control. Release* **172**, 1075–1091 (2013).
4. Azimi, B., Azimi, B., Nourpanah, P., Rabiee, M. & Arbab, S. Producing Gelatin Nanoparticles as Delivery System for Bovine Serum Albumin. *Iran. Biomed. J.* **18**, 34 (2014).
5. Kaul, G. & Amiji, M. Biodistribution and targeting potential of poly(ethylene glycol)-modified gelatin nanoparticles in subcutaneous murine tumor model. *J. Drug Target.* **12**, 585–591 (2005).
6. Azarmi, S., Huang, Y. & Chen, H. Optimization of a two-step desolvation method for preparing gelatin nanoparticles and cell uptake studies in 143B osteosarcoma cancer cells. *J. Pharm. Pharm. Scineces* **9**, 124–132 (2006).
7. Choi, K. Y., Liu, G., Lee, S. & Chen, X. Theranostic nanoplatfroms for simultaneous cancer imaging and therapy: current approaches and future perspectives. *Nanoscale* **4**, 330–342 (2012).
8. Liu, Y., Miyoshi, H. & Nakamura, M. Nanomedicine for drug delivery and imaging: A promising avenue for cancer therapy and diagnosis using targeted functional nanoparticles. *Int. J. Cancer* **120**, 2527–2537 (2007).
9. Won, Y. W. & Kim, Y. H. Recombinant human gelatin nanoparticles as a protein drug carrier. *J. Control. Release* **127**, 154–161 (2008).
10. Resch-genger, U., Grabolle, M., Cavaliere-jaricot, S., Nitschke, R. & Nann, T.

- Quantum dots versus organic dyes as fluorescent labels. *Nat. Methods* **5**, 763–775 (2008).
11. Bradburne, C. E. *et al.* Cytotoxicity of Quantum Dots Used for In Vitro Cellular Labeling: Role of QD Surface Ligand, Delivery Modality, Cell Type, and Direct Comparison to Organic Fluorophores. *Bioconjug. Chem.* **24**, 1570–1583 (2013).
  12. Derfus, A. M., Chan, W. C. W. & Bhatia, S. N. Probing the Cytotoxicity of Semiconductor Quantum Dots. *Nanoletters* **4**, 11–18 (2004).
  13. Chen, L., Siemiarczuk, A., Hai, H. & Chen, Y. Development of biocompatible and proton-resistant quantum dots assembled on gelatin nanospheres. *Langmuir* **30**, 1893–1899 (2014).
  14. Mei, J., Yang, L.-Y., Lai, L. & Xu, Z.-Q. The interactions between CdSe quantum dots and yeast *Saccharomyces cerevisiae*: Adhesion of quantum dots to the cell surface and the protection effect of ZnS shell. *Chemosph.* **112**, 92–99 (2014).
  15. Zhao, K. *et al.* Biodegradable Polymeric Nanoparticles as the Delivery Carrier for Drug. *Current Drug Delivery* **13**, 494–499 (2016).
  16. Hu, C.-M. J., Aryal, S. & Zhang, L. Nanoparticle-assisted combination therapies for effective cancer treatment. *Ther. Deliv.* **1**, 323–334 (2010).
  17. De Jong, W. H. & Borm, P. J. A. Drug delivery and nanoparticles: applications and hazards. *Int. J. Nanomedicine* **3**, 133–149 (2008).
  18. Gao, X. *et al.* In vivo molecular and cellular imaging with quantum dots. (2005). doi:10.1016/j.copbio.2004.11.003
  19. Gao, X., Cui, Y., Levenson, R. M., Chung, L. W. K. & Nie, S. In vivo cancer targeting and imaging with semiconductor quantum dots. *Nat. Biotechnol.* **22**, 969–976 (2004).
  20. Voura, E. B., Jaiswal, J. K., Mattoussi, H. & Simon, S. M. Tracking metastatic

tumor cell extravasation with quantum dot nanocrystals and fluorescence emission-scanning microscopy. *Nat. Med.* **10**, 993–998 (2004).

21. Mouli, S. K., Tyler, P., McDevitt, J. L. & Eifler, A. C. Image-guided local delivery strategies enhance therapeutic nanoparticle uptake in solid tumors. *ACS Nano* **7**, 7724–7733 (2013).
22. Ma, L., Kohli, M. & Smith, A. Nanoparticles for combination drug therapy. *ACS Nano* **7**, 9518–9525 (2013).
23. Owens, D. E. & Peppas, N. A. Opsonization, biodistribution, and pharmacokinetics of polymeric nanoparticles. *Int. J. Pharm.* **307**, 93–102 (2006).
24. Jain, N. K. & Nahar, M. PEGylated nanocarriers for systemic delivery. *Methods Mol. Biol.* **624**, 221–234 (2010).
25. Madan, J. *et al.* Long-circulating poly(ethylene glycol)-grafted gelatin nanoparticles customized for intracellular delivery of noscapine: preparation, in-vitro characterization, structure elucidation, pharmacokinetics, and cytotoxicity analyses. *Anticancer. Drugs* **22**, (2011).
26. Suk, J. S., Xu, Q., Kim, N., Hanes, J. & Ensign, L. M. PEGylation as a strategy for improving nanoparticle-based drug and gene delivery. *Adv. Drug Deliv. Rev.* **99**, 28–51 (2016).
27. Englert, C. *et al.* WT1 suppresses synthesis of the epidermal growth factor receptor and induces apoptosis. *EMBO J.* **14**, 4662–4675 (1995).
28. C. J. Coester H. Von Br, K. L. & C. J. Coester, K. L. Gelatin nanoparticles by two step desolvation a new preparation method, surface modifications and cell uptake. *J. Microencapsul.* **17**, 187–193 (2000).
29. Duong, H. D. & Rhee, J. I. Use of CdSe/ZnS core-shell quantum dots as energy transfer donors in sensing glucose. *Talanta* **73**, 899–905 (2007).

30. Larson, D. R. *et al.* Water-Soluble Quantum Dots for Multiphoton Fluorescence Imaging in Vivo. *Science* (80-. ). **300**, 1434–1436 (2003).
31. Kaul, G. & Amiji, M. Long-Circulating Poly(Ethylene Glycol)-Modified Gelatin Nanoparticles for Intracellular Delivery. *Pharm. Res.* **19**, 1061–1067 (2002).
32. Shang, L., Nienhaus, K. & Nienhaus, G. U. Engineered nanoparticles interacting with cells: size matters. *J. Nanobiotechnology* **12**, 5 (2014).
33. Verma, A. & Stellacci, F. Effect of Surface Properties on Nanoparticle–Cell Interactions. *Small* **6**, 12–21 (2010).
34. Kim, J. A. *et al.* Low Dose of Amino-Modified Nanoparticles Induces Cell Cycle Arrest. *ACS Nano* **7**, 7483–7494 (2013).
35. Jokerst, J. V, Lobovkina, T., Zare, R. N. & Gambhir, S. S. Nanoparticle PEGylation for imaging and therapy. *Nanomedicine (Lond)*. **6**, 715–728 (2011).
36. Li, Y., Kröger, M. & Liu, W. K. Endocytosis of PEGylated nanoparticles accompanied by structural and free energy changes of the grafted polyethylene glycol. *Biomaterials* **35**, 8467–8478 (2014).
37. Gupta, A. K., Gupta, M., Yarwood, S. J. & Curtis, A. S. G. Effect of cellular uptake of gelatin nanoparticles on adhesion , morphology and cytoskeleton organisation of human fibroblasts. *J. Control. Release* **95**, 197–207 (2004).

## CHAPTER 4

*To quantitatively assess our upconversion nanoparticles (UCNPs) functionalized with anti-human vascular endothelial growth factors (VEGF) as a treatment for angiogenic prone diseases by binding to extracellular VEGF. The UCNPs provides bimodal imaging (ie: MRI and fluorescent) and tracking capabilities. Our endeavour is to assess the anti-angiogenic properties of the UCNP model in comparison to bare-antiVEGF as a means for alternative treatment for angiogenic prone diseases such as cancer and wet-age related macular degeneration with diagnostic relevance.*

*The contents of this chapter are a compilation of two original research articles; a) WH. Tse, S. Yang, and J. Zhang. Bimodal imaging compatible theranostic nanoparticles for anti-angiogenic treatment. b) WH. Tse, L. Chen, CM. McCurdy, CM. Tarapacki, BA. Chronik, and J. Zhang. Biocompatible imaging with NaGdF<sub>4</sub>: Er<sup>3+</sup>, Yb<sup>3+</sup> Upconversion Nanoparticles on HUVEC Cells. (To be submitted August 2017).*

## **4 BIMODAL IMAGING COMPATIBLE THERANOSTIC NANOPARTICLES FOR ANTI-ANGIOGENIC TREATMENT**

### **4.1 Introduction**

Nanoparticle theranostic applications for drug delivery are a state-of-the-art concept to provide both biomedically relevant mode of imaging tracking and therapeutics in one model. Current technology is limited by bioavailability of therapeutics and imaging limitations or lack thereof which prevents it from achieving its full potential. Nanoparticles provide an optimal foundation for the development of next generation multifunctional and multi-disease viable therapeutic options. One application of nanoparticles is for the treatment of angiogenic prone diseases such as cancer and wet age-related macular degeneration (AMD) with anti-vascular endothelial growth factors (anti-VEGF) for adjunct and primary care, respectively.<sup>1-4</sup>

In cancer it is well documented angiogenesis is required for solid tumor growth.<sup>5,6</sup> Clinical applications of anticancer agents aside from chemotherapy rely on anti-VEGF as adjunct treatments to greatly improve efficacy of treatment.<sup>7</sup> Bevacizumab, was the first VEGF inhibitor approved for use to treat metastatic colorectal cancer, which improved survival of patients from 15.6 to 20.3 months.<sup>5,7</sup> Other proposed applications include the use of Mogamulizumab, an anti-chemokine receptor, for the treatment of T-cell leukemia-lymphoma<sup>8</sup> and Apatinib for metastatic breast cancer.<sup>1</sup> For treatment of pathogenic angiogenesis, antibody therapy act to inhibit various pathways in the angiogenic process stimulated by the binding of VEGF to its respective receptors which can promote endothelial cell survival, new blood vessel formation and remodeling, and increased vascular permeability.<sup>6,9,10</sup>

Wet AMD is characterized by choroidal neovascularization, choroidal angiogenesis as a result in the imbalance between proangiogenic VEGF and anti-angiogenic pigment epithelium-derived factor.<sup>11</sup> The pathogenesis of this disease is also multifactorial with age and vascular trauma being severe risk factors.<sup>12</sup> Vision loss and in extreme cases irreversible damage to the retina results as vascular leakage causes an increase in ocular pressure leading to retinal separation.<sup>4,13-15</sup> Antibody treatments such as bevacizumab, ranibizumab, and various others have been routinely used to treat wet AMD with success.<sup>13,14,16,17</sup>

Nanoparticles have been proposed to address specific shortcomings of current technologies. Nanoparticles have the potential to increase efficacy and improve drug delivery which decreasing adverse effects by modulating both pharmacokinetic and pharmacodynamic profiles of drugs for enhancing the therapeutic index.<sup>18</sup> Drugs or antibodies may also be loaded into nanosized carriers for increased *in vivo* stability, extend the blood circulation time, and allow for controlled release.<sup>3,19-21</sup> Nanoparticles may also provide a solution for physical barriers to efficacious treatment such as the blood-retina barrier and corneal barrier.<sup>19</sup> Nanoparticle applications for cancer have been proposed to exploit the enhanced permeability and retention effect (EPR), where nanoparticles will passively accumulate in a tumor due to the presence of leaky intratumoral blood vessels where fenestrations are between 100 – 780 nm in size.<sup>18,22</sup>

Nanoparticles can be repurposed for alternative treatments of wet-AMD are desired as current therapy requires frequent injections to maintain relevant bioavailability and have off-target effects.<sup>23</sup> Suitable nanocarriers for ocular treatments have been developed using biodegradable chitosan and gelatin for sustained drug release.<sup>3,19</sup>

In addition, to improving drug accumulation, therapeutic efficacy, sustained drug release, and increasing drug solubility, nanoparticles offer a unique set of physical characteristics suitable for ferrying therapeutic drugs and providing a platform for biomedical imaging.<sup>24-26</sup> As a direct result of material-based properties, the size, shape, structure, and surface properties can be tailored to suit the needs of any application.<sup>25,27</sup> For instance, biocompatible polymeric nanoparticles (ie: chitosan, gelatin, PLGA, etc.) have demonstrated great biocompatibility and drug encapsulation efficiency suitable for *in vivo* sustained drug release.<sup>27-29</sup>

Biocompatible imaging nanoparticles have been developed to bridge the gap between nanocarriers with theranostic imaging. Current renditions of imaging compatible entities are fluorescent dyes, which are susceptible to photobleaching and potentially genotoxic if the excitation source is near the UV range.<sup>30-32</sup> New advancements in lanthanide based nanoparticles have provided the ideal bimodal imaging entity compatible with both magnetic resonance imaging (MRI) and upconversion fluorescence imaging. Fluoride-based lanthanide cores provide a stable matrix for the doping of lanthanide ions responsible.<sup>33</sup> Gadolinium (Gd), Ytterbium (Yb), and Erbium (Er) have demonstrated satisfactory imaging properties for bimodal imaging.<sup>34-37</sup> Gd, a paramagnetic metal employed in clinical MRI, has been demonstrated by Zhou et al. to provide a stronger T1-weighted imaging signal in the nanoparticle form.<sup>38</sup> The most interesting component of the lanthanide doping is the phenomenon of multiphoton upconversion fluorescence which convert near-infrared light (NIR) into higher energy emissions into the visible colour spectrum.<sup>39-41</sup> This phenomenon exploits the optical transmission window for deeper light penetration, damage to cells, reduced light scattering, and increased image contrast.<sup>36,38</sup> This characteristic would be compatible in ophthalmology where optical coherence tomography is used to assess the morphology of the eye.<sup>40</sup>



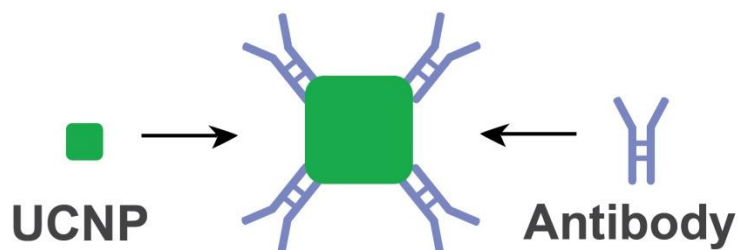


**Figure 4-1.** Schematic of the upconversion nanoparticle antibody model. The UCNP is functionalized with the anti-VEGF antibody to produce a theranostically relevant nanoparticle with bimodal imaging capabilities and anti-angiogenic treatment.

We propose a fluoride-based upconversion nanoparticle (UCNP) core with anti-human VEGF (anti-VEGF) bioconjugated on the surface for the purpose of anti-angiogenesis treatment with bimodal imaging affinities (**Figure 4-1**). The nanoparticle model will be assessed for its potential to be tracked via upconversion fluorescence and traced by magnetic resonance. Furthermore, intend to contrast and compare the nanoparticle model with respect to its non-conjugated anti-VEGF counterpart to quantify potential differences in its anti-angiogenic properties.

## 4.2 Materials and Methods

### 4.2.1 Study Design

The UCNPs functionalized with anti-VEGF was assessed on human umbilical vascular endothelial cells (HUVEC) for biocompatibility and anti-angiogenic effects. HUVECs were grown on a 2% gelatin (w/w) matrix to promote adhesion and provide a suitable foundation for immunocytochemistry (ICC). Furthermore, the UCNP model was assessed for bimodal imaging compatibility for magnetic resonance and fluorescent imaging.

HUVECs were grown in Medium 131 supplemented with microvascular growth supplement (MVGS), 100 units/mL penicillin and 100  $\mu\text{g/mL}$  streptomycin, and 5  $\mu\text{g/mL}$  amphotericin B at 37°C with 5% CO<sub>2</sub> under sterile conditions.

#### 4.2.2 UCNP synthesis surface modification with PEI

Water soluble Gd-based UCNPs doped with polyethylenimine (PEI), Er, and Yb were synthesized according to the method used by Longyi et al. (**Figure 4-2**).<sup>33</sup> In short, 1.6 mmol gadolinium(III) nitrate hexahydrate ( $\text{Gd}(\text{NO}_3)_3 \cdot 6\text{H}_2\text{O}$ ), 0.36 mmol ytterbium(III) nitrate pentahydrate ( $\text{Yb}(\text{NO}_3)_3 \cdot 5\text{H}_2\text{O}$ ), 0.38 mmol erbium(III) nitrate pentahydrate ( $\text{Er}(\text{NO}_3)_3 \cdot 5\text{H}_2\text{O}$ ), 8 mmol sodium fluoride (NaF), 0.7 g PEI (MW ~ 800 by LS, average  $M_n$  ~ 600 by GPC), and 30 mL of ethylene glycol; all purchased from Sigma-Aldrich, were combined in a one pot synthesis reaction to produce NaGdF<sub>4</sub>: Er, Yb (Gd-UCNPs). The solution was heated to 198°C and held for 6 hours with nitrogen under reflux to promote UCNP nucleation and growth. UCNPs were then collected by centrifugation and purified with ethanol thrice. UCNPs were dried with a lyophilizer.

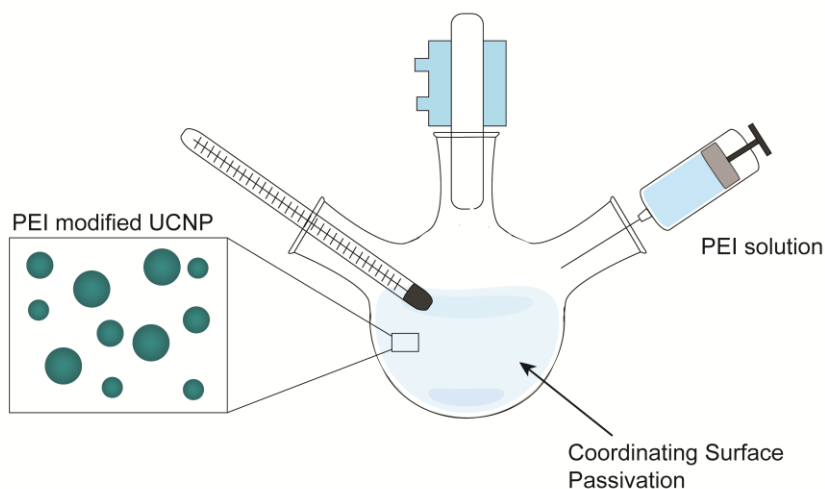


**Figure 4-2.** Synthesis schematic of upconversion nanoparticles modified with PEI. The synthesis occurs in a one pot reaction to grow the NaGdF<sub>4</sub>: Er, Yb UCNPs.

### 4.2.3 UCNP functionalization with anti-VEGF

Polyclonal anti-human VEGF produced in goat (V6627, Sigma-Aldrich) was combined with the as-synthesized UCNPs in a pH 8.5 borate buffer under constant agitation for 2 hours to facilitate a dehydration reaction to covalently link the anti-VEGF to the UCNPs surface. From here on, the bare UCNP shall be referred to as Gd UCNP and the anti-VEGF modified UCNPs shall be referred to as Gd-antiVEGF UCNP.

For applications in ICC, Gd-antiVEGF UCNPS were tagged with FITC using the borate buffer to provide fluorescent tracking during confocal imaging as it is not equipped for upconversion fluorescence imaging.

### 4.2.4 Materials Characterization

UCNPs were characterized with transmission electron microscopy (TEM; Phillips CM-10 at 80 kv) to determine size ( $n = 200$ ) and ICP-MS (Agilent 7700) to determine lanthanide composition. The diameter of the UCNPs from the TEM images was analyzed with ImageJ software (National Institutes of Health, USA). Hi-resolution TEM (HRTEM, FEM Titan 80-300 HB, Gatan 866 model) was used to verify the crystalline structure. The surface modification with PEI was confirmed with Fourier Transform Infrared (FTIR, Bruker Vector 22), in the range of  $600\text{--}4500\text{ cm}^{-1}$  with a resolution of  $4\text{ cm}^{-1}$  and 64 scans.

### 4.2.5 Quantification of anti-VEGF conjugation

Anti-VEGF conjugation was quantified with a protein assay measuring the absorbance of the BCA Assay results at 490 nm. Using a 5 point standard curve as shown in **Figure 4-3**, the amount of anti-VEGF conjugated directly to the surface of the UCNPs was determined.

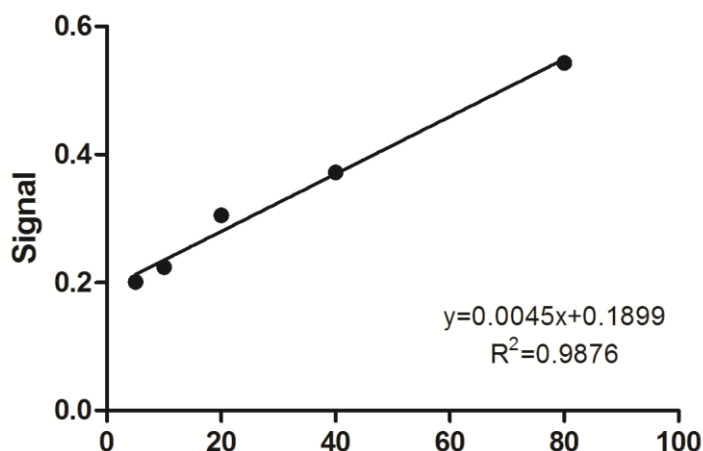


**Figure 4-3.** Anti-VEGF protein assay standard curve. 5 point standard curve for quantifying the directly bioconjugated anti-VEGF.

#### **4.2.6 UCNP fluorescence**

Upconversion fluorescence was assessed with a Spectrofluorometer (QuantaMaster™ 40, Photon Technology International Inc.) equipped with an infrared laser. We assessed the fluorescence of the UCNPs with various laser powers from 0.5 Watt to 1.5 Watt.

#### **4.2.7 Magnetic Properties**

Magnetic resonance imaging compatibility was assessed with a vibrating sample magnetometer (VSM, Lake Shore 7407) to determine magnetic susceptibility and with a GE-MR 750 MRI at 3T as per the methods of Rohrer et al.<sup>42</sup> and Haedicke et al.<sup>43</sup>. Various amounts of UCNPs were prepared in a 1.5% agarose gel with TBE buffer to yield a Gd ion concentration of 0.133 to 5.337 mM. Vasovist, a commercially available Gd contrast agent, was used as comparison.<sup>44</sup>

#### **4.2.8 Cell viability**

Biocompatibility was assessed colorimetrically with a MTT cell viability Assay (Sigma-Aldrich) in triplicate incubated with 10, 50, 100, 250, and 300 µg/mL of the Gd-UCNP, Gd-antiVEGF UCNPs, and the anti-VEGF equivalent for 24 hours with 8, 000 cells. The anti-VEGF equivalent is the amount of anti-VEGF that should be bioconjugated onto the Gd-antiVEGF UCNPs.

#### **4.2.9 Immunocytochemistry**

8 chambered culture slides (Eppendorf) were groomed for ICC by coating them with a 2% solution (w/w) of gelatin (**Figure 4-4**). The 2% solution was made by dissolving the

gelatin into deionized water at 37°C then sterilized in an autoclave. Enough of the gelatin solution to cover the entirety of the well was added and left for 2 hours at 37°C to settle. The solution was then aspirated gently and the gelatin coated plates were left to dry overnight.

Approximately 100,000 cells were seeded into each well. To mimic angiogenesis, cells were treated with 50 µg/mL of phorbol 12-myristate 13-acetate (PMA) for 24 hours prior to treatment with 10 and 100 µg/mL of Gd UCNP, Gd-antiVEGF UCNP, and anti-VEGF equivalent for another 24 hours before ICC in triplicate. It is known PMA is capable of accelerating endothelial cell migration, vascular network formation, and its stabilization.<sup>45,46</sup>

HUVECs were fixed to the gelatin matrix with 4% formalin for 2 hours. Cells were permeabilized with a 0.1% Triton X-100 solution prepared with PBS for 5 minutes. TRITC-phalloidin prepared according to the manufacturer's instructions was incubated with the cells at room temperature for 40 min to stain the actin. DAPI, prepared as per the manufacturer's instructions was added to the cells for 15 minutes. In between each step, cells were thrice washed gently with PBS (pH 7.4). Cells were then treated with anti-fade and sealed with a cover slip for confocal imaging (Zeiss LSM510 Duo).

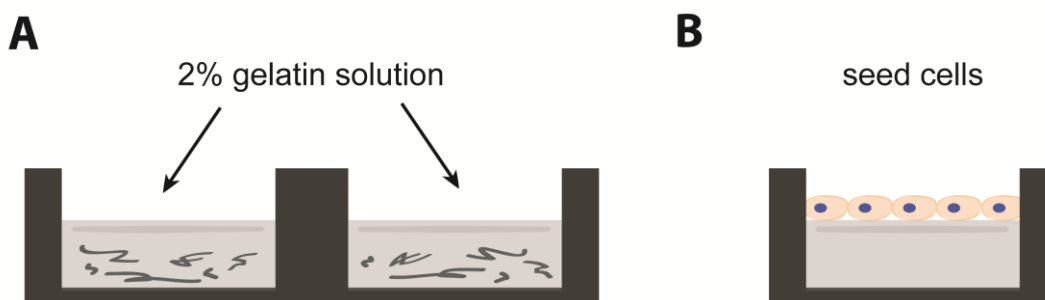


**Figure 4-4.** Chamber preparation for immunocytochemistry. A) 2% gelatin solution was loaded into the 8 well chambers for 2 hours at 37°C prior to aspiration and drying to form a growth matrix for the HUVECs. B) Cells were seeded into the sterile chambers in simulate angiogenic conditions with the addition of PMA.

Cell morphology was visualized and cell length was measured to verify angiogenesis and determine the anti-angiogenic effects of anti-VEGF. Furthermore, we determined the localization of the FITC tagged Gd-antiVEGF UCNP with respect to the cell structure to verify internalization and extracellular localization. Images were captured from at least 4 separate sections of each chamber such as  $n = 120$  cells from each treatment were documented. Image processing was performed with Image Pro Premier (Media Cybernetics Inc., Rockville, MD).

#### 4.2.10 Statistical Analysis

Statistical significance was determined using GraphPad Prism (GraphPad Software Inc, La Jolla, CA, USA). T test was used to assess UCNP size as a result of functionalization. Cell viability was assessed with a t test and two-way ANOVA to determine the effect of concentration. Changes in cell length and treatment concentration were assessed with a one-way ANOVA. Statistical analyses was performed at the 95% confidence level.

### 4.3 Results

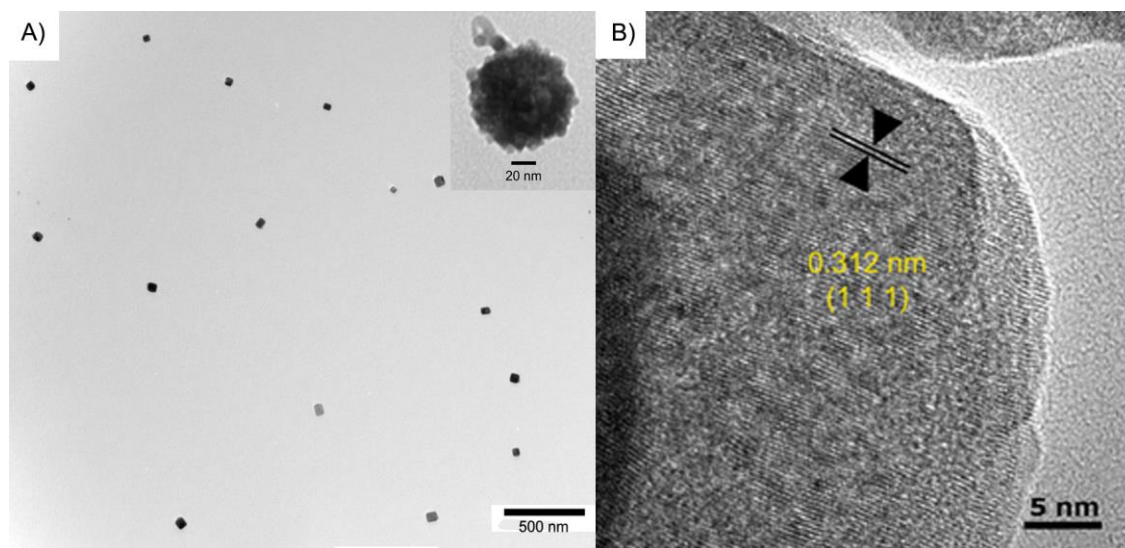


**Figure 4-5.** Upconversion antibody model characterization by TEM. A) Bare Gd-UCNP visualized by TEM. As shown in the inset, the anti-VEGF (outlined in red) was visualized on the Gd-antiVEGF UCNP. B) HRTEM shows the highly crystalline structure of the UCNP. The interplanar distance between adjacent lattice planes was 0.312 nm.

As shown in **Figure 4-5A**, the TEM images was able to visualize the bioconjugated anti-VEGF onto the Gd-UCNPs. HRTEM, **Figure 4-5B**, determined the interplanar distance between adjacent lattice planes to be 0.312 nm, which corresponds to a (1 1 1) plane of the NaGdF<sub>4</sub> (JCPDS 27-0697). PEI surface modification of the Gd-UCNPs was confirmed by FTIR, shown in **Figure 4-6**, demonstrates a broad peak at 3300 cm<sup>-1</sup> caused by -NH- stretching and a peak at 1510 cm<sup>-1</sup> resultant of the vibration of amine groups. UCNP size as a result of anti-VEGF functionalization and amount bioconjugated can be seen on **Table 4-1**. Anti-VEGF significantly increased the size of the UCNP from ~ 53 nm to ~ 106 nm ( $p < 0.0001$ ). Protein assay determined 9.48 μg of anti-VEGF was bioconjugated onto the surface of the 1 mg Gd-UCNP. Physical quantification by ICP-MS of the constituents Gd, Er, and Yb is reported in **Table 4-2**.

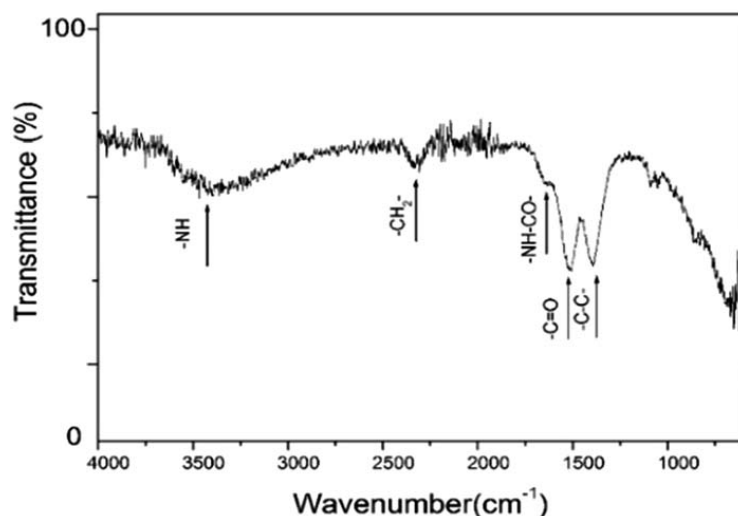


**Figure 4-6.** FTIR spectrum of the PEI modified NaGdF<sub>4</sub>: Er, Yb UCNPs. -NH- stretching was confirmed by the broad 3300 cm<sup>-1</sup> peak. -OC-NH- bending was demonstrated by the small 1640 cm<sup>-1</sup> peak. Amine groups were shown by the 1510 cm<sup>-1</sup> peak. The stretching vibrations of -CH<sub>2</sub>- and C-C bonds are visualized at 2300 and 1400 cm<sup>-1</sup> respectively.

**Table 4-1.** Physical characterization of Gd-UCNPs.

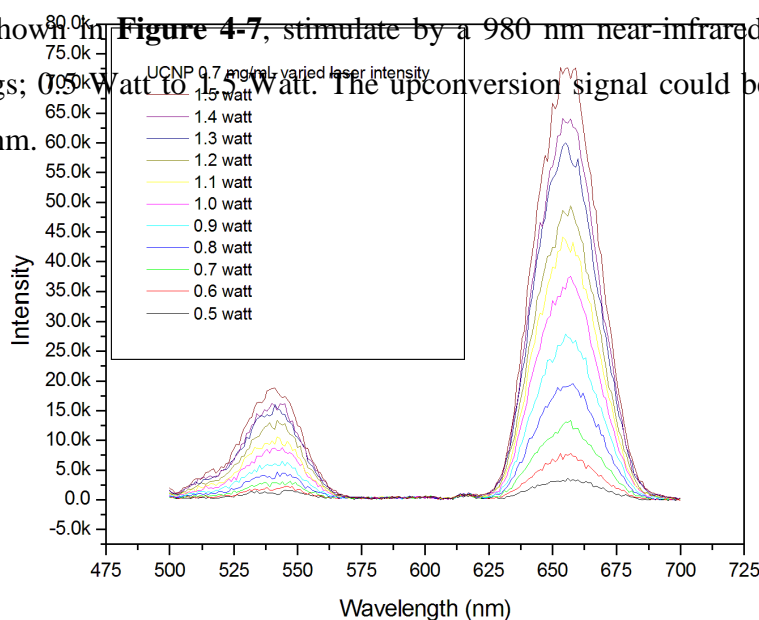
Parameter	Gd-UCNP	Gd-antiVEGF UCNP
Diameter (nm)	52.95 ± 12.98*	105.50 ± 35.28*
Anti-VEGF (μg/ mg Gd-UCNP)	N/A	9.48 ± 1.92

\*Significant increase on size was resultant of anti-VEGF bioconjugation ( $p < 0.0001$ ). Size was determined by measuring individual particles in TEM images ( $n = 200$ ).

**Table 4-2.** Percent composition of Gd, Er, and Yb in UCNPs

Sample	Composition (%)
Gd	41.97
Er	10.80
Yb	11.12

Upconversion fluorescence of the Gd-UCNPs was assessed at a concentration of 0.7 mg/mL, as shown in **Figure 4-7**, stimulate by a 980 nm near-infrared laser of various power settings; 0.5 Watt to 1.5 Watt. The upconversion signal could be detected at 660 nm and 540 nm.

**Figure 4-7.** Upconversion fluorescence spectra of the NaGdF<sub>4</sub>: Er, Yb UCNPs. Laser excitation of 980 nm at various powers 0.5 to 1.5 Watt.

Magnetization of the UCNPs was assessed by VSM. **Figure 4-8** depicts the magnetization of the UCNPs at various biological relevant temperatures to be paramagnetic. Furthermore, at an applied field of 1 T, the magnetization was determined to be 1.3 emu/g.

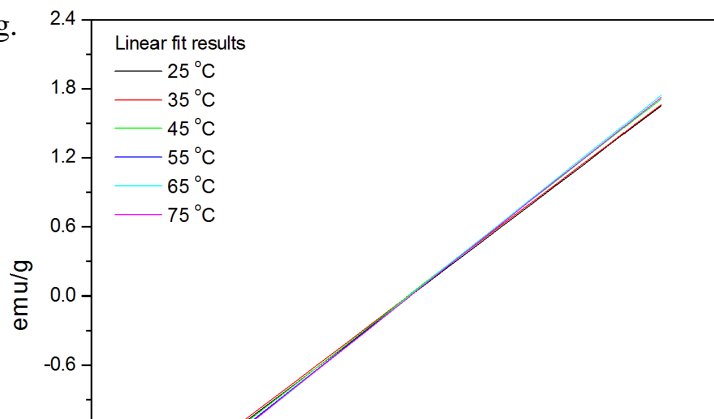




**Figure 4-8.** Magnetization of the UCNPs. At various biologically relevant temperatures, the magnetization was found to be approximately 1.3 emu/g and paramagnetic. Analysis of the UCNPs in a 3 T MRI using a fast spin echo-inversion recovery sequence with various inversion times for T1-weighted imaging is shown in **Figure 4-9**. Imaging parameters were as follows: inversion time (TI) = 200, 500, and 2000 ms; flip angle of 160°. Highlighted in red is the 1% Vasovist and water as references.

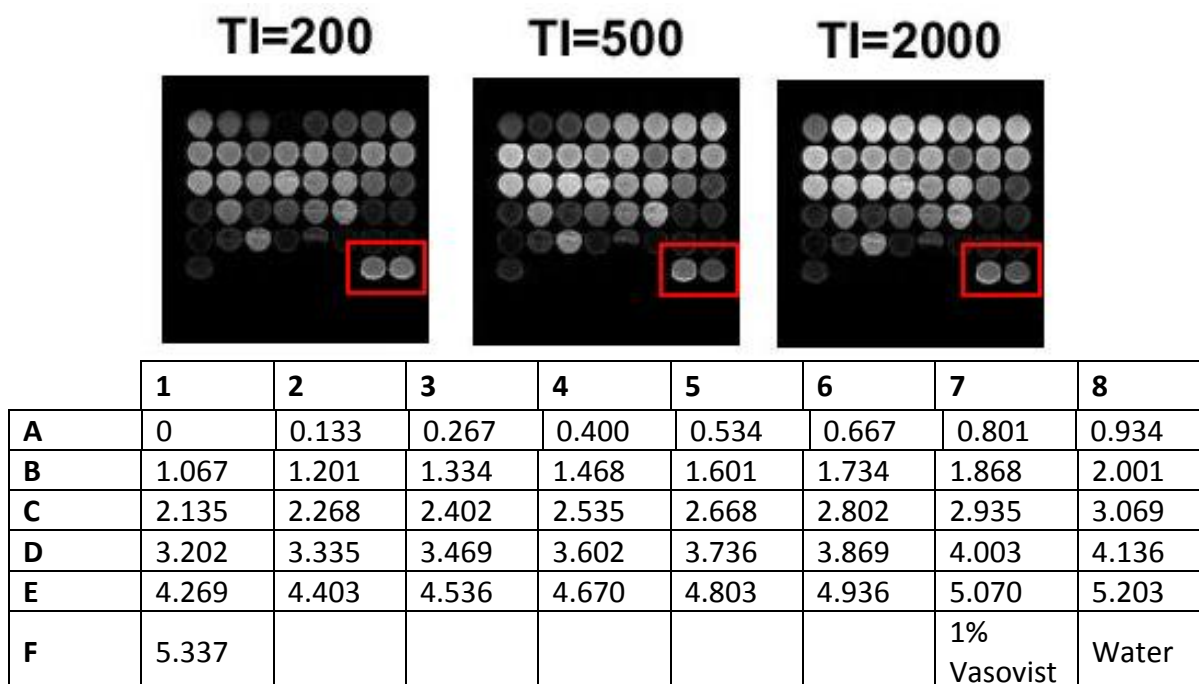


**Figure 4-9.** UCNP T1-weighted signal with 3 T magnetic field. Signal as a result of various inversion times (TI). Outlined in red are the references; 1% Vasovist and water respectively. Sample concentrations are listed in mM of Gd suspended in 1.5% agarose gel.

Relative cell viability of the HUVECs treated with Gd-UCNP, Gd-antiVEGF UCNP, and the anti-VEGF equivalent demonstrated significant difference in viability between Gd-UCNP and the anti-VEGF based treatments (**Figure 4-10A**;  $p < 0.05$ ). Relative viability of anti-VEGF based treatments decreased from 85% viability to below 70% viability when increasing concentration from 10  $\mu\text{g/mL}$  to 100  $\mu\text{g/mL}$ . Gd-UCNP demonstrated an increase in viability instead. Comparing the relative viability of Gd-UCNP to Gd-antiVEGF UCNP at concentrations of 50, 100, 250, and 300  $\mu\text{g/mL}$ , there was a significant decrease cell viability between the two samples (**Figure 4-10B**;  $p = 0.0114$ ). Gd-antiVEGF caused a significant decrease in viability to approximately 70% with increasing concentration whereas, Gd-UCNP remained above 80%.

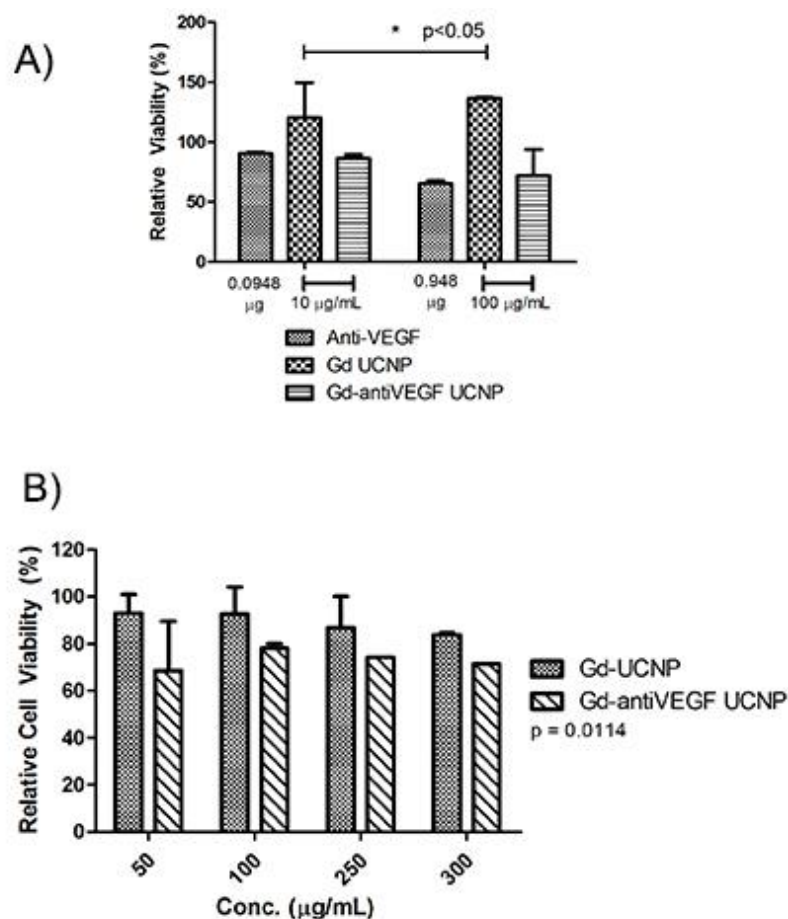


**Figure 4-10.** Relative cell viability of HUVECs with various treatments for 24 hours. A) Cell viability of treated with Gd-UCNP, Gd-antiVEGF UCNP, and anti-VEGF equivalent. UCNP exhibited a significantly higher viability compared to anti-VEGF based treatments ( $p < 0.05$ ). B) Gd-UCNP exhibited a significantly higher viability than Gd-antiVEGF UCNPs ( $p = 0.0114$ ).

**Figure 4-11** depicts the effect of anti-VEGF, Gd UCNP, and Gd-antiVEGF UCNP on HUVECs treated with PMA. Analysis indicated significant differences ( $p < 0.0001$ ) between the treatments. At the low concentration of  $10 \mu\text{g/mL}$ , the Gd-AntiVEGF UCNPs and anti-VEGF equivalent did not cause significant changes in cell lengths relative to the control, which was not treated with PMA. Cells treated with PMA and Gd-UCNPs exhibited significantly elongation though not significantly different to each other. In general, the anti-VEGF equivalent treatments and Gd-antiVEGF UCNPs exhibited shortened cell length in comparison to cells treated with just the Gd UCNPs.

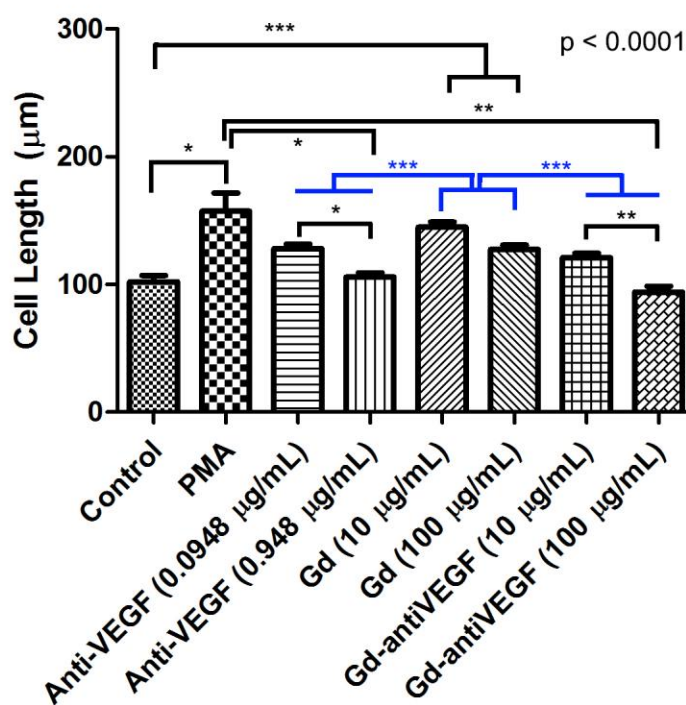


**Figure 4-11.** Change in cell length as a descriptor for angiogenesis. The cell length assessed indicated the anti-VEGF and Gd-antiVEGF UCNPs was significantly shorter than those treated with Gd UCNPs ( $p < 0.0001$ ) after incubation for 24 hours. PMA and Gd UCNPs were not significantly different in cell length but were significantly longer than the control cells.

HUVECs incubated with Gd-antiVEGF UCNP's tagged with FITC were processed into isoforms to provide a clear image of the fluorescence signal and displayed in **Figure 4-12**. The confocal fluorescent image of the HUVECs stained for the actin (red), cell nucleus (blue), and the Gd-antiVEGF UCNP's (green) is shown in **Figure 4-12A**. The corresponding isoform image in **Figure 4-12B**, presents a clearer and sharper image of the staining. As shown in **Figure 4-12C**, the magnified HUVEC is interacting with the Gd-antiVEGF UCNP's on the external surface. The z-stack image of the corresponding cell is shown in **Figure 4-12D**. The effect of the Gd-antiVEGF UCNP's (C) can be observed in **Figure 4-13** relative to the control (A) and the PMA treated cells (B). The cells treated with Gd-anti-VEGF exhibited less coordination and elongation in comparison.

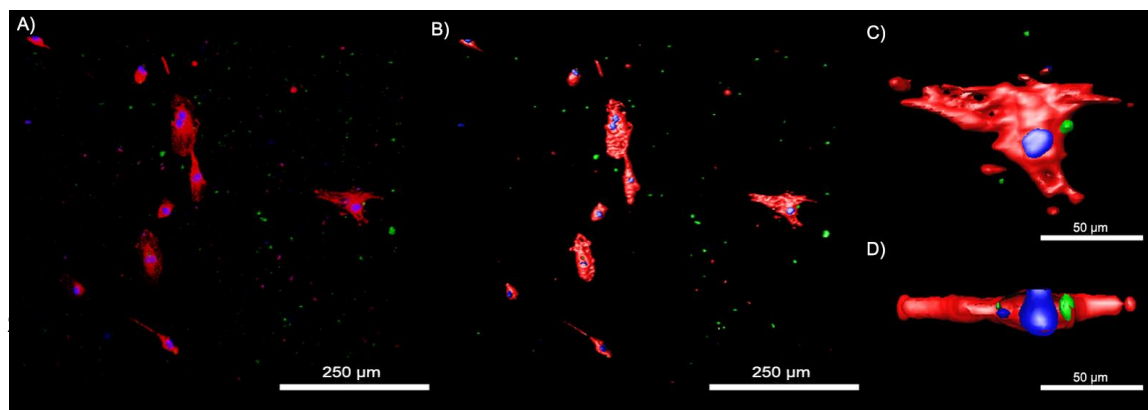


**Figure 4-12.** Confocal images of HUVECs treated with FITC tagged Gd-antiVEGF UCNP's. A) Confocal images depicting the stained actin (red), cell nucleus (blue) and FITC tagged Gd-antiVEGF UCNP's (green). B) Corresponding isoform image. C) Magnified isoform showing the cellular interaction of Gd-antiVEGF UCNP. D) Z-stack of an endothelial cells demonstrating the intracellular location of the Gd-antiVEGF UCNP relative to the nucleus.

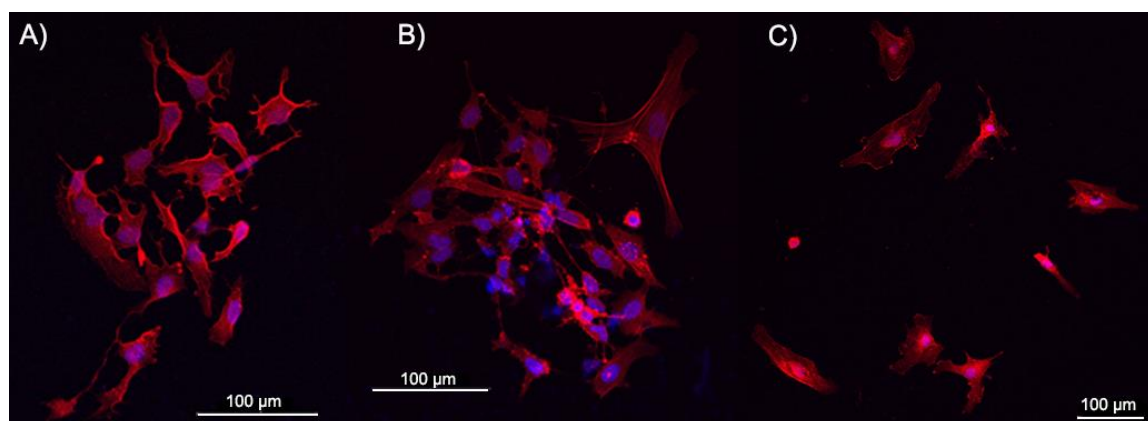


**Figure 4-13.** Confocal images of HUVEC cells. A) Control cells demonstrated some coordination. B) PMA treated HUVECs exhibited elongation and coordination into an immature vascular network C) Gd-antiVEGF UCNPs treated cells inhibited the elongation and formation of an immature vascular network.

## 4.4 Discussion

Our UCNPs functionalized with anti-VEGF provides insight into a shift from traditional treatment and imaging strategies to nanoparticle oriented technology. Our theranostic model was developed to be compatible for tracking by magnetic resonance imaging and fluorescent imaging with the purpose of counter acting pathological angiogenesis.

The bimodal tracking capabilities by MRI and fluorescence was studied by VSM, MRI, and spectrophotometrically with a NIR laser ( $\lambda_{\text{ex}} = 980 \text{ nm}$ ). With respect to upconversion fluorescent imaging as shown in **Figure 4-7**, the detected fluorescence was presented as a function of varying laser powers suitable for biomedical applications. The observed emission spectra was strongly affect by laser power as confirmed by Wang et al.<sup>37</sup> The fluorescence of the 0.7 mg/mL of UCNPs stimulated at low power (0.5 W) was observed to relatively weak. Furthermore, the upconversion nanoparticles has been demonstrated by various groups to demonstrate strong fluorescent emissions as a result of the multi-photon upconversion process.<sup>47,48</sup> Compatibility with MRI as displayed in **Figure 4-9**, demonstrates a potential to be employed as a tracking agent and contrast agent. Signal from Gd concentrations as low as 0.1 mM or lower have been detected.<sup>38,49</sup> In depth investigation of the lanthanide dopants concentration may provide an optimal ratio of the dopants to maximize either upconversion fluorescence or MR signal. However, it is possible to also increase or decrease the specific dopants to improve the detected signal of choice; Gd for MRI or Er/Yb for upconversion fluorescence.

Analysis of cell viability (**Figure 4-10A**) of the anti-VEGF equivalent, Gd UCNPs, and Gd-antiVEGF UCNPs demonstrated a viability of above 85% at a low concentration (10

$\mu\text{g/mL}$ ) and decreased at a higher concentration of anti-VEGF was introduced to the HUVECs causing a significant decrease in viability, which is reflective of the anti-angiogenic properties of the anti-VEGF. Assessment of the Gd UCNPs vs Gd-antiVEGF UCNPs viability over an increased range of concentrations (**Figure 4-10B**) also demonstrated the anti-VEGF's anti-angiogenic properties at elevated concentrations. As the MTT assay is a measure of viability, the anti-VEGF's ability to neutralize the VEGF signal is reflected by the decreased viability as they lose their proliferative stimulation.<sup>50,51</sup>

As **Figure 4-11** suggests, the lengthening and shortening of the cells is reflective of the angiogenic process as the cells proliferate and migrate to form novel vascular structures. The addition of PMA as shown by Osaki et al.<sup>45</sup> and Goodwin<sup>46</sup> is able to stimulate the formation of such structures. The addition of the anti-VEGF equivalent and Gd-antiVEGF UCNPs was able to significantly shorten the cells which signifies the inhibition of elongation; a characteristic of anti-angiogenesis. The effect can be observed in **Figure 4-13**. These results are reflective of the anti-VEGF treatments currently employed for treating AMD and cancer.<sup>8,13,16</sup>

Our theranostic model is promising as it is compatible with bimodal imaging for tracking and imaging for *in vivo* applications. As demonstrated by various groups, the bare UCNPs are capable of bimodal imaging with success *in vitro* and *in vivo* rodent models capable of accumulating with in tumours.<sup>49,52-54</sup> Our model was able to exhibit similar properties for bimodal imaging and provided anti-angiogenic effects in addition to that.

## 4.5 References

1. Lin, Y. *et al.* Apatinib for metastatic breast cancer in non-clinical trial setting : Satisfying efficacy regardless of previous anti-angiogenic treatment. *Tumor Biol.* **39**, 1–9 (2017).
2. Setyawati, M. I., Tay, C. Y., Bay, B. H. & Leong, D. T. Gold Nanoparticles Induced Endothelial Leakiness Depends on Particle Size and Endothelial Cell Origin. *ACS Nano* **11**, 5020–5030 (2017).
3. Elsaid, N., Jackson, T. L., Elsaid, Z., Alqathama, A. & Somavarapu, S. PLGA Microparticles Entrapping Chitosan-Based Nanoparticles for the Ocular Delivery of Ranibizumab. *Mol. P* **13**, 2923–2940 (2016).
4. Cabral, T. *et al.* Aqueous vascular endothelial growth factor and clinical outcomes correlation after single intravitreal injection of bevacizumab in patients with neovascular age - related macular degeneration. *Int. J. Retin. Vittr.* **3**, 4–11 (2017).
5. Ronca, R., Struyf, S., Benkheil, M., Liekens, S. & Mitola, S. Tumor angiogenesis revisited : Regulators and clinical implications. *Med. Res. Rev.* 1–44 (2017). doi:10.1002/med.21452
6. Rubanyi, G. M. *Angiogenesis in Health and Disease*. (CRC Press, 2000).
7. Meadows, K. L. & Hurwitz, H. I. Anti-VEGF Therapies in the Clinic. *Cold Spring Harb. Perspect. Med.* **2**, 1–27 (2012).
8. Makita, S. & Tobinai, K. Mogamulizumab for the treatment of T-cell lymphoma. *Expert Opin. Biol. Ther.* **17**, 1145–1153 (2017).
9. Ferrara, N. *Angiogenesis: From Basic Science to Clinical Applications*. (CRC Press, 2006).
10. Klagsbrun, M. & D'Amore, P. A. *Angiogenesis – Biology and Pathology*. (Cold Spring Harbor Laboratory Press, 2011).

11. Kovach, J. L. *et al.* Anti-VEGF Treatment Strategies for Wet AMD. *J. Ophthalmology* **2012**, 1–7 (2012).
12. Birch, D. G. Age-related macular degeneration: a target for nanotechnology derived medicines. *Int. J. Nanomedicine* **2**, 65–77 (2007).
13. Bloch, S. B. Implementation studies of ranibizumab for neovascular age-related macular degeneration. *Acta Ophthalmol.* **92**, 98 (2014).
14. Lu, X. & Sun, X. Profile of conbercept in the treatment of neovascular age-related macular degeneration. *Drug Des. Devel. Ther.* **9**, 2311–2320 (2015).
15. Hashemi, S., Faramarzi, M. A., Ghasemi Falavarjani, K. & Abdollahi, M. Bevacizumab for choroidal neovascularization secondary to age-related macular degeneration and pathological myopia. *Expert Opin. Biol. Ther.* **14**, 1837–1848 (2014).
16. Miyamoto, N., Kojima, H. & Shimozone, M. Response of eyes with age-related macular degeneration to anti-VEGF drugs and implications for therapy planning. *Clin. Ophthalmology* **11**, 809–816 (2017).
17. Santarelli, M. *et al.* Advances in pharmacotherapy for wet age-related macular degeneration. *Expert Opin. Pharmacother.* **16**, 1769–1781 (2015).
18. Wicki, A., Witzigmann, D., Balasubramanian, V. & Huwyler, J. Nanomedicine in cancer therapy: Challenges, opportunities, and clinical applications. *J. Control. Release* **200**, 138–157 (2015).
19. Mahor, A. *et al.* Journal of Colloid and Interface Science Moxifloxacin loaded gelatin nanoparticles for ocular delivery: Formulation and in - vitro , in - vivo evaluation. *J. Colloid Interface Sci.* **483**, 132–138 (2016).
20. Ding, C. & Li, Z. A review of drug release mechanisms from nanocarrier systems. *Mater. Sci. Eng. C* **76**, 1440–1453 (2017).



21. Suk, J. S., Xu, Q., Kim, N., Hanes, J. & Ensign, L. M. PEGylation as a strategy for improving nanoparticle-based drug and gene delivery. *Adv. Drug Deliv. Rev.* **99**, 28–51 (2016).
22. Choi, K. Y., Liu, G., Lee, S. & Chen, X. Theranostic nanoplatfoms for simultaneous cancer imaging and therapy: current approaches and future perspectives. *Nanoscale* **4**, 330 (2012).
23. Gahlaut, N. *et al.* Nanoengineering of therapeutics for retinal vascular disease. *Eur. J. Pharm. Biopharm.* **95**, 323–330 (2015).
24. Xie, J., Lee, S. & Chen, X. Nanoparticle-based theranostic agents. *Adv. Drug Deliv. Rev.* **62**, 1–32 (2010).
25. Seleci, M., Seleci, D. A., Jonczyk, R., Stahl, F. & Blume, C. Smart multifunctional nanoparticles in nanomedicine. *Bionanomaterials* **17**, 33–41 (2016).
26. Mohanraj, V. J. & Chen, Y. Nanoparticles – A Review. *Trop. J. Pharm. Res.* **5**, 561–573 (2006).
27. Kumari, A., Yadav, S. K. & Yadav, S. C. Biodegradable polymeric nanoparticles based drug delivery systems. *Colloids Surfaces B Biointerfaces* **75**, 1–18 (2010).
28. Xu, Y. & Du, Y. Effect of molecular structure of chitosan on protein delivery properties of chitosan nanoparticles. *Int. J. Pharm.* **250**, 215–226 (2003).
29. Tarhini, M., Greige-gerges, H. & Elaissari, A. Protein-based nanoparticles : From preparation to encapsulation of active molecules. *Int. J. Pharm.* **522**, 172–197 (2017).
30. Zheng, Q. & Lavis, L. D. Development of photostable fluorophores for molecular imaging. *Curr. Opin. Chem. Biol.* **39**, 32–38 (2017).
31. Ge, J. *et al.* Standard Fluorescent Imaging of Live Cells is Highly Genotoxic. *Cytometry A* **83**, 552–560 (2014).

32. Schulz, R. B. & Semmler, W. in *Molecular Imaging I* (ed. Wolfhard Semmler, M. S.) 3–23 (Springer-Verlag Berlin Heidelberg, 2008).
33. Chen, L., Tse, W. H., Siemiarczuk, A. & Zhang, J. Special properties of luminescent magnetic NaGdF<sub>4</sub>:Yb<sup>3+</sup>, Er<sup>3+</sup> upconversion nanocubes with surface modifications. *RSC Adv.* **7**, 26770–26775 (2017).
34. Holmberg, R. J., Aharen, T. & Murugesu, M. Paramagnetic Nanocrystals: Remarkable Lanthanide-Doped Nanoparticles with Varied Shape, Size, and Composition. *J. Phys. Chem. Lett.* (2012).
35. Hou, Y. *et al.* NaGdF<sub>4</sub> Nanoparticle-Based Molecular Probes for Magnetic Resonance Imaging of Intraperitoneal Tumor Xenografts in Vivo. *ACS Nano* **7**, 330–338 (2013).
36. Wong, H. T. *et al.* In vitro cell imaging using multifunctional small sized KGdF<sub>4</sub>:Yb<sup>3+</sup>,Er<sup>3+</sup> upconverting nanoparticles synthesized by a one-pot solvothermal process. *Nanoscale* **5**, 3465–3473 (2013).
37. Wang, F., Deng, R. & Liu, X. Preparation of core-shell NaGdF<sub>4</sub> nanoparticles doped with luminescent lanthanide ions to be used as upconversion-based probes. *Nat. Protoc.* **9**, 1634–1644 (2014).
38. Zhou, J. *et al.* Dual-modality in vivo imaging using rare-earth nanocrystals with near-infrared to near-infrared ( NIR-to-NIR ) upconversion luminescence and magnetic resonance properties. *Biomaterials* **31**, 3287–3295 (2010).
39. Zhao, P. *et al.* NIR-driven Smart Theranostic Nanomedicine for On-demand Drug Release and Synergistic Antitumour Therapy. *Sci. Rep.* **5**, 14258 (2015).
40. Hong, G., Antaris, A. L. & Dai, H. Near-infrared fluorophores for biomedical imaging. *Nat. Biomed. Eng.* **1**, 1–22 (2017).
41. Kwon, O. S., Song, H. S., Kim, H., Artzi, N. & Kim, J. Dual-Color Emissive Upconversion Nanocapsules for Differential Cancer Bioimaging In Vivo. (2016).

42. Rohrer, M., Bauer, H., Mintorovitch, J., Requardt, M. & Weinmann, H. J. Comparison of Magnetic Properties of MRI Contrast Media Solutions at Different Magnetic Field Strengths. *Invest. Radiol.* **40**, 715–724 (2005).
43. Haedicke, I. E. *et al.* An enzyme-activatable and cell-permeable MnIII-porphyrin as a highly efficient T1 MRI contrast agent for cell labeling. *Chem. Sci.* **7**, 4308–4317 (2016).
44. Sabach, A. S. *et al.* Gadofosveset trisodium: Abdominal and peripheral vascular applications. *Am. J. Roentgenol.* **200**, 1378–1386 (2013).
45. Osaki, T. *et al.* Acceleration of vascular sprouting from fabricated perfusable vascular-like structures. *PLoS One* **10**, 1–14 (2015).
46. Goodwin, A. M. *n vitro* assays of angiogenesis for assessment of angiogenic and anti-angiogenic agents. *Microvasc. Res.* **74**, 172–183 (2009).
47. Ai, F. *et al.* A core-shell-shell nanoplatform upconverting near-infrared light at 808 nm for luminescence imaging and photodynamic therapy of cancer. *Sci. Rep.* **5**, 1–11 (2015).
48. Xu, C. T. *et al.* Upconverting nanoparticles for pre-clinical diffuse optical imaging, microscopy and sensing: Current trends and future challenges. *Laser Photonics Rev.* **7**, 663–697 (2013).
49. Zhou, L., Zheng, X., Gu, Z., Yin, W. & Zhang, X. Biomaterials for targeted drug delivery and multimodal imaging. *Biomaterials* **35**, 7666–7678 (2014).
50. Sene, A., Chin-Yee, D. & Apte, R. S. Seeing through VEGF: Innate and adaptive immunity in pathological angiogenesis in the eye. *Trends Mol. Med.* **21**, 43–51 (2015).
51. Campochiaro, P. A. Molecular pathogenesis of retinal and choroidal vascular diseases. *Prog. Retin. Eye Res.* **49**, 67–81 (2015).

52. Zhou, J. *et al.* Dual-modality in vivo imaging using rare-earth nanocrystals with near-infrared to near-infrared (NIR-to-NIR) upconversion luminescence and magnetic resonance properties. *Biomaterials* **31**, 3287–3295 (2010).
53. Hou, Y. *et al.* NaGdF<sub>4</sub> Nanoparticle-Based Molecular Probes for Magnetic Resonance Imaging of Intraperitoneal Tumor Xenografts in Vivo. *ACS Nano* 330–338 (2013).
54. Zhang, L. *et al.* Biomaterials Inorganic photosensitizer coupled Gd-based upconversion luminescent nanocomposites for in vivo magnetic resonance imaging and near-infrared-responsive photodynamic therapy in cancers. *Biomaterials* **44**, 82–90 (2015).

## CHAPTER 5

*To quantitatively assess our biosensor for detecting glucose with high sensitivity and low concentration in tears from rats. The QD-based biosensor aims to non-invasively assess tear glucose as a reflection of blood glucose using Forster Resonance Energy Transfer which is also known as Fluorescence Resonance Energy Transfer. The interaction between protein and QDs is vital to the optimal performance of the biosensor.*

*The contents of this chapter was previously published in the Biosensors and Bioelectronics: L. Chen\*, W.H. Tse\*, Y. Chen, M.W. McDonald, J. Melling and J. Zhang. Nanostructured biosensor for detecting glucose in tear by applying fluorescence resonance energy transfer quenching mechanism. Biosensors and Bioelectronics. 2017: 91;393-399. doi: dx.doi.org/10.1016/j.bios.2016.12.044.*

*\*authors contributed equally*

## **5 NANOSTRUCTURED BIOSENSOR FOR DETECTING GLUCOSE IN TEAR BY APPLYING FLUORESCENCE RESONANCE ENERGY TRANSFER QUENCHING MECHANISM.**

### **5.1 Introduction**

Tear fluid cleans and lubricates the eye while nourishing. Over 20 components have been found in tears, including salt water, proteins, glucose, and some small metallic ions, etc.<sup>1</sup> Diagnosis of biomolecules in tear fluid pertaining to ocular diseases such as ocular rosacea, have been performed primarily by clinicians to examine the high molecular-mass glycoproteins in tears.<sup>2</sup> The detection of ocular glucose dates back to 1930.<sup>3</sup> Following that, Michail and his collaborators first demonstrated the level of glucose in tears is often elevated in diabetic patients.<sup>4</sup> Sen and Sarin studied over 200 cases, their statistic results indicated the blood glucose is about 2 times higher in diabetic patients than that in non-diabetics, whereas tear glucose levels are ~5 times higher in diabetics than that in the general population.<sup>5</sup> In past decades, different research groups found a definite relationship between tear glucose and blood glucose, concluding hyperglycemia could be

detected by measuring tear glucose levels.<sup>6-8</sup> Recent studies indicate tear glucose mean values were  $0.35 \pm 0.04$  mmol/L and  $0.16 \pm 0.03$  mmol/L, for patients with diabetes and healthy subjects, respectively.<sup>9</sup> It is also noted time lag in measuring tear glucose is common to other glucose meters as it takes 5–15 min to allow the change of glucose in blood to eventually reflect in tear/interstitial fluids;<sup>10</sup> while it can be solved by a series of calibrations.<sup>11,12</sup>

However, it is very difficult to acquire enough tear samples in a short period. Furthermore, the concentration of glucose in tears is much lower than that in blood. Very few methods so far can measure such low concentration of glucose in a rapid fashion.<sup>13,14</sup> Compared to many other techniques, Forster or fluorescence resonance energy transfer (FRET), an inexpensive and very sensitive method, has been used in molecule imaging and glucose test.<sup>15-17</sup> It is a distance-dependent energy transfer from a fluorophore donor (D) to a fluorophore acceptor (A) in a nonradioactive process. When the distance of the two fluorophores is very close ( $< 10$  nm), the excited D will transfer some of its energy to excite A that then emits light at a longer wavelength.<sup>17</sup> Using FRET technique for detecting the competitive reactions of glucose and other polysaccharide, such as dextran, to concanavalin A (Con A), a protein, may result in accurate and convenient measures.<sup>18-20</sup> However, fluorophores/organic dyes used in FRET pair are subject to low fluorescent intensity, and poor signal responses influenced by the decay of chromophores and external environment.<sup>21</sup> Fluorescence nanostructures have been recognized as excellent materials used in FRET sensor due to their photo-stability and narrow emission peaks.<sup>22</sup> We developed a nanostructured sensor by using fluorescence resonance energy transfer (FRET) technique which is able to be incorporated into hydrogel-based contact lenses for measuring low concentration of glucose directly.<sup>23,24</sup> While, most reported FRET sensors have an inversely proportional relationship between the ratio of the fluorescence intensity of the donor to that of the acceptor ( $I_D/I_A$ ) and the amount of the targeted molecules because the rate constant of the energy transfer,  $k_{\text{FRET}}$ , decreases while the distance between the FRET pair increases. Consequently, most reported FRET sensors have significant measurement errors when detecting the increase of concentration of the targeted molecules because of the low fluorescence signals-to-noise ratio.

Quite recently, fluorescent quenching-based assay in which the donor fluorescence can be quenched by the acceptor without analytes has shown significant advantages in biosensing, as it allows the restored fluorescence signal proportional response to the concentration of target analytes and lower background fluorescence.<sup>15,25</sup> Consequently, a new nanostructured sensor by applying FRET quenching mechanism is developed here to detect small concentration of tear glucose from very small volume of tear samples in a fast and accurate fashion.

**Figure 5-1A** displays a FRET pair-labeled Concanavalin A (Con A), an enzyme with specific affinity to glucose.<sup>18-20</sup> The donor in this designed FRET transducer is made of quantum dots with an emission ( $\lambda_{em}$ ) in the visible range; the acceptor is dextran-bound malachite green (MG) which has an absorption at the same wavelength of the emission of the quantum dots. The emitted fluorescence of the quantum dots can be quenched by malachite green through the FRET mechanism. In the presence of glucose, the binding between Con A and dextran is out competed by the affinity of Con A for glucose. As a result, dextran bound MG will not quench the fluorescence of quantum dots, and therefore fluorescence intensity is restored. The change in fluorescence intensity is correlated to the amount of glucose reacting with Con A.

In addition, we would like to further develop a dual-method for detecting glucose through both of fluorescence spectra and fluorescence images. To quickly and accurately detect the amount of glucose in a very small volume of tear sample by measuring the changes of fluorescence intensity of the sensor, the numerous nanostructured FRET sensors are immobilized on a single ZnO nanorod (NR) which have a high surface area to volume ratio as shown in **Figure 5-1B**. This design allows numerous FRET biosensors located at a nanoscale, and therefore, is able to amplify the resolution of the sensor.<sup>26</sup> Moreover, to quickly and accurately detect the amount of glucose in a very small volume of tear sample by fluorescence images, the designed pattern made of ZnO NR array is utilized here which can be recognized easily through fluorescence image process. The pixel intensity values in a taken fluorescence image corresponding to the concentration of glucose can be calculated through an imaging process. Consequently, the patterned nanostructured FRET sensor on silicone hydrogel can realize the dual modulation for

monitoring glucose level in tear samples through both of fluorescence spectrum and calibrated image pixel value.

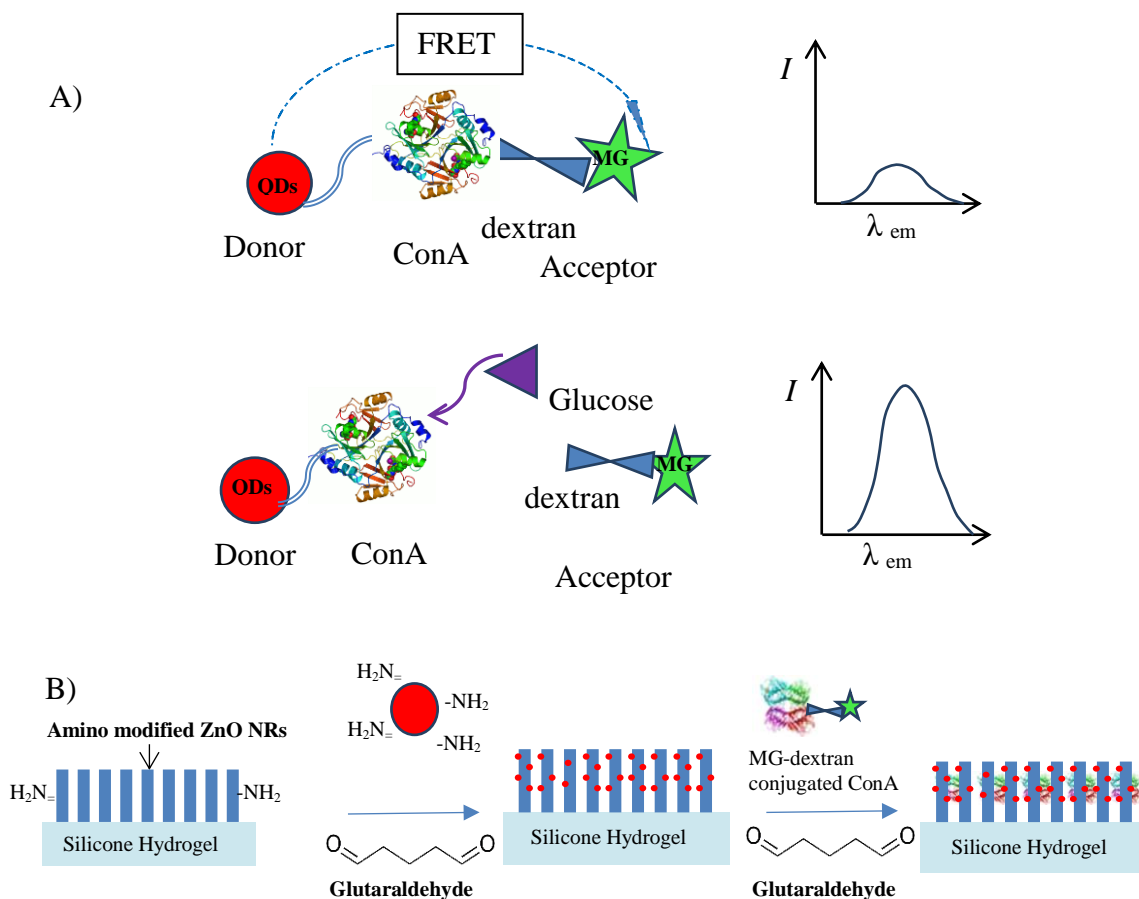


**Figure 5-1.** Illustration of the designed FRET transducer made of ConA-conjugating quantum dots (donor) and MG (acceptor) for detecting glucose. Competitive affinity for glucose displaces MG to restore the quenched fluorescence. (b) Immobilization of the nanostructured FRET transducers on ZnO nanorod array deposited on silicone hydrogel.

## 5.2 Materials and Methods

### 5.2.1 Study Design

The glucose sensor was designed and optimized for low sensitivity detection of glucose change on ZnO nanorods grown on a silicone substrate. The sensor was designed for a quenching mechanism to detect glucose as low as 0.03 mM and up to 3 mM where an



increase in glucose concentration linearly correlated with an increase in detectable fluorescent intensity.

Glucose sensor effectiveness was assessed on Sprague-Dawley rats (Charles River Laboratories, St. Constant, Quebec, Canada) with induced diabetes. Tear glucose collected with capillary tubes and quantified with our fluorescent glucose sensor was compared and contrasted to blood glucose measured with a glucose meter (Freestyle Lite Blood Glucose Monitoring System, Abbott Diabetes Care Inc., Mississauga, Ontario).

Our substrate-based glucose sensor's fluorescence was assessed and captured with a handheld USB powered portable digital microscope, MiScope, from Zorbaco. Images were processed in Matlab to determine the relationship between fluorescence intensity and glucose concentration in the samples.

### **5.2.2 Fabrication of patterned QDs decorated with ZnO nanorod arrays on silicone**

Hydrogel Cadmium selenium/zinc sulfide (CdSe/ZnS) core-shell quantum dots (QDs) were chosen as the donor of the FRET pair. The core-shell QDs were further functionalized with amine groups.<sup>27</sup> Briefly, CdSe/ZnS (20 mg) dissolved in 3 mL of chloroform was mixed with a solution of cysteamine (Cys) hydrochloride (100 mg) dissolved in 5 mL of water. The solution was sonicated until the chloroform layer became clear. The remaining cysteamine was reacted with the addition in excess of 2-mercaptoethanol (20 mmol/L). CdSe/ZnS/Cys QDs were purified by threefold centrifugation (15 min at 10000 rpm) and rinsed with ethanol. Purified particles were re-dispersed in water.

Silicone hydrogel with 150  $\mu\text{m}$  in thickness was produced using a photochemical process.<sup>28</sup> The patterned ZnO nanorod (NR) array was fabricated on the silicone hydrogel by a photolithographic lift-off process as visualized in Figure 5-2. Photoresist (PR; Shipley 1827) was deposited on the ZnO NR arrays by spin coating and exposed to UV (Karl Suss MJB3, Hg Arc Lamp) irradiation over a patterned photomask for 30 seconds followed with post-baking. After the post-baking, the non-irradiated area was treated with a developer (Shipley Microposit MF-319) for 2 min and rinsed with DI water. A wet

chemical etching method was used to remove the ZnO area without PR by immersion in a diluted acetic acid solution. After washing with DI water, the remaining PR was washed away using ethanol. The final products were dried for further application.

The surface modification of the patterned ZnO NR array with amino groups is described as follows; the ZnO NR array on silicone hydrogel was immersed into 2 mL DMSO and 270  $\mu$ L 3-aminopropyltriethoxysilane (APS) suspension. After having reacted at 120  $^{\circ}$ C for 2 h, the ZnO hydrogel was taken out and washed with ethanol to remove unreacted compounds.<sup>29,30</sup> Please note that a small corner of the ZnO NR array on silicone hydrogel was not modified by 3-APS for further conjugation of the FRET pair which will be used as a control area for imaging analysis.

Prior to coating QDs-based FRET sensor onto the surface of lithographically patterned ZnO NRs, glutaraldehyde first reacted with amino group modified ZnO NRs. Following that, ZnO NRs array on silicone hydrogel merged in a 20 mL CdSe solution for 3 days at 4  $^{\circ}$ C, then washed with DI water to remove excess glutaraldehyde and CdSe/ZnS QDs. The obtained film was dried in the dark under vacuum to preserve sensing capabilities.

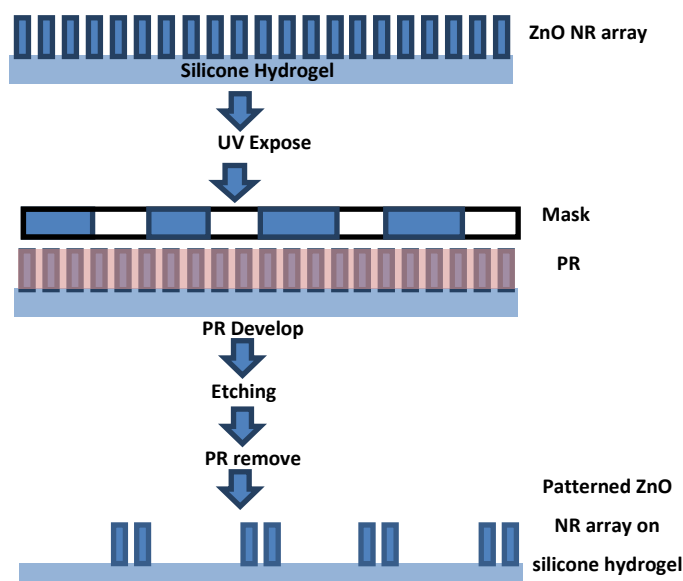


**Figure 5-2.** A photolithographic lift-off process for fabricating the patterned ZnO nanorod array on silicone hydrogel.

### 5.2.3 Synthesis of Malachite Green Dextran

Malachite green (MG) isothiocyanate and 70,000 MW amino dextran purchased from Life Technologies (Burlington, Ontario, Canada) were mixed in a 0.05 M sodium bicarbonate buffer at pH 9.6.<sup>31</sup> Successful conjugation of the isothiocyanate and dextran to form MG-dextran was verified by thin layer chromatography as shown in **Figure 5-3**. Concentration of MG-dextran ( $\epsilon=10^5 \text{ M}^{-1} \text{ cm}^{-1}$  for malachite green at 621 nm) was determined by UV/Vis using the Beer-Lambert Law.

#### Equation 5-1

$$A = \epsilon lc$$

Where A is the absorbance,  $\epsilon$  the molar absorptivity, l the path length, and c the concentration (mol/L).

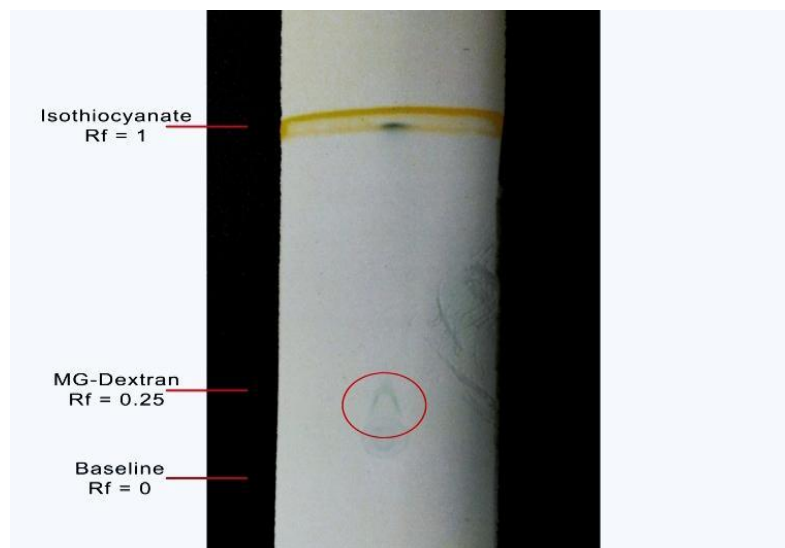


**Figure 5-3.** Thin layer chromatography confirmation of MG-dextran conjugation. The isothiocyanate and MG-dextran had a Rf value of approximately 1.0 and less than 0.25, respectively.

### 5.2.4 Synthesis and Optimization of the FRET Sensor

Con A protein was first loaded with MG-dextran at a molar ratio of 4:1 MG-dextran to Con A in water and agitated for 2 hours. Following that, glutaraldehyde was added to the

above solution at 1:1 molar ratio and agitated for another 2 hours. QDs were then added and agitated for a further 2 hours. To ensure maximum sensitivity in the presence of glucose, CdSe/ZnS quantum dots (QD) were conjugated to Con A loaded with MG-dextran at weight ratios of 10:1, 5:1, 3:1, 2:1, and 1:1, respectively, to determine the degree of quenching and when an increase in QD weight becomes negligible to the change in fluorescence **Figure 5-4**. In this study, the optimal weight ratio of the donor (QDs) to enzyme (Con A) bonded with the acceptor (MG-dextran) was determined to be 7:1 and was used throughout the study.

In assembling the FRET sensor on ZnO silicone hydrogels, the dropwise application of Con A bonded with MG-dextran to the surface of QDs-decorated ZnO NRs with the aid of glutaraldehyde.

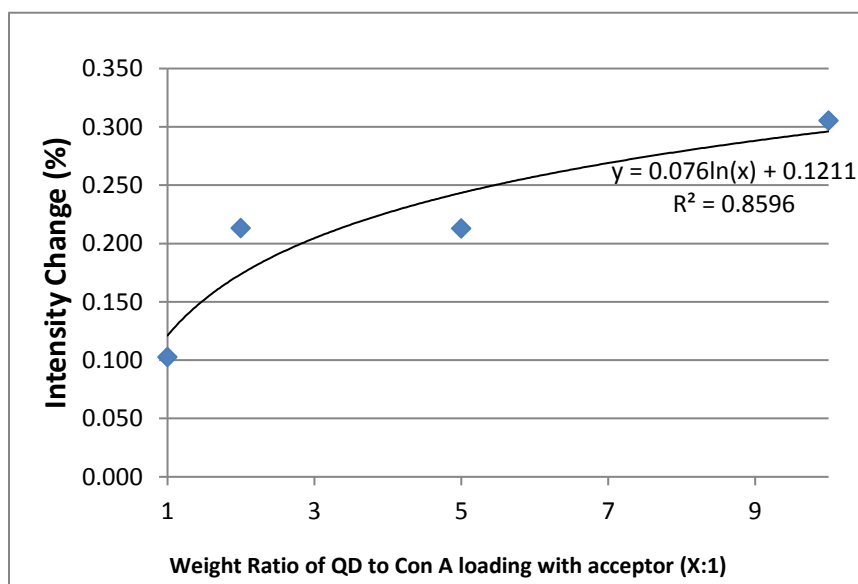


**Figure 5-4.** FRET signal optimization. Fluorescence intensity vs the weight ratio of QDs to Con A loaded with MG-dextran.

### 5.2.5 Sensor measurement

10  $\mu\text{L}$  of glucose in different concentrations at  $\text{pH} = 7.0$ , 0.03 mmol/L, 0.05 mmol/L, 0.2 mmol/L, 0.75 mmol/L, 1 mmol/L, 2 mmol/L, 3 mmol/L, were dropped on the patterned FRET sensors on silicone hydrogels with 30 s of interacting time. The fluorescence response of the patterned FRET sensors on silicone hydrogels to different concentrations of aqueous glucose were recorded by the fluorospectrometer with  $\lambda_{\text{em}} = 490$  nm. At least five independent measures were conducted to measure the response of the sensor according to each glucose level. The standard deviation for each measured points was also calculated.

### 5.2.6 Fluorescence sensor signal converting to image pixel intensity

The USB powered portable MiScope, (40X, pixels =  $640 \times 480$ ), was used to measure and digitally capture the fluorescence intensity of the 0.5 mg of glucose sensor conjugated onto ZnO NRs. 10  $\mu\text{L}$  of various concentrations of glucose was added; 0.03, 0.05, 0.2, 0.75, 1, 2, and 3 mmol/L. Glucose was allowed to react with the sensor for 5 min prior to fluorescent measurement. The donor molecule was excited with the UV light built into the MiScope.

The captured images were converted to RGB colours using Matlab as our previous reported results.<sup>24</sup> Both green and red channels were applied to record the pixel intensity pixel values. The values of pixel intensity of the patterned sensors responding to glucose amounts were calculated in comparison with that of the control areas where no FRET pair is conjugated. The recorded fluorescence images taken by the handheld fluorescence microscope can be converted to the value of pixel intensity through Matlab's imaging process. In this imaging conversion process, the image matrix of the control area were used to compare with that of sensing area of the FRET sensor to obtain the value of pixels intensity corresponding to the concentration of glucose.

The captured FRET sensing image with pixels  $\Sigma XY$  is calibrated in comparison with the image of the control area (lowest fluorescence signal from substrate) with pixels  $\Sigma X'Y'$ . The calibrated pixel intensity ( $I_p$ ) generated from FRET sensors can be expressed as follows;

**Equation 5-2**

$$I_p = \Sigma I(X_i Y_i) - \Sigma I(X_i' Y_i'),$$

Where,  $i$  is the number of pixels in the chosen areas.

**5.2.7 Animal tear test**

Following the positive results of cytotoxicity (**Figure 5-5**), we conducted the animal test to evaluate the response of designed sensor to tear glucose. Four male Sprague-Dawley rats (Charles River Laboratories, St. Constant, QC, Canada) were housed in a 12-h light/dark cycle room with humidity (50%) and temperature (21.5 °C) kept constant. Rats were given water and chow ad libitum and made diabetic with streptozotocin (STZ; Sigma-Aldrich, Oakville, ON, Canada). Intraperitoneal injections of STZ (20 mg/kg) dissolved in a citrate buffer (0.1 M, pH 4.5) were given over five consecutive days. Following the confirmation of diabetes (two blood glucose readings greater than 18 mmol/L) subcutaneous insulin pellets were implanted in the abdominal region of rats. Rats were anesthetized with isoflurane for ease of application of the sensors to their eyes. Tear fluid was collected from the ocular surface with a 1  $\mu$ L glass capillary tube (P1424 SIGMA). 2  $\mu$ L of rat tear sample were collected from each male Sprague-Dawley rats. All samples were diluted by PBS with pH = 7.0 to 7  $\mu$ L. Diluted tear samples (2  $\mu$ L) were then dropped on the FRET sensors (with five independent measures). The standard deviation for each measured points was also calculated. Fluorospectrometry was used to measure the fluorescence intensity of quantum dots (donor) after tear samples interact with FRET sensor for 30 secs. A blood sample was taken from the saphenous vein concurrently with the application of the sensor for blood glucose concentration (Freestyle Lite Blood Glucose Monitoring System, Abbott Diabetes Care Inc., Mississauga, Ontario).

Ethics approval was obtained through the University of Western Ontario Research Ethics Board, in accordance with Canadian Council on Animal Care guidelines.

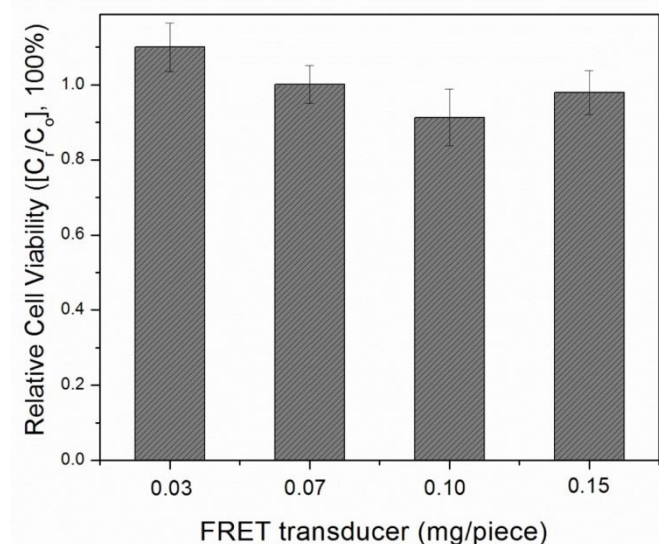


**Figure 5-5.** Cell viability of the FRET glucose sensor. Relative cell viability after 24 hour incubation with various sized FRET sensor modified onto the silicone substrate.

Cellular viability of the glucose sensor was conducted in the Lab of Dr. David Litchfield in the Department of Biochemistry of the University of Western Ontario. UTA-06 human osteosarcoma cells were used in this work, which were derived from the human osteosarcoma cell line U2-OS. The cell line was a generous gift from Dr. Christoph Englert, Forschungszentrum Karlsruhe, Germany.

UTA-06 cells were cultured and grown under sterile conditions in Dulbecco's Modified Eagle Medium (DMEM) supplemented with 10% FBS and 100 units/mL penicillin and 100  $\mu$ g/mL streptomycin, kept at 37°C with 5% CO<sub>2</sub>. 250 000 cells were transferred into each well of a 24 well culture plate and incubated overnight to ensure adhesion to the plate. Various amounts of patterned nanostructured FRET sensors (QDs-based FERT sensors assembled on ZnO NRs), i.e. 0.03, 0.07, 0.10, 0.15 mg, deposited on the surface of silicone hydrogels with dimensions 1cm  $\times$  1cm. Samples were sterilized under UV for 10 minutes.

In quadruplicate, the UTA-06 cells were cultured with the above sensors deposited on hydrogel samples for 24 hours. After the incubation period, the sensor samples were removed, and a MTT cell viability assay was performed. The absorbance of the plates was measured at  $\lambda_{em}$  =490 nm, and the relative cellular viability was calculated.

### 5.2.8 Statistical Analysis

Statistical significance was determined using GraphPad Prism (GraphPad Software Inc, La Jolla, CA, USA). Linear regressions were assessed. Statistical analysis of cytotoxicity was performed at the 95% confidence level.

## 5.3 Results

The ZnO NR array pattern was fabricated on the silicone hydrogel using it as a substrate by a lift-off process shown in **Figure 5-1A**. SEM was used to study the patterned ZnO NR array deposited on the synthetic silicone hydrogel as shown in **Figure 5-6A and B**. The designed pattern is made for easy identification of the captured fluorescence images to calibrate the pixel intensity depending on the concentration of glucose.

The patterned ZnO NR arrays grown on the synthetic silicone hydrogel were modified with amino groups (-NH<sub>2</sub>) to immobilize CdSe/ZnS QDs onto the ZnO NRs. Glutaraldehyde first reacted with -NH<sub>2</sub> functionalized ZnO NRs following the linkage formed by the reaction of glutaraldehyde with the amino group modified QDs. In **Figure 5-6C**, the hexagonal rods with a smooth surface were grown on the silicone hydrogel. The average dimensions of the ZnO NRs are estimated at  $120 \pm 5$  nm in diameter and  $2.00 \pm 0.05$   $\mu$ m in length. The rough surface of the NRs can be observed when decorated with QDs, as shown in **Figure 5-6D**. Furthermore, the TEM micrograph (**Figure 5-6E**) clearly shows the QDs are decorated on the ZnO NRs. The HRTEM micrograph (**Figure 5-6F**) further indicates the core-shell CdSe/ZnS QDs with  $5 \pm 2$  nm in diameter are decorated on the highly crystalline ZnO NRs with a lattice fringe of 0.255 nm. **Figure 5-7** shows the FTIR spectra of the ZnO NRs with surface modification, amino modified QDs, and the hybrid ZnO NRs coated with QDs (ZnO NR-QDs). All samples demonstrate the typical -CH stretch, and -CH<sub>2</sub> stretch in the FTIR spectra. The -C=O stretch at 1750 cm<sup>-1</sup> is observed when glutaraldehyde was modified onto ZnO NRs, while this stretch does not show up to sample of ZnO NR-QDs. The -C=N stretch of the imine group, and -C=N-R located around 1620 cm<sup>-1</sup> appears in the spectrum of ZnO NRs-QDs. Thus, two carbon-nitrogen double bonds (C=N), i.e. Schiff bases, were formed to allow QDs to coat on the ZnO NRs through the linkage of glutaraldehyde.



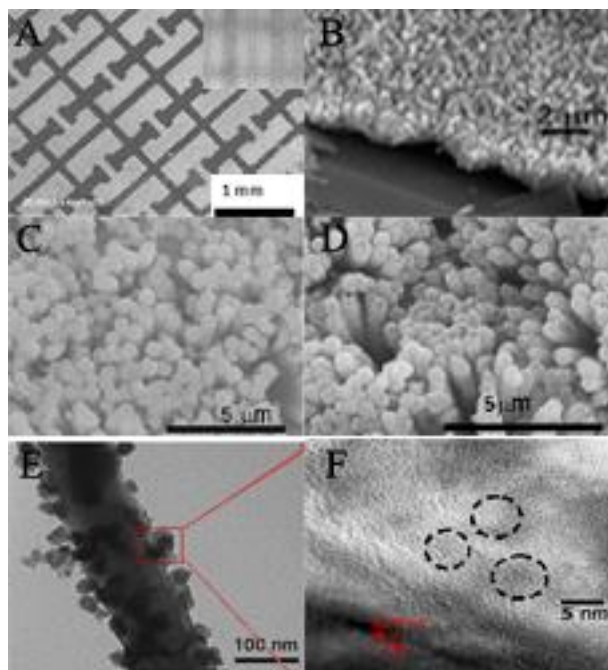


**Figure 5-6.** Characterization of nanomaterials by electron microscopy. A) SEM micrographs of patterned ZnO NRs deposited on a silicone hydrogel. The small inset is the photomask. B) The magnified SEM micrograph of ZnO nanorod array deposited on a silicone hydrogel. C) SEM micrograph of ZnO nanorods. D) SEM micrograph of QDs coated ZnO nanorods. E) TEM micrograph of QDs coated ZnO nanorods. F) HRTEM of CdSe/ZnS QDs.

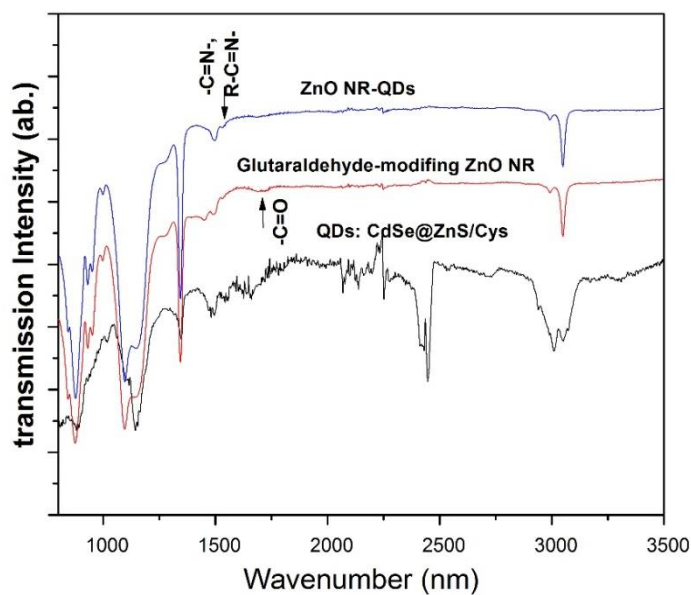


**Figure 5-7.** FTIR spectra of the cysteamine (Cys) modified QDs and ZnO nanorod (NR), and the hybrid ZnO NR coated with QDs (ZnO NR-QDs).

The optimization of the weight ratio of the donor (QDs) to enzyme (Con A) bonded with the acceptor (MG-dextran) was determined at 7:1. The photoluminescence (PL) properties of the nanostructured FRET transducer-coating ZnO NR array (i.e. the patterned FRET sensor), the nanostructured donor of the sensor (i.e. CdSe/ZnS QDs) were studied by a fluorospectrometer in the range of 550–700 nm. In **Figure 5-8A**, the photoluminescence (PL) spectrum of ZnO in the visible range is observed with centering at 628 nm.

10  $\mu\text{L}$  of aqueous glucose of various concentrations were dropped onto the patterned FRET sensors on silicone hydrogels with 30 seconds of interaction time. The fluorescence measurements were determined by fluorospectrometry. As shown in the illustration of **Figure 5-1a**, the fluorescence emission of the donor (CdSe/ZnS QDs) of the designed FRET sensor was quenched by the acceptor MG. The FRET emission ( $\lambda_{\text{em}}=652$  nm) as a function of the concentration of aqueous glucose were measured. The relative fluorescence intensity ( $I_{\text{re}}$ ) is calculated by using the equation below;

### Equation 5-3

$$I_{\text{re}} = I'/I_0$$

where  $I'$  is the restored intensity according to a glucose level,  $I_0$  the intensity of the sensor without glucose, or 0 glucose concentration. **Figure 5-8B** shows two linear regions; (1) from 0.03 to 3 mmol/L; and (2) from 0 to 0.03 mmol/L.

The fluorescence images of the patterned FRET sensors on silicone hydrogel interacting 10  $\mu\text{L}$  of various concentrations of aqueous glucose were monitored by a handheld fluorescence microscope. **Figure 5-9A** shows two fluorescence images of the patterned FRET sensor interacting with two samples of aqueous glucose; 0.04 mmol/L (sample A) and 0.4 mmol/L (sample B). The recorded images by the handheld microscope were converted to the readable signal through Matlab. The pixel intensity was calibrated using MatLab to plot the intensity as a function of aqueous glucose concentration. The calibrated pixel intensities of the patterned FRET sensor is clearly increasing as glucose increases from 0.03 mmol/L to 0.6 mmol/L as shown in **Figure 5-9B**.

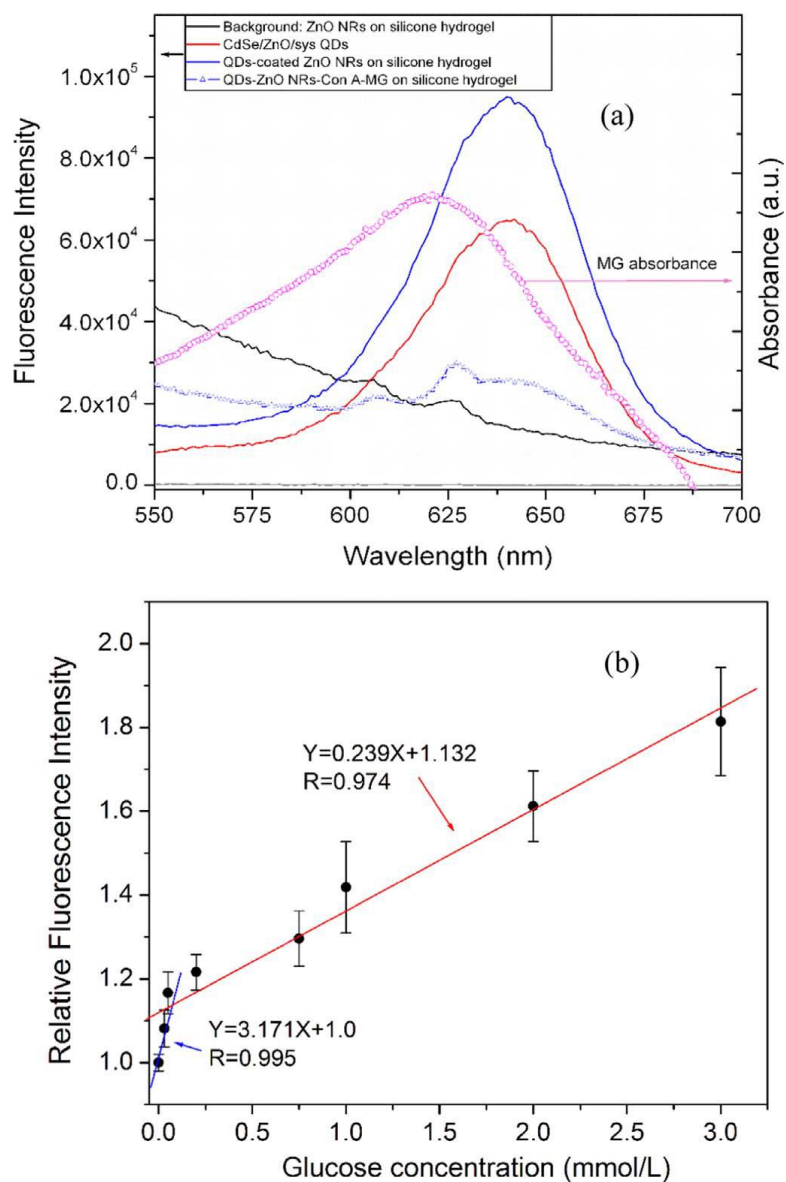


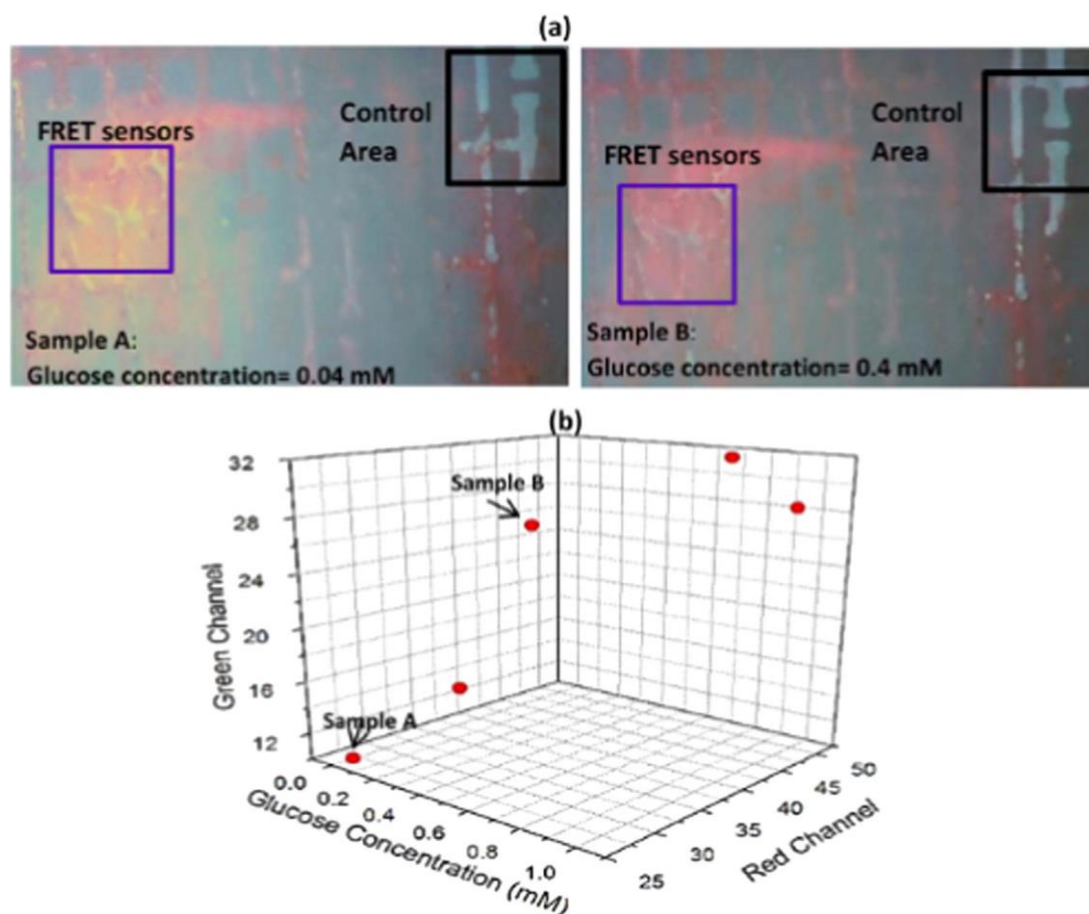
**Figure 5-8.** Photoluminescence of the glucose sensor. (a) Photoluminescence of ZnO NR arrays on silicone hydrogel with/without QDs, and QDs-based fret sensors, and the UV-vis absorption of MG. (b). A linear relationship between fluorescence intensity of the designed sensor and the concentration of glucose.

The rats' tear samples were diluted 3.5 times. The patterned FRET sensor deposited on silicone hydrogels were used to measure the 2  $\mu$ L diluted rats' tear samples. The PL spectra of the sensor corresponding to glucose in tears are shown in **Figure 5-10** after

interacting with rat tears. The detected glucose level in rats' tear samples were calculated by using **Equation 5-4**. Meanwhile, the blood glucose levels to the four rats were measured by Freestyle Lite Blood Glucose Monitoring System, Abbott Diabetes Care Inc. **Table 1** shows the glucose level in rats' tear samples measured by the nanostructured FRET sensor as compared to the blood glucose level of the four rats. The linear relationship between relative fluorescence intensity and glucose concentration in the range of 0.03–3 mmol/L can be expressed as follows;

#### Equation 5-4

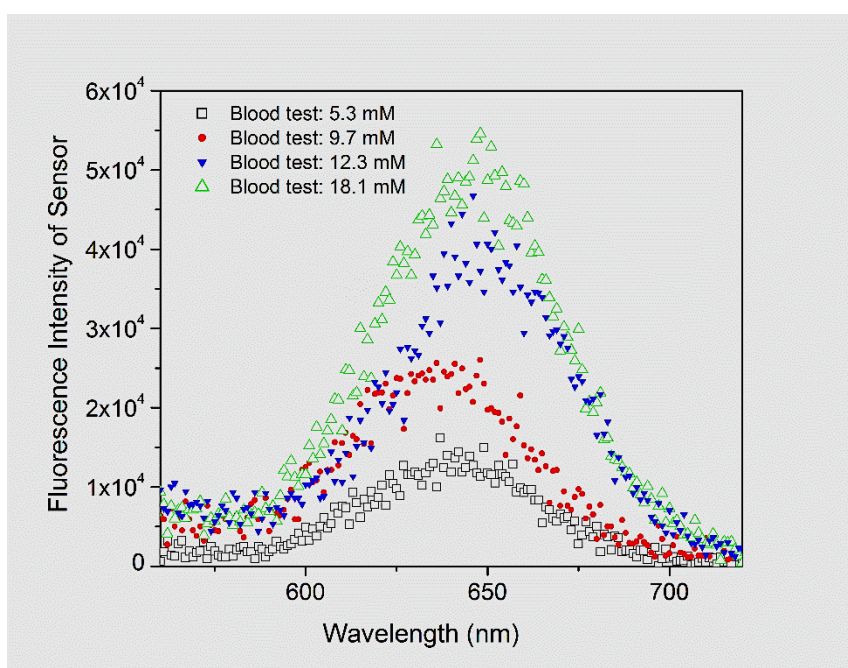
$$Y = 0.239X + 1.132$$



**Figure 5-9.** Fluorescence images of the patterned FRET sensor on silicone hydrogel and the relative pixel intensities of the sensors responding to the concentrations of glucose. (a) Fluorescence images of the patterned FRET sensor to aqueous glucose with 0.04 mmol/L and 0.4 mmol/L, respectively. (b) The relative pixel intensities of the sensors vs. the concentration of aqueous glucose.

**Table 5-1.** Glucose levels of in rat blood glucose vs tear glucose.

Blood Glucose (mmol/L)	Tear Glucose (mmol/L)
5.3	$0.14 \pm 0.03$
9.7	$0.42 \pm 0.04$
12.3	$0.95 \pm 0.05$
18.2	$1.28 \pm 0.05$

**Figure 5-10.** Photoluminescence spectra of designed sensor responding to tear samples from rats with different glucose level in blood.

The selectivity of the designed sensor towards glucose detection was further verified (**Figure 5-11**). 1 mM glucose in PBS solution and some possible interfering molecules, sucrose, fructose, mannose, lactose, maltose, mannitol, histidine, cysteine, ascorbic acid, and cholesterol at 1mM, were tested by the designed sensor, respectively. The relative sensing signal is referring to the normalization of the fluorescence intensity of the

designed sensor responding to 1mM test sample to the sensor's fluorescence intensity in the presence of 1mM glucose ( $I_{\text{test sample}}/I_{\text{glucose}}$ ).

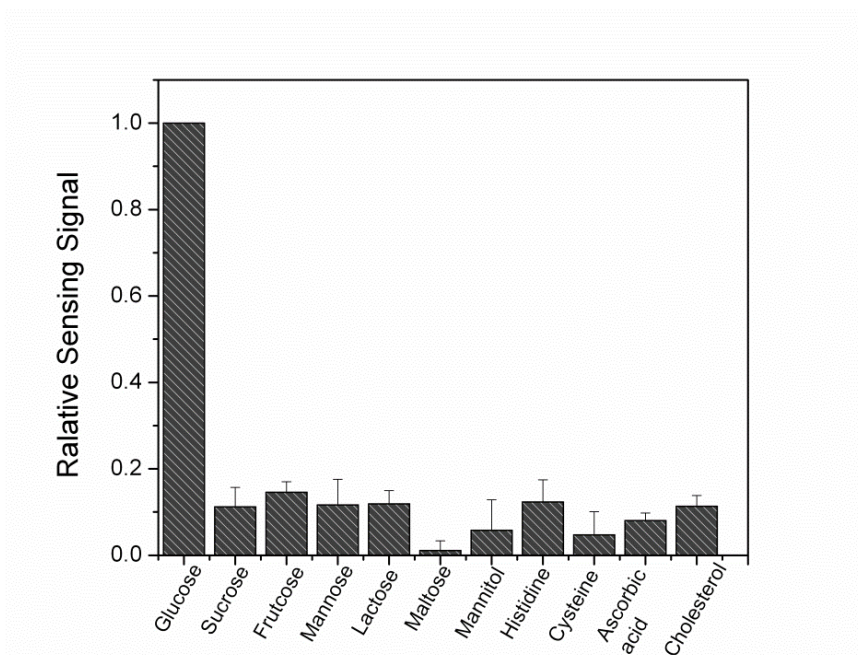


**Figure 5-11.** Relative Sensing Signal ( $I_{\text{test sample}}/I_{\text{glucose}}$ ) to different biomolecules.

## 5.4 Discussion

The maximum intensity of PL spectrum of CdSe/ZnS QDs is observed at 648 nm. The PL spectrum of ZnO NR-QDs is dominated by the decorated QDs because of the large amount of QDs on a single ZnO NR, centered at 648 nm. When the acceptor of FRET sensor, MG-dextran, bound to QDs through Con A, the PL peak of ZnO NRs can be observed with centering at 652 nm; whereas the PL peak at 652 nm attributed to the donor (QDs) of the patterned FRET sensor is significantly suppressed. The slight redshift of the emission of QDs may be caused by the surface conjugation of Con A and the acceptor of MG-dextran. MG quenches the fluorescence signal of QDs through the FRET mechanism because of its broad absorbance around 650 nm. The HRTEM micrograph (**Figure 5-6F**) further indicates the core-shell CdSe/ZnS QDs with  $5 \pm 2$  nm in diameter

are decorated on the highly crystalline ZnO NRs with a lattice fringe of 0.255 nm, which corresponds to the (0002) lattice planes demonstrated by Chen et al.<sup>32</sup>

In the presence of glucose, the quenched fluorescence of QDs is restored after the addition of glucose and the fluorescence emission of the patterned FRET sensors centered at 652 nm increases with increasing aqueous glucose. It is noted that the concentration of glucose in the range of 0.03–3 mmol/L can cover the tear glucose level of both the diabetes and healthy subject. The observed two linear regions can be attributed to the sensor's inherent sensitivity to glucose. As Con A contains 4 binding sites for glucose, the initial sharp response observed corresponds to the displacement of MG-dextran as a result of the glucose introduction. The secondary linear zone corresponds to the saturation of the Con A sites as glucose concentration increases.

The difference in pixel intensity value does not change significantly when the concentration of glucose is beyond 0.6 mmol/L. It is expected that a more advanced fluorescence microscope will be able to overcome the limit.

The concentrations of blood glucose of the rats used in the current study were maintained in a range similar to patients with 'poorly' managed Type 1 diabetes.<sup>33</sup> Specifically, rats were representative of low to moderate hyperglycemic patients with Type 1 diabetes mellitus under conventional insulin therapy.<sup>34</sup> Typically blood glucose concentrations in patient populations with type 1 diabetes fluctuate considerably; therefore, four rats with a range of blood glucose concentrations were utilized in the experiment to demonstrate. As shown in **Table 1**, the small value of the calculated standard deviation of the measurement indicates the repeatability of the measure with our glucose sensor.

In **Figure 5-11** indicates that other saccharide molecules and some small biomolecules existing in tears do not interfere with the measure of glucose. Thus, our design allows Con A specifically to interact with saccharides with smaller molecular weight, i.e. glucose.

## 5.5 References

1. Ohashi, Y., Dogru, M. & Tsubota, K. Laboratory findings in tear fluid analysis. *Clin. Chim. Acta* **369**, 17–28 (2006).
2. An, H. J. *et al.* Glycomics Analyses of Tear Fluid for the Diagnostic Detection of Ocular Rosacea. *J. Proteome Res.* **4**, 1981–1987 (2005).
3. Ridley, F. The Intraocular Pressure and Drainage of the Aqueous Humour. *Br. J. Exp. Pathol.* **11**, 217–240 (1930).
4. Michail, D., Vancea, P. & Zolog, N. Sur l'élimination lacrymale du glucose chez les diabetiques. *C R Soc Biol* **125**, 1095–1099 (1937).
5. Sen, D. K. & Sarin, G. S. Tear glucose levels in normal people and in diabetic patients. *Br. J. Ophthalmol.* **64**, 693–695 (1980).
6. Lewis, J. G. & Stephens, P. J. TEAR GLUCOSE IN DIABETICS. *Br. J. Ophthalmol.* **42**, 754–758 (1958).
7. Gasset, A. R., Braverman, L. E., Fleming, M. C., Arky, R. A. & Alter, B. R. Tear glucose detection of hyperglycemia. *Am. J. Ophthalmol.* **65**, 414–420 (1968).
8. Motoji, K. The glucose content of the tear fluid in normal and diabetic subjects. *Jpn. J. Clin. Ophthalmol.* **25**, 1945–1950 (1971).
9. Lane, J. D., Krumholz, D. M., Sack, R. A. & Morris, C. Tear glucose dynamics in diabetes mellitus. *Curr. Eye Res.* **31**, 895–901 (2006).
10. Boyne, M. S., Silver, D. M., Kaplan, J. & Saudek, C. D. Timing of changes in interstitial and venous blood glucose measured with a continuous subcutaneous glucose sensor. *Diabetes* **52**, 2790–2794 (2003).
11. Lodwig, V. & Heinemann, L. Continuous glucose monitoring with glucose sensors: calibration and assessment criteria. *Diabetes Technol. Ther.* **5**, 572–586 (2003).



12. Kvist, P. H. & Jensen, H. E. Recent advances in continuous glucose monitoring: biocompatibility of glucose sensors for implantation in subcutis. *J. Diabetes Sci. Technol.* **1**, 746–752 (2007).
13. O'Donnell, C., Efron, N. & Boulton, A. J. A prospective study of contact lens wear in diabetes mellitus. *Ophthalmic Physiol. Opt.* **21**, 127–138 (2001).
14. March, W., Long, B., Hofmann, W., Keys, D. & McKenney, C. Safety of contact lenses in patients with diabetes. *Diabetes Technol. Ther.* **6**, 49–52 (2004).
15. Tyagi, S., Marras, S. A. E. & Kramer, F. R. Wavelength-shifting molecular beacons. *Nat Biotech* **18**, 1191–1196 (2000).
16. Forster, T. 10th Spiers Memorial Lecture. Transfer mechanisms of electronic excitation. *Discuss. Faraday Soc.* **27**, 7–17 (1959).
17. Moschou, E. A., Sharma, B. V., Deo, S. K. & Daunert, S. Fluorescence Glucose Detection: Advances Toward the Ideal In Vivo Biosensor. *J. Fluoresc.* **14**, 535–547 (2004).
18. Ballerstadt, R., Evans, C., McNichols, R. & Gowda, A. Concanavalin A for in vivo glucose sensing: a biotoxicity review. *Biosens. Bioelectron.* **22**, 275–284 (2006).
19. Russell, R. J., Pishko, M. V., Gefrides, C. C., McShane, M. J. & Cote, G. L. A fluorescence-based glucose biosensor using concanavalin A and dextran encapsulated in a poly(ethylene glycol) hydrogel. *Anal. Chem.* **71**, 3126–3132 (1999).
20. Pickup, J. C., Hussain, F., Evans, N. D., Rolinski, O. J. & Birch, D. J. S. Fluorescence-based glucose sensors. *Biosens. Bioelectron.* **20**, 2555–2565 (2005).
21. Resch-Genger, U., Grabolle, M., Cavaliere-Jaricot, S., Nitschke, R. & Nann, T. Quantum dots versus organic dyes as fluorescent labels. *Nat. Methods* **5**, 763+ (2008).

22. Jamieson, T. *et al.* Biological applications of quantum dots. *Biomaterials* **28**, 4717–4732 (2007).
23. Zhang, J., Hodge, W., Hutnick, C. & Wang, X. Noninvasive diagnostic devices for diabetes through measuring tear glucose. *J. Diabetes Sci. Technol.* **5**, 166–172 (2011).
24. Zhang, J., Wang, X., Chen, L., Li, J. & Luzak, K. Harnessing a nanostructured fluorescence energy transfer sensor for quick detection of extremely small amounts of glucose. *J. Diabetes Sci. Technol.* **7**, 45–52 (2013).
25. Chen, L., Bao, Y., Denstedt, J. & Zhang, J. Nanostructured bioluminescent sensor for rapidly detecting thrombin. *Biosens. Bioelectron.* **77**, 83–89 (2016).
26. Chen, Y., Tse, W. H., Chen, L. & Zhang, J. Ag nanoparticles-decorated ZnO nanorod array on a mechanical flexible substrate with enhanced optical and antimicrobial properties. *Nanoscale Res. Lett.* **10**, 106 (2015).
27. Lee, C.-M. *et al.* Surface engineering of quantum dots for in vivo imaging. *Nanotechnology* **21**, 285102 (2010).
28. Kim, J., Conway, A. & Chauhan, A. Extended delivery of ophthalmic drugs by silicone hydrogel contact lenses. *Biomaterials* **29**, 2259–2269 (2008).
29. Kim, J. Y. & Osterloh, F. E. ZnO-CdSe nanoparticle clusters as directional photoemitters with tunable wavelength. *J. Am. Chem. Soc.* **127**, 10152–10153 (2005).
30. Costenaro, D., Carniato, F., Gatti, G., Bisio, C. & Marchese, L. On the Physico-Chemical Properties of ZnO Nanosheets Modified with Luminescent CdTe Nanocrystals. *J. Phys. Chem. C* **115**, 25257–25265 (2011).
31. McCartney, L. J., Pickup, J. C., Rolinski, O. J. & Birch, D. J. Near-infrared fluorescence lifetime assay for serum glucose based on allophycocyanin-labeled concanavalin A. *Anal. Biochem.* **292**, 216–221 (2001).

32. Chen, C. *et al.* Enhanced Raman scattering and photocatalytic activity of Ag/ZnO heterojunction nanocrystals. *Dalton Trans.* **40**, 9566–9570 (2011).
33. Nathan, D. M. The diabetes control and complications trial/epidemiology of diabetes interventions and complications study at 30 years: overview. *Diabetes Care* **37**, 9–16 (2014).
34. Melling, C. W. J. *et al.* A model of poorly controlled type 1 Diabetes Mellitus and its treatment with aerobic exercise training. *Diabetes Metab.* **39**, 226–235 (2013).

## CHAPTER 6

*The final chapter of this thesis revisits the motivation, research objectives, and provides a summary of the important findings and conclusions of Chapters 2-5. Limitations and future studies for theranostics motivated by this work presented in this thesis will be discussed.*

### 6 CONCLUSION AND FUTURE DIRECTIONS

#### 6.1 Overview of Rationale and Research Questions

Theranostics is a constantly evolving field, providing new opportunities in developing new healthcare technologies at an affordable price.<sup>1</sup> The application of nanoparticles is highly suitable for theranostics as it provides material-based properties, a framework for personalized medicine, and high-surface area to volume fitting for surface modifications.<sup>2-4</sup> The goal of theranostics is to concurrently provide biomedically relevant diagnostic information and exert a pharmaceutical effect and overcome potential limitations of current technology. Applications of theranostic applications aim to enhance drug carriers, biosensors, and imaging entities.

For instance, gadolinium contrast agents have been proven to cause adverse effects if in its free ionic form rather than chelated.<sup>5,6</sup> Through transmetallation, the Gd ions can be replaced in the chelator by Fe, Ca, Zn, and Cu ions, where thereby the Gd may freely interfere with cation channels leading to splenic degeneration, liver necrosis, etc.<sup>5</sup> Cases of neurotoxicity have also been reported.<sup>7</sup>

Drug delivery can be affected by natural barriers such as the hepatic first pass, the blood brain barrier, and diffusion through fenestrations causing a loss of therapeutic concentration and therefore shortening the duration of treatment or not achieving the therapeutic threshold to exert a therapeutic response.<sup>8,9</sup>

The application of nanoparticles for theranostics is dependent its functionalization with targeting ligands, proteins, and antibodies for specificity and functionality.<sup>10</sup> It is already understood nanoparticle possess far superior properties that can address the shortcomings

of current biomedical technologies. However, as a whole, nanoparticles and its functionalization is not yet understood with regards to functionalization strategies and cellular interactions.

In response to these unknowns of theranostic applications, the overarching objective of this thesis was to assess and understand nanoparticle-protein interactions at the molecular and cellular level to provide pertinent developments in pushing the area of nanotechnology forward for biomedical applications. The specific research questions investigated here include: 1) Is our theranostic model composed of an organic nanoparticle drug carrier core hybridized with inorganic fluorescent nanoparticles and functionalized with anti-human antibodies suitable for drug delivery? (Chapter 2); 2) What are the repercussions of functionalization strategies on cell viability? (Chapter 3); 3) Can Gd-based UCNPs functionalized with anti-VEGF exert the same anti-angiogenic therapeutic effect as anti-VEGF while simultaneously provide upconversion fluorescence and MRI tracking potential? (Chapter 4); 4) Can non-invasive nanoparticle-protein biosensors provide high selectivity and sensitivity for the quantification of glucose? (Chapter 5).

## **6.2 Summary and Conclusions**

In Chapter 2, we quantitatively assessed gelatin-based nanospheres hybridized with CdSe/ZnS/cysteamine QDs and functionalized with anti-human IgG Fab for non-specific targeted drug delivery. Assessed in UTA-6 osteosarcoma cells, the functionalized nanoparticles of  $480 \pm 50$  nm exhibited an increase of 50% cellular interaction compared to non-functionalized particles ( $p = 0.0023$ ). The relative viability at a concentration  $40 \mu\text{g/mL}$  remained above 80% with no significant difference ( $p = 0.8074$ ) between the different samples. The results indicate our model is an effective model for maximizing the abilities of drug-loaded gelatin nanoparticles for targeted drug delivery and imaging.

In Chapter 3, we contrasted and compared the repercussions of modification strategies of our gelatin-based nanoparticle (GNP) model. With the same modifications as mentioned on Chapter 2, we assessed the order of modification first with either QDs or anti-IgG and followed by the other. PEGylation was also performed and assessed to potentially

increase compatibility. The results indicated modification strategy did not significantly impact the size but rather the addition of anti-IgG that significantly increased the size compared to the bare GNP ( $p < 0.0001$ ). The amount of QDs hybridized ( $p = 0.1000$ ) and anti-IgG bioconjugated ( $p = 0.727$ ) did not differ significantly. Through live cell imaging, the modified GNPs were able to be fluorescently detected and located with UTA-6 cells through a z-stack. Cell viability of UTA-6 osteosarcoma cells differed significantly ( $p < 0.05$ ) between Path A (ie: QD first followed by anti-IgG) and Path B (ie: anti-IgG first followed by QD). Path A modified GNP remained above 80% viability even when treated with 40  $\mu\text{g}$  whereas Path B modified GNP decreased to below 50% viability. PEGylation significantly decreased Path A viability slightly ( $p = 0.0034$ ) while remaining above 70% at 40  $\mu\text{g}$ , whereas Path B viability increased slightly ( $p = 0.0019$ ) as a result but did not reach above 60%. The results implicate the components and modification strategies must be considered when developing nanoparticle technology for therapeutic applications as the final product may possess significant repercussions which may inhibit its full potential.

In Chapter 4, we quantitatively assessed an upconversion nanoparticle model functionalized with anti-VEGF for the treatment of pathological angiogenesis with bimodal tracking via upconversion fluorescence and magnetic resonance. We verified upconversion fluorescence via a spectrophotometer outfitted with a NIR laser and MRI compatibility with VSM and a 3 T MRI. Relative viability was assessed in HUVECs with various concentrations of Gd-UCNPs, Gd-antiVEGF UCNPs, and the anti-VEGF equivalent. Gd-UCNP has a significantly higher viability compared to the Gd-antiVEGF UCNPs ( $p = 0.0114$ ) when treated with up to 300  $\mu\text{g/mL}$  of nanoparticles. Viability at 10 and 100  $\mu\text{g/mL}$  of UCNPs or anti-VEGF indicated Gd-UCNPs yielded a higher viability in comparison to both its anti-VEGF functionalized counterpart and the anti-VEGF equivalent ( $p < 0.05$ ). We were able to quantify the observed morphological changes with confocal microscopy as a result of the treatments. Anti-VEGF based treatments produced a significantly shorter cell length ( $p < 0.0001$ ) than Gd UCNPs. The results suggest there were no significant difference between anti-VEGF and the Gd-antiVEGF except for the

bimodal imaging properties. This suggests the Gd-antiVEGF model is suitable for theranostic applications as an alternative to bare anti-VEGF.

In Chapter 5, we assessed a non-invasive method of glucose detection in tears as a reflection of blood glucose using a FRET quenching mechanism. Con A covalently bonded with QDs with glutaraldehyde was loaded with MG-dextran. The MG-dextran acts to quench the QDs signal until glucose is introduced. As a result, the MG-dextran was displaced from Con A as glucose had demonstrated a higher affinity to increase the detected fluorescent signal. The biosensor was anchored to a ZnO nanorod substrate for stability. The FRET sensor demonstrated both selectivity and sensitivity to detect glucose between 0.03 mM and 3 mM. The tear glucose of diabetics is noted to be  $> 0.35 \pm 0.04$  mM. Our results verified our sensor was able to measure tear glucose in a volume as little as 2  $\mu$ L in a short span of time.

In summary, we demonstrated the importance of proteins and antibodies to provide functionality to nanoparticles and provided nanoparticle solutions to address shortcomings of current biomedical technology. We demonstrated 2 potential methods of drug delivery a) drug carrier modified with fluorescent nanoparticles and antibodies for selectivity; b) therapeutic antibodies directly conjugated onto the surface of MR compatible and upconversion trackable nanoparticles. We also provided an alternative to invasive glucometry via a non-invasive tear glucose biosensor with high selectivity and sensitivity for changes in glucose measured by fluorescence.

## **6.3 Limitations**

In this section, we address some limitations of the technologies presented in Chapters 2-5. A description of both study specific limitations and technological limitations will be discussed.

### **6.3.1 Study Specific Limitations**

*Engineering Large Gelatin Nanospheres Coated with Quantum Dots for Targeted Delivery to Human Osteosarcoma Cells with Enhanced Cellular Internalization (Chapter*

*2) and Cellular interaction influenced by surface modification strategies of gelatin-based nanoparticles (Chapter 3)*

In the studies presented in Chapters 2 and 3, the inverted microscope outfitted for live imaging used to obtain cell images did not possess the ideal imaging conditions for accurate identification of the QD modified GNs and GNPs. As evidenced in the images, the fluorescent signal obtained was observed to be oval in nature. This observed phenomena, an airy disk, is resultant of the microscope collecting out of focus light above and below the objective focal plane.<sup>11</sup> A significant amount of out of focus fluorescence emission was delivered through the aperture to produce the airy disk. As a result, the localization of the fluorescent nanoparticles was not accurate as assumptions had to be made to assess the internalization and surface interactions. We evaluated the particle based on the centre of the emission relative the surface of the cell, the plane of which the cell surface was in focus.

*Bimodal imaging compatible theranostic nanoparticles for anti-angiogenic treatment (Chapter 4)*

In the study presented in Chapter 4, the observed HUVECs did not form a uniform monolayer as expected when angiogenesis was induced with PMA. The observed cells tended to aggregate into distinct groups and overlap leading to inaccurate measures of cell morphology at times. Furthermore, the cells did demonstrate sprout tip formation and elongation as reported by Osaki et al.<sup>12</sup> but extensive connected vascular networks as demonstrated by Nagamori was not observed after 24 hours.<sup>13</sup> This could be been resultant of an underestimation of seeding density causing isolated pockets of cells. As a result, we were unable to quantify the density of the network or growth of the network. However, the results were conclusive of the anti-angiogenic properties of the Gd-antiVEGF UCNPs to mitigate angiogenesis by assessing the elongation of the cells as proof of the migration and sprout tip formation during angiogenesis. The decreased viability was proof of the anti-proliferative response to the anti-VEGF treatments.

*Nanostructured biosensor for detecting glucose in tear by applying fluorescence resonance energy transfer quenching mechanism (Chapter 5)*



In the study presented in Chapter 5, the murine model compatibility with the sensor area was a challenge. Firstly, the biosensor modified on to the ZnO nanorod substrate was applied in its dehydrated form. The substrate was unable to conform to the shape of the murine eye during direct application. Secondly, the biosensor distribution localized was caused during the conjugation process to the ZnO as the biosensor was applied as a droplet onto the substrate. The distribution of the sensor droplet was dependent on the surface tension. As a result, adjustments were required to ensure the full content of the biosensor was exposed to the tear glucose. This application may have caused slight discomfort to the mouse while under sedation.

### 6.3.2 General Limitations

Pertinent to Chapters 2, 3, and 5, we acknowledge the QDs have not been perfected and therefore additional investigations are required to validate them as candidates for *in vivo* biomedical applications. QDs, possess the fluorescent qualities suitable for biomedical applications as they are resistant to photobleaching, highly stable as a whole, and possess tunable fluorescence.<sup>14,15</sup> However, on a deeper level, QDs even when capped for enhanced stability are subject to the dissociation of the heavy metal ion constituents from the core in response to acidic pH and aerobic conditions.<sup>16</sup> The leaching of Cd ions can occur through the ZnS shell to cause cytotoxicity at concentrations as low as 1 nM *in vitro*.<sup>17</sup> The incorporation of the protein metallothionein into the model may sequester low levels of Cd ions into an inert complex.<sup>18</sup> Another core concern is the application of high energy photons to stimulate the fluorescent response. Side effects include genotoxicity and mutagenesis resulting in carcinogenesis.<sup>19-21</sup> As demonstrated with gel electrophoresis, shorter excitation wavelengths, and longer irradiation periods are known to induce significant damage as well.<sup>22</sup>

In Chapter 4 we inclined to shift to UCNPs as the multi-photon NIR infrared excitation possesses the ideal spectral and optical window for biological imaging.<sup>23,24</sup> One limitation UCNPs for bimodal compatible imaging in MRI and fluorescence is the optimization of lanthanide dopants essential to its function. The efficiency of its desired effects come as a tradeoff between size and the amount of lanthanides doped. A larger diameter UCNPs

theoretically can hold a larger concentration of lanthanide dopants. However, is the size tradeoff worth it if there are biological repercussions when introduced *in vitro* or *in vivo*. Furthermore, the concentration of individual lanthanide dopants can be adjusted to suit the individual needs of the imaging modality under consideration. It is possible with further investigation to refine and optimize the dopants concentrations for bimodal applications with the desired properties suitable for biomedical applications.

As discussed in Chapters 2-4, antibody and therapeutic protein bioconjugation to nanoparticles are effective for cell targeting and treatment. However, they possess limitations of their own. Steric hindrance and spatial orientation of the protein of choice is important for execution of its function. In our direct conjugation method, steric hindrance may have limited the amount of antibodies and proteins conjugated on the surface, yet at the same time limit access of the nanoparticle surface laden functional groups to cellular processes which may negatively impact cellular processes as reported by Kim et al.<sup>25</sup> Steric hindrance of protein conjugation can be addressed with the addition of linker molecules which extend from the surface of the nanoparticles themselves.<sup>26</sup> These same molecules may also be used to spatially orientate antibodies to maximize their potential and function.<sup>27</sup>

## **6.4 Future Directions**

### **6.4.1 Upconversion nanoparticle based contact lens biosensor for non-invasive glucose detection**

Our results in Chapters 4 and 5 prompted us revisit the biosensor laden substrate using a contact lens compatible material and UCNPs for signal generation. The results strongly support the advantages of using the Er, Yb lanthanide pair for the biosensor signal. Using a similar construct of Con A loaded with MG-dextran, we conjugated the UCNPs with glutaraldehyde to form a stable covalent bond prior to loading directly onto the surface of the silicone hydrogel. Our foundation in nanoparticle-protein manipulation and functionalized aided in the optimization of conditions for suitable for glucose sensing with UCNPs.

Our preliminary results as shown in **Figure 6-1** demonstrates the potential for the UCNPs-based sensor for glucose detection. We were able to confirm not only the deposition of the sensor onto the silicone hydrogel via scanning electron microscopy, but the Con A and the UCNPs as well (**Figure 6-1A**). We were able to generate an optimization curve for the Gd-UCNPs to Con A ratio as well (**Figure 6-1B**).

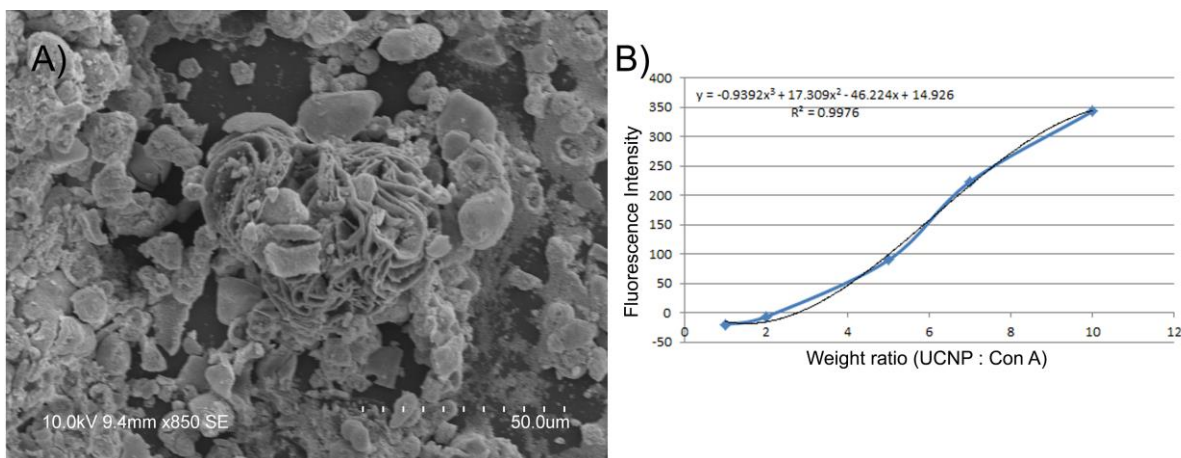


**Figure 6-1.** UCNP-based glucose sensor. A) Scanning electron micrograph of the biosensor loaded onto the surface of the silicone hydrogel. The Con A and UCNPs can be clearly seen in the image. B) Optimization curve of the UCNP to Con A weight ratio.  $R^2 = 0.9976$ .

We aim to evaluate the performance in a proof-of-concept study to:

- a) Employ NIR lasers to measure changes in glucose within the therapeutic optical window (700 nm – 1700 nm)<sup>23</sup>
- b) Develop a wearable version of the biosensor for direct glucose sensing

The next steps in the study involve refining silicone model as whole to minimize the potential dissociation of the biosensor from the surface and design the biosensor orientation on the silicone hydrogel curb impeding of vision. As well, glucometric data will be obtained *in vitro* and *in vivo* with a murine model.

### **6.4.2 Biomedical collaborations for treatment design**

The next steps in developing biomedically relevant nanoparticle technology is to seek collaborations with clinicians and other research groups dedicated to disease treatment research. The merriment of interdisciplinary knowledge provides an understanding of the disease treatment regimen of various pathologies and the limitations that nanoparticles can address. As we have discussed previously, nanoparticles are capable of being effective drug carriers that can overcome physiological barriers and can localize therapeutics to an area of interest. By understanding the conditions for an effective treatment of current pathologies, nanoparticles are adequate entities to be tailored and personalized for specific diseases or patient needs.

## **6.5 Significance and Impact**

Although the physical and material-based properties of nanoparticles have been extensively studied, there is a lack of understanding the consequences at the cellular level when they are personalized for specific applications or pathological treatments. Using various combinations of nanoparticles (organic or inorganic) functionalized with proteins and antibodies to provide purpose, various theranostic applications were assessed; drug delivery with two different models and high sensitivity non-invasive glucose sensing. This thesis significantly advances our understanding of the nanoparticle and protein interactions as the future of biotechnology to combine diagnostics and therapeutics into one practical entity that can be tailored to individual needs. The studies presented in this thesis provides unequivocal evidence that nanotechnology can circumvent the challenges of modern technology through increased stability of metal ions, potentiate a higher or induce a similar therapeutic response, and provide a safer alternative for biosensing and drug delivery.

Additionally, this thesis increased the fundamental knowledge of theranostic model design and functionalization strategies to optimize and maximize the potential of nanoparticles for various applications.

## 6.6 References

1. Vogenberg, F. R., Isaacson Barash, C. & Pursel, M. Personalized medicine: part 1: evolution and development into theranostics. *Pharm. Ther.* **35**, 560–576 (2010).
2. Pye, H. *et al.* A HER2 selective theranostic agent for surgical resection guidance and photodynamic therapy. *Photochem. Photobiol. Sci.* **5**, 341–354 (2016).
3. Weinshilboum, R. Inheritance and drug response. *N. Engl. J. Med.* **348**, 529–537 (2003).
4. Voura, E. B., Jaiswal, J. K., Mattoussi, H. & Simon, S. M. Tracking metastatic tumor cell extravasation with quantum dot nanocrystals and fluorescence emission-scanning microscopy. *Nat. Med.* **10**, 993–998 (2004).
5. Tedeschi, E. *et al.* Gadolinium retention in the body: what we know and what we can do. *Radiol. Med.* **122**, 1–12 (2017).
6. Andreucci, M., Solomon, R. & Tasanarong, A. Side Effects of Radiographic Contrast Media : Pathogenesis , Risk Factors , and Prevention. *Biomed Res. Int.* **2014**, 1–21 (2014).
7. Maramattom, B. V, Manno, E. M., Wijdicks, E. F. & Lindell, E. P. Gadolinium encephalopathy in a patient with renal failure. *Neurology* **64**, 1276–1278 (2005).
8. Naik, A., Kalia, Y. N. & Guy, R. H. Transdermal drug delivery: Overcoming the skin's barrier function. *Pharm. Sci. Technol. Today* **3**, 318–326 (2000).
9. Nicoll, L. H. & Hesby, A. Intramuscular injection: An integrative research review and guideline for evidence-based practice. *Appl. Nurs. Res.* **15**, 149–162 (2002).
10. Gravitz, L. Therapy: this time it's personal. *Nature* **509**, S52–S54 (2014).
11. Pawley, J. B. *Handbook of Biological Confocal Microscopy*. (Springer, 2006).
12. Osaki, T. *et al.* Acceleration of vascular sprouting from fabricated perfusable

- vascular-like structures. *PLoS One* **10**, 1–14 (2015).
13. Nagamori, E. *et al.* Biomaterials Network formation through active migration of human vascular endothelial cells in a multilayered skeletal myoblast sheet. *Biomaterials* **34**, 662–668 (2013).
  14. Chan, W. C. W. *et al.* Luminescent quantum dots for multiplexed biological detection and imaging. *Curr. Opin. Biotechnol.* **13**, 40–46 (2002).
  15. Gao, X. *et al.* In vivo molecular and cellular imaging with quantum dots. *Curr. Opin. Biotechnol.* **16**, 63–72 (2005).
  16. Zeng, C., Ramos-Ruiz, A., Field, J. A. & Sierra-Alvarez, R. Cadmium telluride (CdTe) and cadmium selenide (CdSe) leaching behavior and surface chemistry in response to pH and O<sub>2</sub>. *J. Environ. Manage.* **154**, 78–85 (2015).
  17. Brunetti, V. *et al.* InP/ZnS as a safer alternative to CdSe/ZnS core/shell quantum dots: in vitro and in vivo toxicity assessment. *Nanoscale* **5**, 307–317 (2013).
  18. Derfus, A. M., Chan, W. C. W. & Bhatia, S. N. Probing the Cytotoxicity of Semiconductor Quantum Dots. *Nanoletters* **4**, 11–18 (2004).
  19. Ananthaswamy, H. N. & Pierceall, W. E. Molecular Mechanisms of Ultraviolet Radiation Carcinogenesis. *Photochem. Photobiol.* **52**, 1119–1136 (1990).
  20. Shibutani, S., Takeshita, M. & Grollman, A. P. Insertion of Specific Bases during DNA Synthesis Past the Oxidation-Damaged Base 8-OxodG. *Nature* **349**, 431–434 (1991).
  21. Wood, M. L., Dizdaroglu, M., Gajewski, E. & Essigmann, J. M. Mechanistic Studies of Ionizing Radiation and Oxidative Mutagenesis: Genetic Effects of a Single 8-Hydroxyguanine ( 7-Hydro-8-oxoguanine ) Residue Inserted at a Unique Site in a Viral Genome<sup>1</sup>. *Biochemistry* **29**, 7024–7032 (1990).
  22. Ge, J. *et al.* Standard Fluorescent Imaging of Live Cells is Highly Genotoxic.

- Cytometry A* **83**, 552–560 (2014).
23. Hong, G., Antaris, A. L. & Dai, H. Near-infrared fluorophores for biomedical imaging. *Nat. Biomed. Eng.* **1**, 1–22 (2017).
  24. Liu, B., Li, C., Yang, P., Hou, Z. & Lin, J. 808-nm-Light-Excited Lanthanide-Doped Nanoparticles : Rational Design , Luminescence Control and Theranostic Applications. *Adv. Mater.* **29**, (2017).
  25. Kim, J. A. *et al.* Low Dose of Amino-Modified Nanoparticles Induces Cell Cycle Arrest. *ACS Nano* **7**, 7483–7494 (2013).
  26. Yu, M. K., Park, J. & Jon, S. Targeting strategies for multifunctional nanoparticles in cancer imaging and therapy. *Theranostics* **2**, 3–44 (2012).
  27. Arruebo, M., Valladares, M. & González-Fernández, Á. Antibody-conjugated nanoparticles for biomedical applications. *J. Nanomater.* 1–24 (2009).

## APPENDIX

### APPENDIX A: Permission for Republication of Scientific Article

Rightslink® by Copyright Clearance Center

<https://s100.copyright.com/AppDispatchServlet#formTop>

# RightsLink®

[Home](#) [Create Account](#) [Help](#)


**Title:** Engineering large gelatin nanospheres coated with quantum dots for targeted delivery of human osteosarcoma with enhanced cellular internalization

**Conference Proceedings:** Nanotechnology (IEEE-NANO), 2014 IEEE 14th International Conference on

**Author:** Wai Hei Tse

**Publisher:** IEEE

**Date:** Aug. 2014

Copyright © 2014, IEEE

**LOGIN**

If you're a [copyright.com](#) user, you can login to RightsLink using your [copyright.com](#) credentials. Already a RightsLink user or want to [learn more?](#)

#### Thesis / Dissertation Reuse

**The IEEE does not require individuals working on a thesis to obtain a formal reuse license, however, you may print out this statement to be used as a permission grant:**

*Requirements to be followed when using any portion (e.g., figure, graph, table, or textual material) of an IEEE copyrighted paper in a thesis:*

- 1) In the case of textual material (e.g., using short quotes or referring to the work within these papers) users must give full credit to the original source (author, paper, publication) followed by the IEEE copyright line ♠ 2011 IEEE.
- 2) In the case of illustrations or tabular material, we require that the copyright line ♠ [Year of original publication] IEEE appear prominently with each reprinted figure and/or table.
- 3) If a substantial portion of the original paper is to be used, and if you are not the senior author, also obtain the senior author's approval.

*Requirements to be followed when using an entire IEEE copyrighted paper in a thesis:*

- 1) The following IEEE copyright/ credit notice should be placed prominently in the references: ♠ [year of original publication] IEEE. Reprinted, with permission, from [author names, paper title, IEEE publication title, and month/year of publication]
- 2) Only the accepted version of an IEEE copyrighted paper can be used when posting the paper or your thesis on-line.
- 3) In placing the thesis on the author's university website, please display the following message in a prominent place on the website: In reference to IEEE copyrighted material which is used with permission in this thesis, the IEEE does not endorse any of [university/educational entity's name goes here]'s products or services. Internal or personal use of this material is permitted. If interested in reprinting/republishing IEEE copyrighted material for advertising or promotional purposes or for creating new collective works for resale or redistribution, please go to [http://www.ieee.org/publications\\_standards/publications/rights/rights\\_link.html](http://www.ieee.org/publications_standards/publications/rights/rights_link.html) to learn how to obtain a License from RightsLink.

If applicable, University Microfilms and/or ProQuest Library, or the Archives of Canada may supply single copies of the dissertation.

[BACK](#)
[CLOSE WINDOW](#)

Copyright © 2017 [Copyright Clearance Center, Inc.](#) All Rights Reserved. [Privacy statement.](#) [Terms and Conditions.](#)  
Comments? We would like to hear from you. E-mail us at [customer@copyright.com](mailto:customer@copyright.com)





RightsLink®

[Home](#)
[Create Account](#)
[Help](#)




**Title:** Cellular interaction influenced by surface modification strategies of gelatin-based nanoparticles

**Author:** Wai Hei Tse, Laszlo Gyenis, David W Litchfield, et al

**Publication:** Journal of Biomaterials Applications

**Publisher:** SAGE Publications

**Date:** 02/01/2017

Copyright © 2017, © SAGE Publications

**LOGIN**

If you're a [copyright.com](#) user, you can login to RightsLink using your [copyright.com](#) credentials. Already a RightsLink user or want to [learn more?](#)

If you are a SAGE journal author requesting permission to reuse material from your journal article, please note you may be able to reuse your content without requiring permission from SAGE. Please review SAGE's author re-use and archiving policies at <https://us.sagepub.com/en-us/nam/journal-author-archiving-policies-and-re-use> for more information.

If your request does not fall within SAGE's reuse guidelines, please proceed with submitting your request by selecting one of the other reuse categories that describes your use. Please note, a fee may be charged for reuse of content requiring permission. Please contact [permissions@sagepub.co.uk](mailto:permissions@sagepub.co.uk) if you have questions.

[BACK](#)
[CLOSE WINDOW](#)

Copyright © 2017 [Copyright Clearance Center, Inc.](#) All Rights Reserved. [Privacy statement.](#) [Terms and Conditions.](#) Comments? We would like to hear from you. E-mail us at [customercare@copyright.com](mailto:customercare@copyright.com)

**ELSEVIER LICENSE  
TERMS AND CONDITIONS**

Jun 30, 2017

This Agreement between Western University -- Wai Hei Tse ("You") and Elsevier ("Elsevier") consists of your license details and the terms and conditions provided by Elsevier and Copyright Clearance Center.

License Number	4137090411451
License date	Jun 27, 2017
Licensed Content Publisher	Elsevier
Licensed Content Publication	Biosensors and Bioelectronics
Licensed Content Title	Nanostructured biosensor for detecting glucose in tear by applying fluorescence resonance energy transfer quenching mechanism
Licensed Content Author	Longyi Chen,Wai Hei Tse,Yi Chen,Matthew W. McDonald,James Melling,Jin Zhang
Licensed Content Date	May 15, 2017
Licensed Content Volume	91
Licensed Content Issue	n/a
Licensed Content Pages	7
Start Page	393
End Page	399
Type of Use	reuse in a thesis/dissertation
Portion	full article
Format	both print and electronic
Are you the author of this Elsevier article?	Yes
Will you be translating?	No
Order reference number	
Title of your thesis/dissertation	Study of protein-nanoparticle interaction for theranostic applications
Expected completion date	Aug 2017
Estimated size (number of pages)	150
Elsevier VAT number	GB 494 6272 12
Requestor Location	Western University 1151 Richmond Street  London, ON N6A 3K7 Canada Attn: Western University
Total	0.00 CAD

## Curriculum Vitae

### EDUCATION

- September 2007-  
April 2012      Bachelor of Medical Science  
Honours Specialization Medical Biophysics  
(Medical Science Concentration)  
The University of Western Ontario, London, Ontario, Canada
- September 2012-  
August 2017      Doctor of Philosophy  
Department of Medical Biophysics  
The University of Western Ontario, London, Ontario, Canada  
*Supervisor:* Dr. Jin Zhang  
*Thesis:* “The Design, Fabrication, and Characterization of Protein Nanoparticle Interactions for Theranostic Applications.”

### RESEARCH POSITIONS

- May 2008-  
April 2012      **Undergraduate Research Assistant**  
Ontario Ginseng Innovation and Research Consortium  
London, Ontario, Canada  
*Supervisor:* Dr. Ed Lui
- September 2011-  
April 2012      **Fourth Year Undergraduate Honours Thesis Student**  
Lawson Health Research Institute, Victoria Hospital  
London, Ontario  
*Supervisor:* Dr. Karel Tysl  
*Project:* “The effect of ascorbate on the bacterial load in septic mice.”
- August 2012      **Research Assistant**  
Multifunctional Nanocomposites Lab, the University of Western Ontario  
London, Ontario  
*Supervisor:* Dr. Jin Zhang  
*Project:* “Development of nanocomposites for multi-functional delivery systems.”
- September 2012-  
August 2017      **Graduate Research Assistant, Doctoral**  
Department of Medical Biophysics, The University of Western Ontario,  
London, Ontario, Canada  
*Supervisor:* Dr. Jin Zhang  
*Thesis:* “The Design, Fabrication, and Characterization of Protein Nanoparticle Interactions for Theranostic Applications.”

### RESEARCH-SPECIFIC HONOURS, SCHOLARSHIPS, AND AWARDS

- 2011-2015            Western Graduate Research Scholarship  
*Awarded to a full time graduate student for stipend support who has maintained an average of 80% or more.*  
 Institutional  
 \$4,500 CAD / year
- 2015-2017            National Sciences and Engineering Research Council fo Canada (NSERC), Postgraduate Scholarships- Doctoral (PGS-D)  
*Awarded to high-caliber scholars engaged in a Doctoral Program among top-ranked applicants.*  
 National  
 \$42,000 CAD
- 2016                    School of Graduate Graduate and Postdoctoral Studies, Doctoral Excellence Research Award  
*Awarded to outstanding doctoral scholars holding a Tri-Agency Scholarship (NSERC, CIHR, SSHRC)*  
 Institutional  
 \$10,000 CAD
- 2017                    33<sup>rd</sup> Canadian Biomaterials Society Annual Meeting Best Presentation Award, Canadian Biomaterials Society  
*Awarded to the top oral presenters who presented first author original research papers.*  
 National  
 \$200 CAD

## **PUBLICATIONS and PRESENTATIONS**

### **A. Refereed Journal Manuscripts (11 Published, 3 in preparation)**

#### **Published (11)**

1. Zhang J, Bi R, Hodge W, Yin P, and **Tse WH**. Nanocomposite contact lens for the delivery of hydrophilic protein drugs. *Journal of Materials Chemistry B*. 1; 4388-4395, 2013.
2. **Tse WH**, Gyenis L, Litchfield DW, and Zhang J. Engineering hybrid gelatin nanospheres coated with quantum dots for targeted delivery of human osteosarcoma with enhanced cellular internalization. *Proceedings of the 14th IEEE International Conference on Nanotechnology*. 672-677, 2014.
3. Chen Y, Guo X, **Tse WH**, Sham TK, and Zhang J. Magnetic Anisotropy Induced in NiCo Granular Nanostructures by ZnO Nanorods Deposited on A Polymer Substrate. *RSC Advances*. 4(89); 47987, 2014.
4. Zhang J, Chen L, **Tse WH**, Bi R, Chen L. Inorganic nanoparticles: engineering for biomedical applications. *Nanotechnology Magazine, IEEE*. 8; 21-28, 2014.

5. Chen C, **Tse WH**, Chen L, and Zhang J. Ag nanoparticles-decorated ZnO nanorod array on a mechanical flexible substrate with enhanced optical and antimicrobial properties. *Nanoscale Research Letters*. 10(106), 2015. DOI 10.1186/s11671-014-0712-3
6. Yin P, Huang G, **Tse WH**, Bao Y, Denstedt J, and Zhang J. Nanocomposited silicone hydrogels with a laser-assisted surface modification for inhibiting the growth of bacterial biofilm. *Journal of Materials Chemistry B*. 3; 3234-3241, 2015.
7. Huang G, **Tse WH**, and Zhang J. Deposition of Hydrophilic Nanocomposite-based Coating on Silicone Hydrogel through a Laser Process to Minimize UV Exposure and Bacterial Contamination. *RSC Advances*. 6; 67166-67172, 2016.
8. **Tse WH**, Gyenis L, Litchfield DW, and Zhang J. Cellular interaction influenced by surface modification strategies of gelatin-based nanoparticles. *Journal of Biomaterials Applications*. 31; 1087-1096, 2017.
9. Chen L, **Tse WH**, Chen Y, McDonald MW, Melling J, and Zhang J. Nanostructured biosensor for detecting glucose in tear by applying fluorescence resonance energy transfer quenching mechanism. *Biosensors and Bioelectronics*. 19; 393-399, 2017. doi: 10.1016/j.bios.2016.12.04 – **co-first author**
10. Leszek J, **Tse WH**, Zhang J, Ávila-Rodríguez MF, Tarasov VV, Barreto GE, Bachurin SO, and Aliev G. Nanotechnology for Alzheimer Disease. *Current Alzheimer Research*. 2017. doi: 10.2174/1567205014666170203125008.
11. Chen L, **Tse WH**, Siemiarczuk A, Zhang J. Special properties of luminescent magnetic NaGdF<sub>4</sub>: Yb<sup>3+</sup>, Er<sup>3+</sup> upconversion nanocubes with surface modifications. *RSC Advances*. 7; 26770-26775, 2017.

### **In Preparation (3)**

1. **Tse WH**, Chen L, McDonald MW, Melling J, and Zhang J. Development of Upconversion Nanostructure Contact Lens Biosensors for Non-invasive Tear Glucose Measurement. *Small*. (In preparation; 2017) – **co-first author**
2. **Tse WH**, Yang S, and Zhang J. Bimodal imaging compatible theranostic nanoparticles for anti-angiogenic treatment. (In preparation; 2017)
3. **Tse WH**, L Chen, McCurdy CM, Tarapacki CM, Chronik BA, and Zhang J. Biocompatible imaging with NaGdF<sub>4</sub>: Er<sup>3+</sup>, Yb<sup>3+</sup> Upconversion Nanoparticles on HUVEC Cells. (In preparation; August 2017).

### **B. Published Refereed Conference Papers (1)**

1. **Tse WH**, Gyenis L, Litchfield DW, and Zhang J. Engineering hybrid gelatin nanospheres coated with quantum dots for targeted delivery of human osteosarcoma with enhanced cellular internalization. *Proceedings of the 14th IEEE International Conference on Nanotechnology*. 672-677, 2014. (Conference Proceed Publication)

### **C. Peer Reviewed Published Conference Abstracts (3)**

1. Yin P, Huang G, **Tse WH**, and Zhang J. Laser-assisted modification of silicone nanocomposites to inhibit protein absorption. *CAMBR*. 0038. Centre for Advanced Materials and Biomaterials Research 2012.
2. **Tse WH**, Gyenis L, Litchfield DW, and Zhang J. Engineering hybrid gelatin nanospheres coated with quantum dots for enhanced cell internalization. *CAMBR*. 0066. Centre for Advanced Materials and Biomaterials Research 2013.
3. **Tse WH**, Gyenis L, Litchfield DW, and Zhang J. Engineering hybrid gelatin nanospheres coated with quantum dots for targeted delivery of human osteosarcoma with enhanced cellular internalization.  
Institute of Electrical and Electronics Engineers International Conference on Nanotechnology (IEEE-Nano) 2014: 672, 0057.

### **D. Peer Reviewed Oral Presentations (2) \*presenter**

1. Zhang J\*, **Tse WH**, and Hodge WG. Conjugation of antibody on biocompatible nanoparticles for targeted drug delivery. ARVO 2013 Annual Meeting, Seattle, Washington, USA. (May 2013)
2. **Tse WH**, and Zhang J. Development of a biocompatible upconversion nanoparticle model for theranostic applications in anti-angiogenesis. 33<sup>rd</sup> Annual Meeting of the Canadian Biomaterials Society, Winnipeg, Manitoba. (May 2017)

### **PROFESSIONAL MEMBERSHIPS**

- |           |   |
|-----------|---|
| 2012-2013 | The Association for Research in Vision and Ophthalmology<br><i>Student Member</i> |
| 2017      | Canadian Biomaterials Society<br><i>Student Member</i>                            |